UNIVERSITY
OF SOUTHERN
QUEENSLAND
AUSTRALIA

MODELLING THE COMPRESSIVE STRENGTH AND THERMAL
PROPERTIES OF FOAM CONCRETE

A Thesis submitted by

Qiang Li Candidate, M Eng

For the award of

Doctor of Philosophy

2017

ABSTRACT

Foam concrete has attracted attention worldwide because of its light weight and enhanced insulating properties as a building material. Pore features in foam concrete play an important role in affecting its compressive strength and insulation properties. Therefore, quantitative description of relationships between pore features heat conductivity and compressive strength is the main aims of this thesis. To accomplish the aims, theoretical method is employed to deduce the heat conductivity, and experimental method is used to justify its compressive. Further, Matlab and Python program are programmed to depict the random pore distribution, and then finite element method is employed to calculate its compressive based on the pore distribution.

Initially, experimental testing of the compressive strength of foam concrete is carried out, in which Ø2.68 mm and Ø7 mm of EPS beads are adopted in order to study the influences of volume fraction and size. The results of this work showed that the compressive strength of EPS concrete at 28 days can be expressed as: $f_{2.68} = 5.58 \times 10^{-8} \times \rho^{2.72}$ and $f_7 = 3.2 \times 10^{-9} \times \rho^{3.07}$, in which ρ is the density of EPS concrete. By comparing the experimental results and the calculated results from simulation, it can be established that the smaller EPS beads size and the lower the EPS volume fraction, the smaller the difference between calculated and experimental data. Furthermore, Young's modulus for specimens containing different EPS beads is measured with strain gauges during the compression process. Based on the stochastic of pore features of foam concrete, numerical method is employed to construct a pore feature function related to volume fraction. Then the relationship between pore features and compressive strength is correlated.

Next, a theoretical model for idealized foam concrete with a uniform pores distribution is devised to describe compressive strength at 28 days $f_c = f_0(1 - \frac{fix\left(\frac{3V_f a^3}{4\pi r^3}\right)^{\frac{2}{3}} \pi r^2}{a^2})$, in which f_0 is compressive strength of completely solid concrete, f_c is compressive strength under a certain volume fraction of pore, a is cubic sample size, r is the radius of pore size, V_f is the volume fraction, and fix is a

round function. Additionally, compressive strength by mixing two sizes of pores is studied and the results indicated that the compressive strength is reduced when compared to that made by just one-size pores. Also the maximum compressive strength is achieved when the volume fraction ratio for the two sized pores is 50:50.

A 2-D random pore distribution program is used to describe the pore (by EPS) distribution in real concrete. The pores distribution generated by the program in 2 dimensions is compared with that from experimental images, and it is established that the random model can be used to describe the pores distribution in 2 dimensions. Following this, a 3-dimensional distribution program is written, and the 3-dimensional model is imported into Abaqus software expressly to calculate stress distribution. The simulation results confirms that stress concentration is generated locally where the inter pores distances are minimal during loading pressure. Stress distribution in the sample with the smaller pores is more uniformly distributed than that for large pores.

Finally, in this thesis, a heat conductivity model for foam concrete is built according to heat transference principles. A mixed heat transferring model by series and parallel mode is utilised: $k_e = k_s \dfrac{k_g \sqrt[3]{V_g{}^2} + k_s\left(1 - \sqrt[3]{V_g{}^2}\right)}{k_g\left(\sqrt[3]{V_g{}^2} - V_g\right) + k_s\left(1 - \sqrt[3]{V_g{}^2} + V_g\right)}$, in which k_e is the effective heat conductivity, k_s is the heat conductivity of the solid concrete part, k_g is the heat conductivity of air in the hollow pores, and V_g is the pore volume fraction. Compared with series, parallel, Maxwell-Eucken and the Carson heat transferring model, the heat conductivity calculated by the proposed model more closely matches the experimental results, and the relative error is less than 6%. Using this heat conductivity model, the temperature field of a building wall made of foam concrete is compared with that made of traditional concrete under simulating fire incident conditions. This temperature field simulation indicates that the foam concrete wall allows people longer period to escape from the fire.

The highlight of this thesis is following:1) building a relationship between pore feature and compressive strength; 2) building a compressive strength model of two sizes EPS beads mixing model; 3) compiles a program code for random pore

distribution model and predicting the stress distribution; 3) building a heat conductivity model of foam concrete that fits experimental results well;

Key words: Foam concrete; Heat conductivity; Compressive strength; EPS beads; Numerical simulation

Certification of Thesis

This thesis is entirely the work of ___*Qiang Li*_____ except where otherwise acknowledged. The work is original and has not previously been submitted for any other award, except where acknowledged.

Student and supervisors signatures of endorsement are held at USQ.

_____

Principal Supervisor

Professor Hao Wang

_____

Associate Supervisor

Frank Bullen

_____

Associate Supervisor

Zuhua Zhang

PUBLICATIONS

Chun-li Mo, **Qiang Li**, Xu-ming Guo, Hao Wang, Numerical Simulation the temperature field of the multi-coil batch during annealing process in Bell-type furnace, Advance Material Research, Vols. 538-541, 2012: pp 637-641.

Qiang Li, Hao Wang, Frank Bullen and Andrew Reid, Numerical Simulation of Porous Structure in Foam Concrete on Thermal Insulation Property, ACCM8 Kuala Lumpur, Malaysia, 6 - 8 November 2012.

Qiang Li, Hao Wang, Zuhua Zhang, Andrew Reid. Numerical simulation of porosity on thermal properties and fire resistance of foamed concrete, Journal of Sustainable Cement-Based Materials, Vols.2,2013: 13-19,

Yu, Bao Yi and Wang, Qing and **Li, Qiang** and Wu, Yu Juan and Chen, Yan (2013) Interface microstructure and mechanical properties of copper/aluminum composite material. In: 3rd International Conference on Advanced Engineering Materials and Technology (AEMT 2013), 11-12 May 2013, Zhangjiajie, China.

Zhang, Zuhua and Wang, Hao and Provis, John L. and Reid, Andrew and **Li, Qiang** (2013) Durability of fly ash based-geopolymers: effect of crystallization on mechanical properties. In: 8th International Symposium on Cement and Concrete (ISCC 2013), 20-23 Sep 2013, Nanjing, China.

Qiang Li, Fuan Hua, Jianping Li, Hao Wang, Research difference of strain distribution and microstructure evolution between rolling direction and transverse direction of AM50 Mg Alloy plate by Digital Image Correlation, Advances in Materials Science and Engineering,Vol.2015, Article ID 175873, page7.

Qiang Li, Qiaoyi Guo, Hao Wang, The effect of r/a on its compressive strength of EPS concrete, Computer and Concrete, under reviewing;

Qiang Li, Baoyi Yu, Yingdong Qu, Hao Wang, Kaiyu Zhao, Numerical simulation of random distribution of EPS beads distribution in 2D and 3D, submitted to Advances in Cement Research.

ACKNOWLEDGEMENTS

TABLE OF CONTENTS

LIST OF FIGURES

CHAPTER 4 THEORETICAL METHOD TO DEDUCE THE COMPRESSIVE STRENGTH OF EPS CONCRETE

CHAPTER 5 SIMULATION OF EPS BEADS DISTRIBUTION IN EPS CONCRETE

CHAPTER 6 SIMULATION OF THE STRESS DISTRIBUTION WITHIN FOAM CONCRETE

CHAPTER 7 THERMAL PROPERTIES OF FOAM CONCRETE

LIST OF TABLES

CHAPTER 6 SIMULATION OF THE STRESS DISTRIBUTION WITHIN FOAM
CONCRETE

CHAPTER 7 THERMAL PROPERTIES OF FOAM CONCRETE

CHAPTER 1 INTRODUCTION

Foam concrete is a lightweight concrete that air-voids are entrapped or entrained in the solid concrete body [1], which has been used in the non-structural and structural construction since 1920s[2, 3]. In the last century, foam concrete developed quickly, especially for the present, energy saving spreads all over the world[2, 4]. Foam concrete with advantages of light weight, good insulation, sound absorption, fire resistance and low manufacturing cost is widely used in construction industries[4]. Using foam concrete to partly replace the traditional concrete as non-bearing walls or ceilings can not only reduce the buildings weight leading to reduced dead-loads on the foundation and make the buildings more energy-efficient, but also can reduce CO_2 emission during the construction and the whole service life of building, therefore, it is regarded as an environmentally friendly material [2, 5, 6].

Now most of foam concrete applications are related to its thermal insulation properties and mechanical properties[7, 8]. Generally, thermal insulation properties increase with decreasing the density of foam concrete, while the mechanical properties are in the same trend as the density variation. In fact, the low compressive strength of foam concrete limits its applications in thermal insulation field. Therefore, the application of foam concrete has to consider the balance between the thermal insulation properties and mechanical properties. The macroscopic thermal insulation properties and mechanical properties are directly influenced by the microscopic pore features, such as porosity, pore size, pore area fraction, pore distribution, pore shape factor, etc [8, 9].

Currently study on foam concrete focuses on the influence of the porosity on the compressive strength and heat conductivity [10-12], which neglects pore features' influence, including pore size, pore shape factor, pore area fraction and pore size distribution, etc. Although the porosity of foam concrete is regarded as an primary role in determining the compressive strength and heat conductivity[13-15], knowing the pore features is helpfu3.l to understand how these microscale pore features affect the macro physical properties, which can also provide a theoretical tool to design, evaluate and optimize the foam concrete producing process[16].

However, pore features of foam concrete are statistical data obtained from experimental specimens, which vary in different samples[15, 16], especially for the pore size, pore shape factor, pore area fraction, pore distribution et al. Besides the porosity of foam concrete, pore size is regarded as another important factors afftecting the compressive strength of foam concrete[2, 9], in which the smaller size of pores leads to higher compress strength. Moreover, the compressive strength model of foam concrete related with porosity and pore size is empirical model. Therefore it is necessary to study the pore features of foam concrete by quantitative method.

Although, using EPS beads to replace foam is an effective way to study the influence of pore size on compressive strength, the ratio of EPS beads size to sample size and different size EPS beads mixing together are ignored before, and these research works have real significantly meaning for industrial production. Further, heat conductivity is an important index to evaluate energy saving efficiency of building, and a good model of heat conductivity can predict the heat conductivity of foam concrete more accurately that can reduce the experimental cost effectively. Finally, the comparison of temperature field between traditional concrete and foam concrete during fire accidence is studied to illustrate its well thermal insulation property.

This thesis aims to determine the relationships between compressive strength/heat conductivity and pore features of foam concrete, which is helpful for engineers and researcher to design and manufacture foam concrete with a certain property. To accomplish this aim, experimental, theoretical and numerical simulation methods have been employed to investigate the influence of pore size on compressive strength, the reconstruction of the pores distribution in 2D and 3D, the stress distribution during loading process and heat conductivity as well as temperature field of foam concrete during fire accidence are studied.

The thesis is divided into 8 chapters: Chapter 1 is a brief introduction of the thesis; Chapter 2 is the literature review; Chapter 3 is the compressive strength and Young's modulus of EPS concrete at different volume fractions and sizes by experimental method; Chapter 4 presents theoretical model of compressive strength;

Chapter 5 is the EPS distribution that is carried by computer simulation and compared with real sample; Chapter 6 is a simulation of EPS concrete compressive strength under different volume fractions and sizes; Chapter 7 explores a heat conductivity model for foam concrete and the resultant temperature field during fire incident; Chapter 8 forms the summary.

CHAPTER 2 LITERATURE REVIEW

2.1 Research background

Concrete remains one of the most widely used manmade construction materials in the world. Traditional concrete is composed of Portland cement, sand, aggregates and water [17], and its density ranges from 2240 to 2600 kg/m^3 [18] with a compressive strength in a range of 20 – 80 MPa [19]. Global cement consumption was about 41 billion tons in 2015 [20]. Generally, unreinforced concrete is used in a compressive condition whereas reinforced concrete can be subjected to tensile loading. The latter is used extensively in applications such as buildings, bridges, tunnels, reservoirs, marine structure and other infrastructural projects.

Although concrete plays an important role in modern construction and buildings, its whole life negative impacts cannot be neglected. The cement production process releases great amount of CO_2. Production of 1 kg cement generates 0.9 kg CO_2 [21]. Overall concrete production contributes 8% of global CO_2 emission [22], and is one of the biggest sources of global warming gas. The concrete industry also consumes 40% of world energy, 12% of world water consumption and generates 40% of waste to landfill [23]. Therefore, there is an urgent demand to improve concrete industries to be more environmentally friendly and sustainable.

Since the 1970s energy crisis, energy saving has become a common goal internationally. It then becomes important for the building/construction industry to develop improved materials to make buildings more energy efficient. Thermal insulation is one of the effective measures to achieve energy savings in buildings [24]. Foam concrete is a type of lightweight concrete with good thermal insulation properties that makes buildings more energy efficient than traditional fully solid Portland concrete. Due to its lower density, foam concrete is easier to transport from one location to another, and it is easier to cut than traditional concrete. Foam concrete also doesn't contain any easily combustible substances and can be used as an excellent fire barrier in the construction of buildings [25]. In addition, due to air pores embedded into concrete, it has excellent sound absorbing properties [1, 26]. As energy efficient material with a relatively low production cost, a minimum

strength is required as well as insulation and sound absorption, it has attracted interest from both researchers and construction industry.

2.1.1 What is foam concrete

Generally speaking, foam concrete is made of cement, water and air bubbles(foam), and the volume of foam in concrete determines the density of foam concrete, which can range from $300kg/m^3$ to $1800kg/m^3$ [11], much lower than traditional solid Portland concrete.

The first patent for foam concrete can be dated back to 1923 [1, 23]. Its construction applications as a lightweight non- and semi-structural material have increased significantly in the last decade. The first comprehensive review of foam concrete was presented by Valore in 1954 [1, 23, 27]. In 2000, Narayanan and Ramamurthy [11] reviewed the properties of foam concrete, including water absorption, capillarity properties, durability, thermal conductivity, fire resistance and acoustic properties. In 2007, Nambiar, Kunhanandan and Ramamurthy [15] focused their research on the characteristics of air voids in foam concrete. Barayanan and Ramamurthy [11] reviewed research developments on microstructure and properties of foam concrete, in which different models of volume fraction and strength are considered. To date, foam concrete has been widely accepted by industries and academics, and more and more different kinds of foam concrete have been developed, including higher compressive strength and environmental-friendly foam concrete [28, 29].

2.1.2 Classification of foam concrete

Foam concrete can be broadly classified into three classes according to the method of pore formation [11] as listed as below:

1) Gas concrete, where gas forming chemicals are mixed into lime or concrete mortar during the liquid or plastic stages and gas is generated by a chemical reaction;

2) Foam concrete in which the pre-formed foam is mixed with concrete and water. This method has the lowest production cost, but pore size and volume fraction in the concrete is difficult to control;

3) A combination of the above methods.

2.1.3 Advantages and limitations of foam concrete

Due to the presence of a large volume of void pores, foam concrete has some special characteristics:

  1) low self-weight means that it can save lots of cement, and can also be transported more easily [30];

2) low heat conductivity makes it more suitable as thermal insulation material and fire-resistant material [31, 32];

3) the large pore volume in the concrete results in lower production cost than traditional concrete [33];

4) foam concrete has good sound absorption properties that can reduce noise impact on residential and commercial buildings [29, 30, 34].

Despite the many advantages of foam concrete, low compressive strength is one of important factors limiting its wider application.

2.1.4 Application of foam concrete

With the advantages mentioned above, foam concrete has a wide spread of applications, such as roof decks, heat and sound insulation walls, and road sub-base etc [35, 36].

Figure 2. 1 Examples of Foam concrete applications a) insulation wall, b) running track sub-base [36]

Two applications of foam concrete are depicted in Figure 2.1. In the first, it is used as an insulation wall, which can make the building more energy efficient. In the second, it is used as a sub-base of a running track, an application where minimized strength is required. These diverse applications indicate that foam concrete has a large market potential as the energy efficiency and lower production costs become more important for its market acceptance. It is predicted that the use of foam concrete in industrial and civil buildings will be greatly expanded.

2.2 Previous research on foam concrete

Historically, researchers have paid much attention to chemical composition and physical properties [1, 37-40], mechanism of chemical reaction [41, 42], and relationships between pore volume fraction and mechanical/thermal insulation properties of foam concrete [43-47]. Other researchers investigated stress distribution, failure mechanism [48-50], creep and shrinkage, and cracking caused by shrinkage [51-54]. All the research can be summarized as either the relationship between chemical composition and properties or the relationship between micro-structure and properties.

When the chemical composition is known, the final properties of foam concrete are dependent its structure. Most of previous models are related to the pore volume fraction, which means that if the pore volume fraction is known, thermal properties and mechanical properties can be deduced. This is based on the assumption that all void spaces are uniform in size and distribution and of a spherical shape. These models didn't consider the influences of irregular pore shape and variable pore sizes on the final properties.
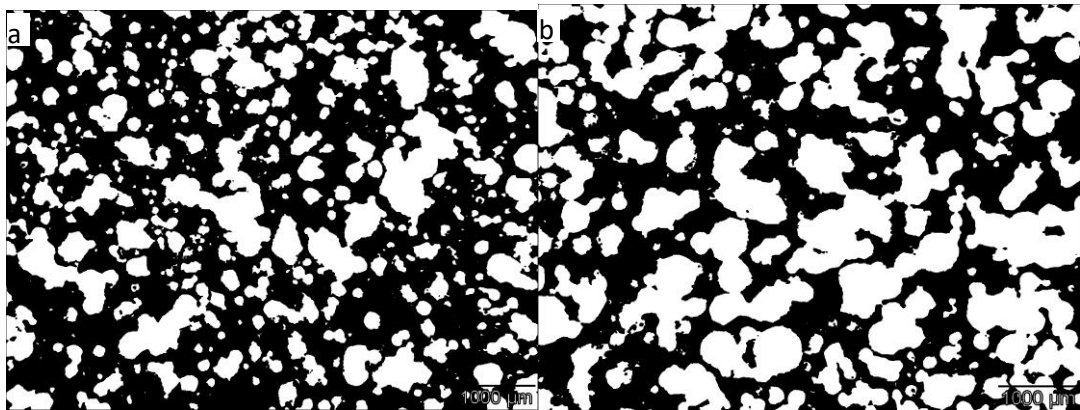
Figure 2. 2 Actual pore structure image of foam concrete[1]

A pore structural morphology of foam concrete is imaged in Figure 2.2, in which the white colour part represents for the porous regions and the black part represents for

---

[1] Images are provided by Dr Zuhua Zhang

the matrix binder regions. In Figure 2.2 a), volume fraction of 13% is depicted and in Figure 2.2 b) volume fraction of 20% is depicted. These images demonstrate that the pore size ranges from 0.1mm to several mm, and as the pore volume fraction increases, the average pore size also increases.

It is also indicated in Figure 2.2 that the pore size is variable and the pore shape is not uniformly spherical. It is apparent that the volume fraction only doesn't reflect the real pore structure of foam concrete, and that the roles of these irregular pores in affecting the properties need to be studied.

It becomes very useful to quantitatively and accurately describe the internal pores structure and to establish a relationship between the irregular pore structure and properties. The ability to design and control pore structure for high efficiency and low cost by using modelling approach instead of relying solely on the experimental method has significant advantage.

2.2.1 Mechanical properties

Compressive strength is one of the most important indexes for concrete materials. Foam concrete with high void space possesses much lower compressive strength than normal Portland concrete. The relationship between void ratio and compressive strength of foam concrete play a determined role in limiting the foam concrete application. A suitable model describing relationship between void ratio and compressive strength is thus highly desired during foam concrete mix design process. With the model, the balance between weights of foam concrete and compressive can be predicted. Over the past decades, researchers developed different models to describe the relationships between pore volume fraction and the compressive strength of foam concrete [10, 11, 13, 16, 55]. These models are listed in Table 2.1.

Table 2. 1 Compressive strength model of foam concrete [10, 11, 13, 16, 39, 56-59]

Model name	Mathematical model description
Feret's equation	$S = K \left[\frac{1}{1 + \left(\frac{w}{c}\right) + \left(\frac{a}{c}\right)} \right]^{n}$; where w/c is water-cement ratio, a/c

	is air-cement ratio, and K and n are constants.
Schiller Equation	$S = K_s \ln(P_{cr}/P)$ where P_{cr} is the critical volume fraction corresponding to zero strength, and K_s is the coefficient;
Powers' gel-space ratio	$S = Kg^n$; where g is the gel-space ratio, and K and n are constants;
Strength-volume fraction	$n = 1 - [d_c(1 + 0.2\rho_c)/(1 + k)\rho_c\gamma_w]^b$; where d_c is concrete density, ρ_c is the specific gravity of cement, γ_w is the unit weight of water, k is water-cement ratio, and b is an empirical constant;
Balshin expression	$S = S_0(1 - p)^n$, S_0 is the strength at zero volume fraction, p is pore volume fraction, n is coefficient;
Ryshkevitch	$S = S_0 e^{-k,p}$; where S_0 is zero volume fraction strength, k is constant, and p is pore volume fraction;
Hasselmann	$S = S_0 - k_h p$; where S_0 is zero volume fraction strength, k_h is constant, and p is pores volume fraction;
Hoff	$\frac{f_y}{f_0} = \left(\frac{d_c}{1+k}\right)^b \left(\frac{1+0.2p_c}{p_c\gamma_w}\right)^b$; where σ_y compressive strength, k water/cement ratio, p_c concrete density, γ_w weight of water;
Kearsley	$S = 39.6(\ln(t))^{1.174}(1 - p)^{3.6}$; where t is time and p is pore volume fraction;
Nambiar	$S = b_0 + \sum_{i=1}^k b_i x_i + \sum_{i=1}^k b_{ii} x_i^2 + \sum_{i<j} \sum b_{ij} x_i x_j$; where x_i are quantitative variables, and b_0 and b_i are regression coefficients;
Lian	$S = \sqrt{A(1 - p)^m e^{-np}}$; where A, m and n are constants, and p is the volume fraction;
Omkar Deo and Narayanan Neithalath	$f_c' = \alpha_0 + \alpha_1 \left[\frac{\ln(d_{MFS})}{\ln \overline{d_n}}\right] + \alpha_2 \left(\frac{\varphi_A}{S_p}\right)^{-1} + \alpha_3 ln\Gamma_{3d}$; where $\alpha_0, \alpha_1, \alpha_2$ and α_3 are coefficients, $\overline{d_n}$ is averaged pore diameter, d_{MFS} is averaged pore distance, S_p is shape factor, φ_A is averaged pore area fraction, and Γ_{3d} is 3d shape factor.

It can be deduced from Table 2.1 that compressive strength models can be divided into three types. The first is based on water-cement and air-cement ratios including Feret's model, strength-volume fraction model and Hoff model. The second type is

based on the gel-space ratio including Powers' gel-space ratio, and the third type on the volume fraction including Balshin's expression and Ryshkevitch and Hasselmann model. However, most volume fraction-related models regard the overall void space as the only factor affecting compressive strength. Compressive strength can be expressed as an exponent function of volume fraction, but these models neglect the influence of pore features. The model presented by Omkar Deo does relate pore features to compressive strength, but the pores in the model are confined to an average pore size ranging from 3-10mm, which is much bigger than that of foam concrete.

Young's modulus and the Poisson ratio are also important property indexes for foam concrete, some researchers have presented models, which consider volume fraction [60-62] and Young's modulus. These are listed in Table 2.2.

Table 2. 2 Models employing Young's modulus of foam concrete [61, 62]

Model name	Mathematical description
Gibson and Ashby	$\frac{E}{E_{ref}} = \alpha \left(\frac{\rho}{\rho_{ref}}\right)^n$; where α is a constant, its value relied on the microstructure; n is exponent constant, and E_{ref} and ρ_{ref} are solid reference materials;
Christensen model	$\frac{E}{E_s} = \frac{2(7-\nu_s)}{3(1-\nu_s)(9+5\nu_s)}\frac{\rho}{\rho_s}$; where ρ_s is density of solid part, and ν_s is the Poisson's ratio of solid part;
Hashin-Strikman	$\frac{E_u}{E_s} = \frac{p}{1+C_H(1-p)}$; where $C_H = \frac{(1+\nu_s)(13-15\nu_s)}{2(7-5\nu_s)}$;
Simone and Gibson	$\frac{E}{E_s} \approx 0.315\left(\frac{\rho}{\rho_s}\right) + 0.209\left(\frac{\rho}{\rho_s}\right)^2$;
semi-empirical formulae	$\frac{E}{E_s} \approx \phi^2 \left(\frac{\rho}{\rho_s}\right)^2 + (1-\phi)\frac{\rho}{\rho_s}$; where ϕ is the solid mass fraction;

In models incorporated Young's modulus is a function of density and Poisson ratio. The density ratio and the solid mass fraction are all expressed as a volume fraction function.

In general, Poisson's ratio is assumed as a constant for foam concrete except for Christensen model [62]: $\nu = \frac{1+5\nu_s}{9+5\nu_s}$, in which ν_s is Poisson ratio of the zero volume fraction.

2.2.2 Thermal insulation property

Thermal insulation is one of the main applications for foam concrete. The thermal insulation ability depends on three factors: the heat conductivity, the density and the specific heat. The density of foam concrete can be readily obtained from its volume and mass, but the heat conductivity and the specific heat properties require some special facilities for their determination, which involves high cost. Therefore, the ability to theoretically calculate heat conductivity and the specific heat for foam concrete is highly desirable.

(1) Heat conductivity model

Again, there are many different models to predict heat conductivity as listed in Table 2.3.

Table 2. 3 Heat conductivity models [63-68]

Model name	Mathematical description of heat conductivity
Series model	$k_e = \frac{1}{\frac{1-v_g}{k_s}+\frac{v_2}{k_g}} = \frac{k_s \times k_g}{(1-v_g)k_g+v_2 k_s}$; where k_s and k_g are heat the conductivities of solid and gas, respectively, and v_g is the air void pore volume fraction.
Parallel model	$k_e = (1-v_g)k_s + v_g k_g$; variables are the same as series model.
Carson	$k_e = \frac{1}{4}((3v_g - 1)\,k_g + [3(1-v_g)-1]\,k_s + \sqrt{([(3v_g-1)k_g + [3(1-v_g)-1]k_s]^2 + 8k_s k_g}))$; variables are the same as series model.
Maxwell-Eucken I	$k_e = k_s \frac{2k_s+k_g-2(k_s-k_g)v_g}{2k_s+k_g+(k_s-k_g)v_g}$; variables are the same as series model.
Maxwell-Eucken II	$k_e = k_g \frac{2k_g+k_s-2(k_g-k_s)(1-v_g)}{2k_g+k_s+(k_g-k_s)(1-v_g)}$; variables are the same as series model.

| Kim | $k_e = \frac{(1-v_g)k_s + v_g k_g}{\tau_{dry}}$; where τ_{dry} is tortuosity factor, and the others are the same as series model. |

As for Table 2.3 various effective heat conductivity models can be divided into three classes. The first class is generally used for predicting the general heat conductivity of multiphase material, such as Series and Parallel models. The second class is used for predicting the effective heat conductivity for porous material, and includes the followings: Carson model, Maxwell-Eucken I and Maxwell-Eucken II, which can be applied to different porous materials. The third class is used for predicting effective heat conductivity of foam concrete, such as by Kim's model [58]. The model presented by Kim requires an artificial coefficient to adjust its results.

However, all above models neglect the influences of void pore features, as well as internal heat transferring in void pores.

(2) Specific heat model

Specific heat is heat capability related to material type and its structure. Bentz et al., [69] studied the thermal properties of fly ash mortar and concrete, in which the specific heat can be expressed as:

$$C^p_{conc} = C^p_{water} m_{water} + C^p_{cem} m_{cem} + C^p_{FA} m_{FA} + C^p_{sand} m_{sand} + C^p_{cagg} m_{cagg}$$

(2.1)

where *m* stands for mass fraction, C^p stands for specific heat; and subscripts *conc, water, FA, cem, sand* and *cagg* stand for concrete, water, fly ash, cement, sand and concrete aggregate, respectively.

Zhou et al [70] presented a specific heat model of combined materials, which is expressed as:

$$C^p = \frac{L_a C^p_a + L_b C^p_b}{L_a + L_b}$$

(2.2)

where C^p is specific heat; L is thickness of specimen, and the subscript *a* and *b* are different components of concrete, respectively;

Equation 2.1 is accepted by most researchers, implying that the specific heat of foam concrete can be described as an averaged function of specific heats of the different phases [24] multiplied by their mass fractions.

2.3 Challenges in current research

Although foam concrete has been developed for nearly 90 years [11], many aspects remain to be investigated, such as light weight, thermal insulation and mechanical properties/weight ratio. New research needs to be based on appropriate understanding of the mechanisms of thermal, mechanical and physical/chemical behaviour of foam concrete from the micro-scale to macro-scale [28, 29, 71, 72].

More broadly, the research on foam concrete includes chemical composition design, pore structure design, creep and shrinkage mechanism, process optimization, and failure mechanisms [1, 29].

The two most important factors for foam concrete applications are thermal insulation and compressive strength. Therefore, the factors controlling these two properties and their interdependence are the primary focus of industries and researchers.

Consequently, the main emphasis of this foam concrete research is listed below:

1) How can the pore structure features be quantitatively and accurately described?
2) Can a relationship between irregular pore structure features and properties be established?
3) Can an effective numerical design method be developed to control the pore structure that has low cost and high efficiency instead of traditional experimental methods?

Establishing relationships between void pore features and compressive strength/thermal insulation is a complex issue because pore features including pore

shape, pore size and pore size distribution must all be considered [9, 14-16, 25, 73]. Researchers have found it difficult even to quantitatively describe pore features.

2.3.1 The status of heat transfer research

The existing heat transfer models for foam concrete neglect the inner radiation within the void pore. It is a difficult process to find a model that quantitatively considers not only macro-pore features but also inner radiation. The influences of pore features on heat transfer including conductivity, convection and radiation still remain to be established or modified. While the heat conductivity of foam concrete is a key parameter related to heat transfer, features of the existing modelling methodologies are provided in Figure 2.3.
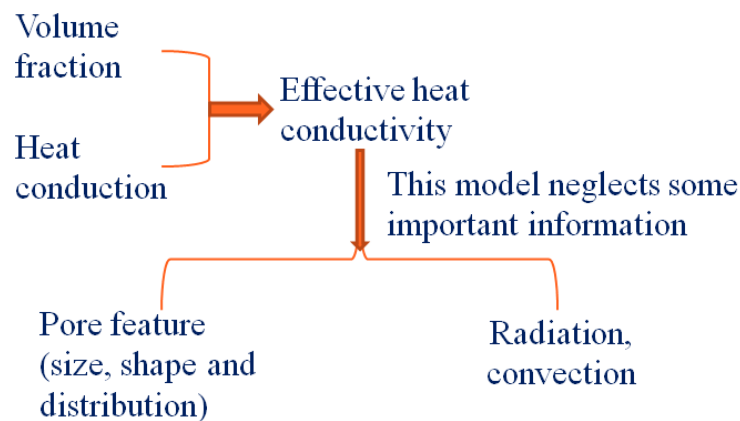
Figure 2. 3 Shortcomings of current heat conductivity method

As illustrated in Figure 2.3, the existing modelling methodology for the effective heat conductivity is based on pore volume fraction and heat conduction only, which neglects the impact of pore features, such as inner radiation and convection in void pore.

2.3.2 Compressive strength

Mechanical properties, especially compressive strength of foam concrete, decline as the void and pores volume fraction increases in general. However, there has been little quantitative relationship published to describe the influences of pore features on compressive strength as most of models focused on the relationship between pore volume fraction and compressive strength [1, 7, 13, 39]. This reflects the difficulty

in identifying and quantifying void pore features, such as pore size, size distribution, pore area fraction, and pore separation [15, 16].

(1) Experimental research

Many previous researchers have used the experimental approaches to study compressive strength [7, 9, 13, 15, 39, 45]. The experimental method is a direct way to provide a relationship between pores features in foam concrete and compressive strength, but at a higher cost than theoretical analysis and numerical simulation methods. Furthermore, the experimental method takes long times to get result due to concrete inherit slow-hardening properties. Moreover, results are always affected by experimental conditions, such as temperature, moisture content, curing time *etc*, all of which affect the precision of experimental results. At present, most research on foam concrete continues to use the experimental approach to study the relationship.

Because the pores in foam concrete are irregular shape and their size ranges from μm to mm [15, 74], the influence of pores size on compressive strength is difficult to quantify. Using EPS beads to replace the foam in foam concrete can directly study the size effect. Expanded polystyrene (EPS) has a spherical shape for which the radius can be selected by a sieving method, and it is easy to measure its size. Further, EPS has far lower strength compared with concrete, and consequently can be regarded as pores embedded into concrete matrix. Therefore, using EPS beads to substitute for the pores in concrete is an effective way to study the pore size impact on compressive strength. Hence it can be regarded as an idealized material of uniform size in concrete.

EPS concrete is a kind of lightweight concrete in which EPS beads are embedded into cement paste to imitate void to reduce its density significantly. EPS concrete with low density and high thermal insulation properties arouses great interest from both industries and research institutes around the world for its potential wide applications. These include energy saving construction material, sub-base material for pavement and railway track beds, construction material for floating marine structures, energy absorbing material for the protection of buried military structures and fenders in offshore oil platforms [75-77].

Although there are lots of advantages and potential applications, the mechanical properties of EPS concrete are one of the weaknesses [78-80]. In general, mechanical properties of EPS concrete declines as its density decreases. In the past decade, there were many researchers investigating to EPS concrete [76, 78, 81-83] with many publications related to mechanical properties. The relationship between EPS beads and its mechanical properties would aid the design of EPS concrete to better fit these applications, especially density, heat insulation and mechanical properties.

K.Miled et al [78, 79] studied the size effect of EPS beads on the compressive strength and failure of EPS concrete. In their model[78], EPS beads were assumed to be distributed uniformly within the concrete, and then the damage initiation and distribution in the specimen were calculated. Their research work indicated that there was no size effect on the compressive strength. However, their model was just a 2D model that couldn't reflect the 3D dimensional situation. Uniform distribution of EPS beads does not reflect real illustration. In 2007, K.Miled [79] et al used the experimental method and numerical method to investigate the influences of size effect of EPS beads on compressive strength and reported that a difference of compressive strength between the big size and small size of EPS beads could reach 40% with the same density. They concluded that the finer EPS beads produced the higher compressive strength.

2014 Ning Liu et al [80] studied the impact of size on the compressive strength using numerical fitting method, in which they utilised an exponent equation to describe the relationship among the EPS volume fraction, EPS size and compressive strength.

In 2005 A.Laukaitis et al [84] studied the effect of size on the compressive strength of EPS concrete. Their work demonstrated that the fine polystyrene yielded the highest compressive strength and that crumbled polystyrene had the lowest compressive strength. In their paper, compressive strength was expressed as a power function of density corresponding to the three kinds of polystyrene. However, all the samples' compressive strengths were less than 1 MPa, and the difference for

compressive strength between the fine polystyrene and large polystyrene samples was about 0.1~0.2 MPa.

In 2006 Daneti Saradhi Babu et al[75] investigated the effect of EPS on compressive strength, split tensile strength, moisture migration and absorption, for which they derived a fitting function between compressive strength and EPS concrete density. Their research didn't explain from the influence of EPS bead size on the compressive strength.

There was also others research on the EPS structure [83], fabrication and physical properties [81], and numerical simulation [85, 86].

Although there has been some research focused on the effects of EPS bead size on compressive strength, both theoretical and numerical methods are still necessary for quantitative EPS concrete research.

  (2) Theoretical analysis method

Theoretical analysis is an economical means to research compressive strength. Many researchers have applied stress analysis method to the analyse of the failure models of concrete[87, 88]. Although the theoretical analysis method is based on physical model, it requires strong mathematical skills and this method still has problem in dealing with complex structures and multi-axis stress state or 3-dimensional problems, which limits its application to simple structures.

(3) Numerical simulation method

Numerical simulation is a highly efficient and low cost researching method, which can also solve complex structural problems. Finite element method (FEM) is one of the most widely used numerical methods in the concrete field [83, 89-92]. Others adopted FEM to study the influence of aggregates on failure [91], and some researchers used FEM to study the impact of inner pore structures on the macro-scale stress-strain relationship [89, 93]. However, precise calculation by FEM depends on the meshed size of grid unit. Finer meshed size can make results more precise, but employs longer calculation time.

Artificial neural network is another widely used method. Some researchers have adopted an artificial neural network method to investigate the influences of chemical

composition on compressive strength[94-96], others have adopted this method to study the shrinkage of concrete[97]. Additionally, there have been some researchers using this method to other aspects of concrete [98, 99]. However, there is less research with this method on the relationship between pore features and compressive strength. Although artificial neural network is a highly efficiency research method, it uses mathematical method to establish the correlation between each input parameter and output results, which lacks the physical meaning to explain the correlation mechanism.

There are also other numerical simulation methods used in concrete field[100, 101], such as numerical fitting [101] and fractional factorial method[100]. All these numerical simulation methods present researchers with an economic and efficient tool to quantitatively describe concrete problems. Hence, using numerical simulation together with experimental verification can save the research costs and enhance research efficiency.

2.4 Summary

Foam concrete has great market demand for its attractive physical properties. Consequently, this thesis had two main aims:

(1) To quantitatively describe pore features;

(2) To establish the relationship between pores features and physical properties, which include two aspects– thermal insulation and compressive strength.

The approaches employed to above these aims are theoretical deduction, numerical simulation and experimental method, which are utilized to determine quantitatively the impact of pore features on compressive strength and thermal insulation. To achieve the aims, EPS beads is employed to build the correlation between beads size and compressive, and the random distribution model is adopted to describe the EPS distribution in concrete matrix and then the FEM method is used to predict the compressive strength, and a theoretical model of heat conductivity model of foam concrete and its fire resistance is also compared with dense concrete. Because pore

volume fraction and pore size can be measured easily, therefore in the thesis, the impact of pore volume fraction and pore size are studied.

CHAPTER 3 COMPRESSIVE STRENGTH OF FOAM CONCRETE

3.1 Experimental Design

To minimize the influence caused by other factors, the water/cement (*w/c*) ratio is kept constant and the volume of EPS is varied. It is expected that the effect of *w/c* ratio will be similar in all samples.

The flowchart (Figure 3.1) documents the steps used in making the EPS concrete sample.
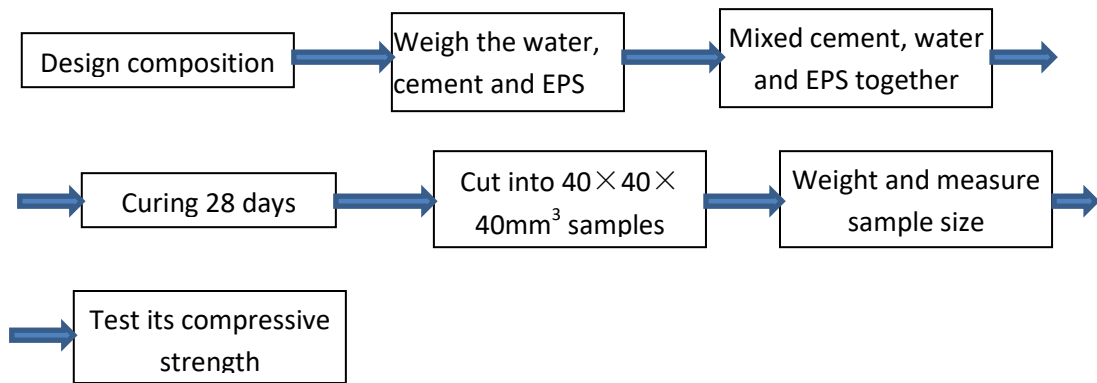
Figure 3. 1 Flow chart of EPS concrete sample preparation

The procedure is followed to the manufacture of the EPS concrete samples for compressive strength testing. In order to investigate the influence of the EPS volume fraction on compressive strength of EPS concrete, 5 groups of EPS volume fractions are designed ranging from 10% to 50%. EPS bead radii are fixed at 1.3mm and 3.5 mm.

The following EPS beads and volume fraction are adopted in determination of compressive strength (Table 3.1).

Table 3. 1 Experiment design

	V_f	10%	20%	30%	40%	50%
d						

2.68mm	√	√	√	√	√
7 mm	√	√	√	√	√

V_f is volume fraction of EPS; d is the EPS diameter; √ sample employed.

The volume fraction of EPS beads in EPS concrete is determined as:

$$V_f = \frac{\rho_c - \rho_{mix}}{\rho_c - \rho_{EPS}}$$

$$(3.1)$$

where ρ_c is cement density, which is 3150kg/m^3; ρ_{EPS} is EPS bead density, which is 18kg/m^3; and ρ_{mix} is EPS concrete density.

According to Equation 3.1, if the volume fraction of EPS bead is known, the density of EPS concrete can be derived as:

$$\rho_{mix} = \rho_c - (\rho_c - \rho_{EPS})V_f \quad (3.2)$$

Equation 3.2 can be also rewritten as Equation 3.3 for a unit volume of EPS concrete.

$$\rho_c(1 - V_f) + \rho_{EPS}V_f = m = \rho_{mix} \quad (3.3)$$

Therefore, to mix a certain volume fraction of EPS concrete, the mass ratio for the EPS concrete can be expressed as:

$$m_{mix} = \rho_{mix}V = \rho_c(1 - V_f)V + \rho_{EPS}V_fV \quad (3.4)$$

A $40 \times 40 \times 40$mm^3 cubic sample is adopted to ensure a reasonable EPS distribution. The ratio of cement/water is set as 0.3, and the water lost during curing is 1/3 of total water weight, which is obtained by measuring the dried sample. So the weight of EPS beads can be determined.

The different volume fractions of EPS in EPS concrete are listed in Table 3.2.

Table 3. 2 Component composition for different volume fraction of EPS concrete

EPS V_f (%)	$\rho_{mix} = \rho_c - (\rho_c - \rho_{eps})V_f$	Cement density	EPS density	mass of cement (g)	water (g)	EPS(g)
0	3150	3150	18	2423	727	0
10	2837	3150	18	2181	654	2.08
20	2524	3150	18	1938	582	4.15
30	2210	3150	18	1696	509	6.23
40	1897	3150	18	1454	436	8.31
50	1584	3150	18	1212	363	10.38

After casting, the samples are left in mould at an ambient temperature for 24 hours to ensure adequate strength for handling. After demoulding the samples are water submerged for 28 days.

Compressive testing is carried out on a MTS Insight test machine with a maximum 100 kN loading force as illustrated in Figure 3.2.

Figure 3. 2 Compressive strength test machine

The loading force and displacement are recorded during the test. When the cross area of the sample is input into the computer, compressive stress and strain can be

determined directly, and then Young's modulus can be deduced by using the strain and stress data.

As displayed in Figure 3.3, the strain during the compressing process may be contributed by the steel plates, the wood plate and the concrete sample. However, the test machine is unable to distinguish the strain contribution by each of these. In order to accurately measure concrete sample strain, strain is measured by a strain gauge (made by Tokyo Sokki Kenkeujo Co.Ltd), its type PFL-20-11-3LT. The strain gauges are attached to the both sides of specimen by glue as illustrated in Figure 3.3.

The wireline is connected with a computer to record instantly strain data. In order to reduce the top and bottom faces friction with wooden plates, a pair of Teflon layers is laid on both the top and bottom sides of the concrete sample.
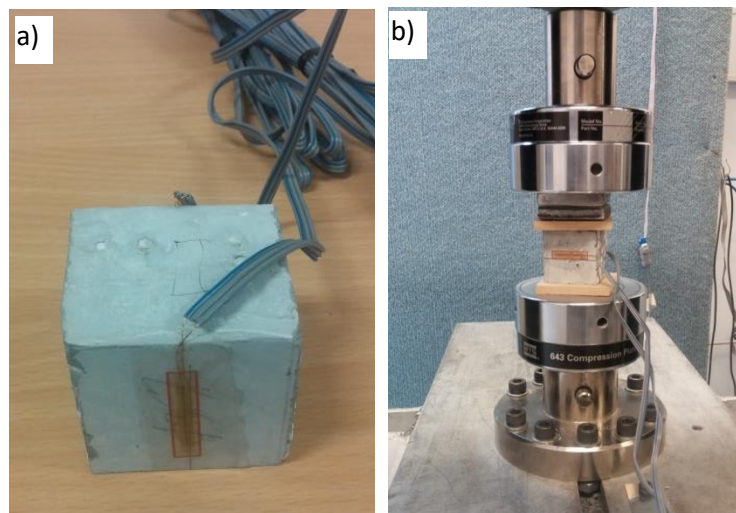
Figure 3. 3 Strain gauge on the concrete sample, a) is the strain gauge position, b) concrete sample with strain gauge on the experimental platform

In Figure 3.3 a), there are two centred strain gauges pasted to front and back face of the sample, and the two strain gauges are in the same direction. Using strain gauges, strain is measured directly both in vertical and horizontal dimensions. In our experiment, both horizontal and vertical directions of strain are measured during compression. The top punch dropping rate is set as 1mm/min.

Figure 3. 4 Strain gauges on the sample

Since the horizontal direction strain is very small ranging from 0 to 5.00×10^{-4} (experimental data) in contrast to vertical strain which ranged from 0 to 6.0×10^{-3}. So the horizontal direction strain is neglected. In this thesis volume fraction ranged from 10% to 50% EPS beads are employed to view the strain during compressive strength test.

3.1.1 Auxiliary device for measuring compressive strength

During the initial experiments, it is discovered that if the top side of sample is not parallel to the bottom side of sample, then the measured compressive strength will be in error and much lower. Therefore, an improved method for measuring compressive strength is designed to avoid this. Details are shown in Figure 3.5.
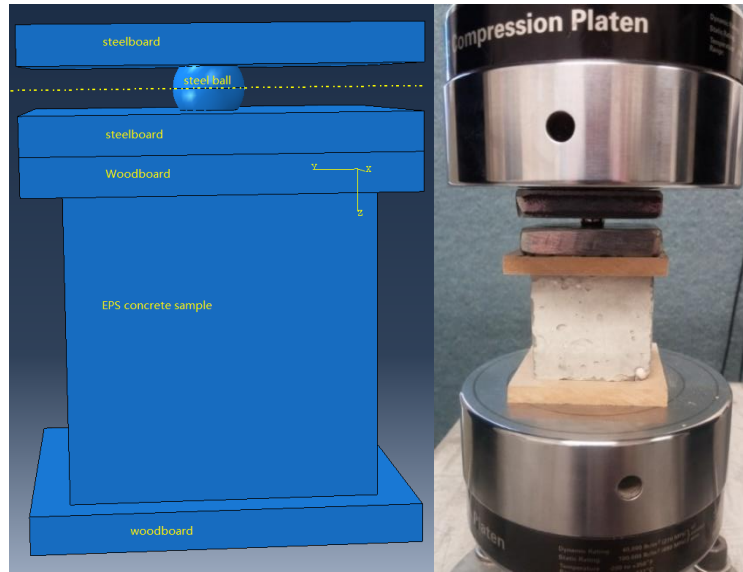
Figure 3. 5 Assembly facility for compression testing

Here in Figure 3.5 a schematic figure of facility is pictured on the left and the actual experimental facility on the right. Firstly, wooden plates are placed on both the top and bottom sides of samples to minimise potential influences of uneven faces. On the top wooden plate, a set of steel plates separated by a steel ball is placed centrally. To avoid the steel ball movement, a concave depression is machined in facing sides of the steel plate centre. Using the set of steel plates, the loading force is applied to the sample body uniformly, and the problem of nonparallel opposed faces resolved.

3.1.2 EPS Beads Measurement

Accurately measuring the size and density of EPS beads is crucial in order to precisely design the volume fraction of EPS concrete. To permit relatively precise results, 10 EPS beads are selected for an averaged diameter. Similarly, for the determination of density, 10 EPS beads are employed for total weight estimation. Then the density of EPS beads is calculated by

$$\rho = W_{total}/\Sigma(\frac{4\pi r_i^3}{3}) \tag{3.5}$$

where r_i is the radius of the ith EPS bead, W_{total} is the total weight of 10 EPS beads.

The ten EPS beads are depicted in Figure 3.6.
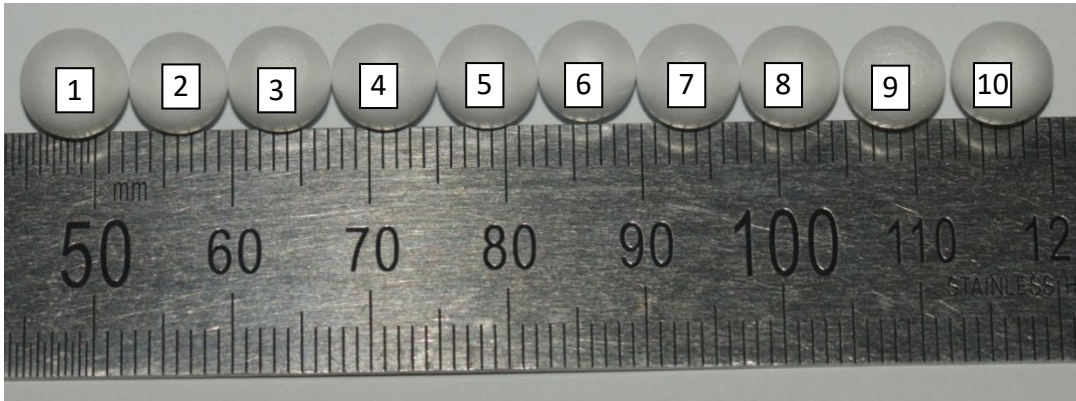
Figure 3. 6 Image size of Ø 7mm EPS beads on A4 paper and magnified by 3.5 times In order to accurately measure the size of each EPS bead, the image of these EPS beads is magnified and printed on A4 paper, and the ruler is employed to measure each EPS bead size. Image sizes of 7mm EPS beads on A4 paper are listed in Table 3.3. According to these measured values and the zoom ratio, the averaged diameter of EPS beads is obtained as $\bar{d} = \frac{\sum d_i}{n} \approx 7.04$mm.

The image of Ø2.68 mm EPS beads is illustrated in Figure 3.7.
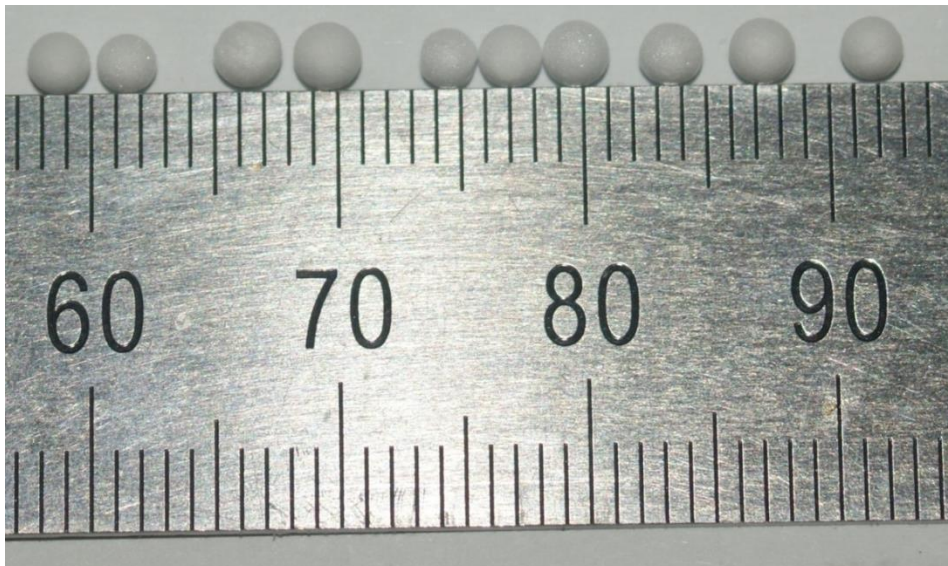
Figure 3. 7 Image size of Ø 2.68 mm EPS beads on A4 paper and magnified by 6 times

The similar method is also used to measure the Ø 2.68 mm EPS beads size, and the measured size on A4 paper is listed in Table 3.3. The zoom ratio is 1:6. According to these measured values and the zoom ratio, the averaged diameter of EPS beads is given as $\bar{d} = \frac{\sum d_i}{n} \approx 2.68mm$.

Accurately scaling the EPS weight is also an important step for density measurement, which is a key step for designing the EPS volume fraction. Therefore, a total of 10 EPS beads are used and weighted together so as to reduce any artificial error. Weights are determined with a MonoBloc AB204-S analytical balance, a brand of Mettler Toledo Company (the minimum weight unit is 0.1 mg, which matches the test requirement). The weights for both $\Phi 7mm$ and $\Phi 2.68$ mm EPS beads is displayed in Figure 3.8.

a)   d=2.68 mm;   b) d=7.04 mm

Figure 3. 8 Real weight of 10 EPS beads of different size

Figure 3.8 shows the real weight of 10 EPS beads, in which a) is diameter Ø2.68 mm EPS beads, b) is diameter Ø7.04 mm EPS beads. The total weight of ten Ø2.68 mm EPS beads is 0.0030g, while the weight of Ø7.04 mm EPS beads is 0.0285 g. According to Equation 3.3, the densities of Ø2.68 mm and Ø7.04 mm EPS beads are calculated as 30.58 kg/m^3 and 15.54kg/m^3, respectively. The density of the small EPS beads is nearly twice of the large EPS beads. The measured data are listed in Table 3.3.

Table 3. 3 Real diameter and density of Ø 7 mm and Ø 2.68 mm EPS beads

	Image of Ø7 mm size (1:3.5)	real size	Ø7 mm Volume	Image of Ø2.68 mm size (1:6)	Ø2.68 mm real size	Ø2.68 mm Volume	Ø7 mm density (kg/m^3)	Ø2.68 mm density (kg/m^3)
1	26	7.43	214.64	15.5	2.58	9.02	15.54	30.58
2	24	6.86	168.82	15	2.5	8.18		
3	25	7.14	190.82	17	2.83	11.91		
4	25.5	7.29	202.49	17.5	2.92	12.99		
5	24.5	7	179.59	14.5	2.42	7.39		
6	23.5	6.71	158.49	16	2.67	9.93		
7	25	7.14	190.82	17.5	2.92	12.99		
8	24	6.86	168.82	15.5	2.58	9.03		
9	24.5	7	179.59	16.5	2.75	10.89		
10	24.5	7	179.59	15.5	2.58	9.03		
sum			1833.68			101.36		

3.2 Experimental Results and Analysis

3.2.1 Experimental result

Some of the experimental results are listed in Table 3.4.

Table 3. 4 EPS concrete samples data

Ø7mm	Length (mm)	Width (mm)	Height (mm)	Weight (g)	Density (kg/m3)	Maximum Force (KN)	Compressive Strength (MPa)
10%	41.92	42.83	40.06	129.81	1804.76	53.66	29.89

20%	44.80	40.65	40.05	122.04	1673.27	47.87	26.28
30%	41.45	42.24	39.92	100.99	1444.95	32.99	18.84
40%	42.13	42.69	39.92	96.71	1346.96	20.19	11.22
50%	42.40	42.01	40.02	68.80	965.18	8.34	4.68
2.68mm							
10%	42.19	41.36	40.04	140.01	2003.96	93.01	53.30
20%	41.61	40.85	39.84	130.20	1922.70	84.58	49.76
30%	40.83	40.55	39.85	117.53	1781.37	63.03	38.07
40%	43.41	41.87	40.04	122.24	1679.65	56.25	30.95
50%	38.93	41.62	39.65	95.56	1487.51	39.94	24.65

Using these experimental data, compressive strength under the different density and EPS beads size is illustrated in Figure 3.9.
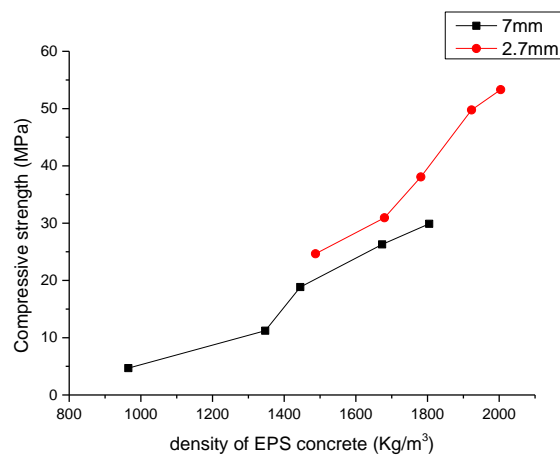
Figure 3. 9 experimentally determined relationship between compressive strength and density of EPS concrete with different EPS beads diameter

In Figure 3.9, compressive strength of EPS concrete at the different densities and diameters. The red circle points represent the compressive strength of EPS concrete containing Ø2.68 mm EPS beads at different volume fraction. The blue square points are the compressive strength of EPS concrete containing Ø7 mm EPS beads at different EPS volume fraction. As the concrete density increases, compressive strength increases in both EPS concretes. With the same concrete density, the EPS concrete containing smaller EPS beads has a higher compressive strength than that containing larger EPS beads.

The failure images of different size and volume fraction EPS concrete are depicted in Table 3.5.

Table 3. 5 Compressing figure of EPS concrete sample
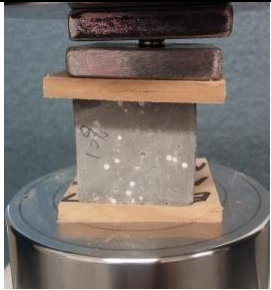
Ø7mm (%)	photo	Ø2.68mm(%)	photo
10		10	
20		20	
30		30	
40		40	
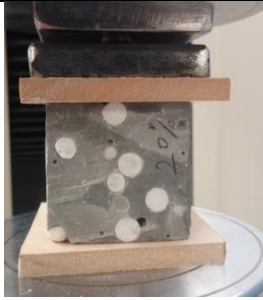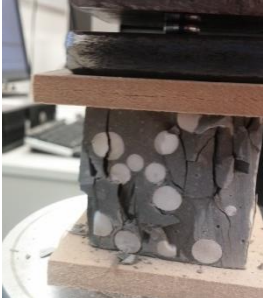
50   50

From Table 3.5 it can be seen that the concrete with 2.68mm EPS beads is easier to crack into small fragments, while the concrete with 7mm EPS beads breaks up into big fragments. Under the same volume fraction, there are more 2.68mm EPS beads than that containing 7mm EPS beads in concrete, and when failure occurs between EPS beads, the more EPS beads in a certain volume causes the smaller fragments.

3.2.2 Experimental results analysis

(1) Compressive strength of EPS concrete containing Ø2.68 mm EPS beads

Utilizing numerical method, the fitting curve for EPS concrete containing Ø2.68 mm EPS beads is drawn as Figure 3.4, and fitting parameters is listed in Table 3.4, in which a power function is employed.
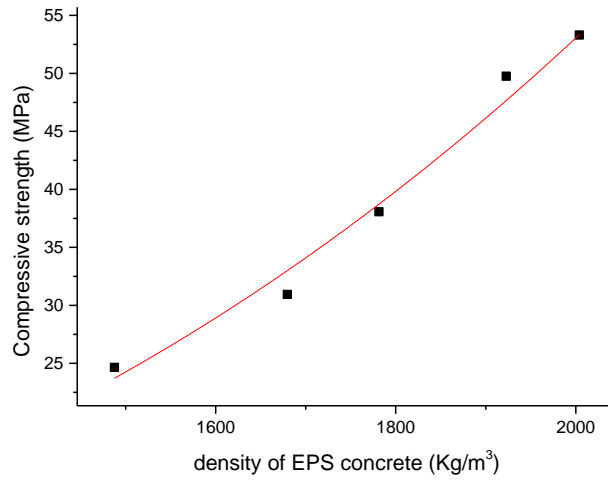
Figure 3. 10 Fitting curve of compressive strength of diameter Ø 2.68mm EPS concrete

Figure 3.10 shows the fitting curve of compressive strength based on the experimental results, in which the black squares represent experimental compressive strength, and the line stands for the fitting curve. The curve fits nicely to experimental results.

For EPS concrete with Ø2.68 mm EPS, Table 3.6 presented parameters give the following relationship for compressive strength:

$$f_{2.68} = a * \rho^b \tag{3.6}$$

where $f_{2.68}$ is the compressive strength of EPS concrete containing Ø2.68 mm EPS beads, ρ is EPS concrete density, and coefficient *a* and *b* can be obtained from Table 3.6, so $f_{2.68} = 5.58 \times 10^{-8} \times \rho^{2.72}$.

Table 3. 6 Fitting parameter of diameter 2.68 mm EPS concrete

	a		*b*		Statistic	
	Value	Standard Error	Value	Standard error	Reduced Chi-Sqr	Adj.R-Squr
Compressive	5.58E-8	9.83E-8	2.72	0. 023	3.31	0.98

strength

The fitting parameters of the curve are listed in Table 3.6, and in the top row *a* and *b* represent the coefficient of power function. The curve fits the experimental results well, in which R-square value reaches 0.98, very close to 1.

For EPS concrete with Ø2.68 mm EPS beads, Table 3.6 presented parameters give the following relationship for compressive strength:

$$f_{2.68} = a * \rho^b \tag{3.5}$$

Where $f_{2.68}$ is the compressive strength of EPS concrete containing Ø2.68 mm EPS beads, ρ is EPS concrete density, and coefficient *a* and *b* can be obtained from Table 3.6, so $f_{2.68} = 5.58 \times 10^{-8} \times \rho^{2.72}$.

(2) Compressive strength of EPS concrete containing Ø7 mm EPS beads

Similarly, with the compressive strength measured in samples containing Ø7mm EPS beads, the fitting curve and fitting parameter are displayed in Figure 3.11 and Table 3.7.
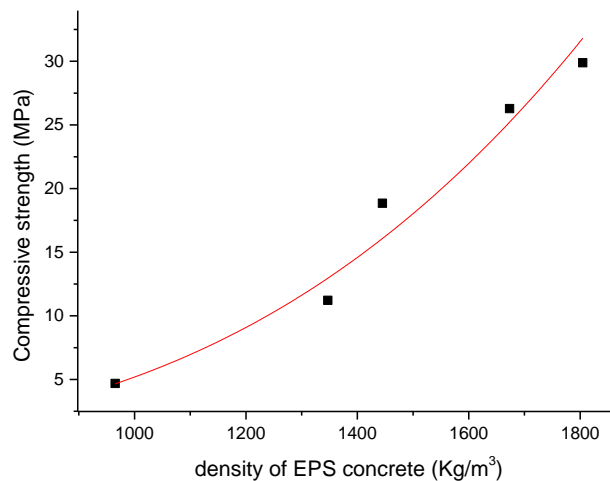
Figure 3. 11 Fitting curve of compressive strength of diameter Ø 7mm EPS concrete

In Figure 3.11, the square dots represent for experimental compressive strength, and the line represents for the fitting curve. The fitting curve closely fits the experimental results. As the density of EPS concrete is increased, the compressive strength increases. When the density is lower than 1000 kg/m^3, the compressive strength is less than 5 MPa. As the density of EPS increases to 1800 kg/m^3, the compressive strength value increases to more than 30 MPa.

When EPS beads diameter is Ø7mm, EPS concrete, compressive strength is given as following relationship:

$$f_7 = a * \rho^b \tag{3.7}$$

where f_7 is compressive strength of EPS concrete containing diameter Ø7mm EPS beads, ρ is EPS concrete density, and coefficient a and b values are obtained from Table 3.7. So the compressive strength by the numerical method is given as $f_7 = 3.20 \times 10^{-9} \times \rho^{3.07}$.

Table 3. 7 Fitting parameter of diameter Ø 7 mm EPS concrete

	a		b		statistics	
	value	Standard error	value	value	Standard error	value
Compressive strength	3.20E-9	1.06E-8	3.07	0.45	5.17	0.95

The fitting curve matches the experimental results well with R-square value of 0.95, very close to 1.

When comparing the two different of EPS concretes compressive strength, the smaller size of EPS beads can result in higher compressive strengths than the coarser EPS beads EPS concrete at the same density.

3.3 Young's modulus

Young's modulus is an important mechanical property, which is expressed as:

$$E = \frac{f}{\epsilon}$$

(3.8)

where E is Young's modulus, f is stress, ϵ is strain.

Stress can be estimated by dividing the loading force over the loading area:

$$\sigma = \frac{F}{S}$$

(3.9)

where F is loading force, S is the area of cross section that is perpendicular to the loading force.

Strain is given by Equation 3.10

$$\varepsilon = \frac{\delta l}{l_0}$$

(3.10)

where $\boldsymbol{\delta l}$ is the reduction of height, which can be recorded by the compressing test machine, and $\boldsymbol{l_0}$ is the initial height of the sample.

3.3.1 Stress-strain relationship

1. Stress-strain relationship and Young's modulus of EPS concrete with Ø2.68mm EPS beads

Stress determined from $f = F/s$ (Equation 3.9). The loading force F is obtained from experimental data, and s is area of sample, which is assumed to be a constant.

The stress-strain relationship of Ø2.68 mm EPS beads with 10% volume fraction is depicted in Figure 3.12.
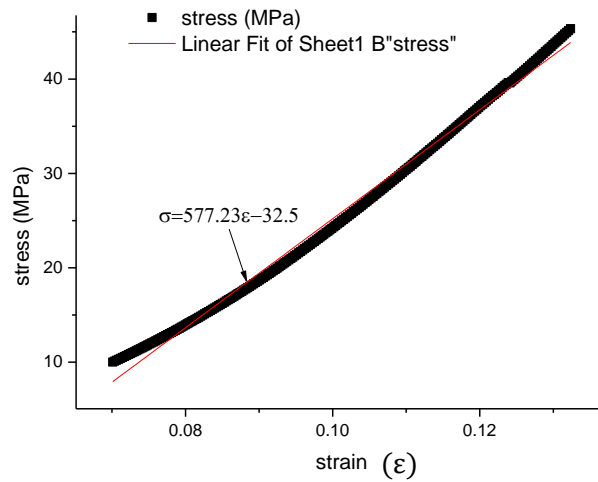
Figure 3. 12 Stress-strain relationship of Ø 2.68 mm EPS beads with 10% volume
fraction

When the strain is less than 0.09, the relationship between stress and strain is
nonlinear. When the strain exceeds 0.09 but less than 0.135, the strain and stress can
be regarded as exhibiting a linear. The maximum stress is 47 MPa. The linearly
fitting relationship between strain and stress is employed in Figure 3.11. Young's
modulus of the EPS concrete containing 10% Ø2.68 mm EPS beads is 577.23 MPa.

The stress-strain relationship of Ø2.68mm EPS beads with 20% volume fraction is
plotted in Figure 3.13.
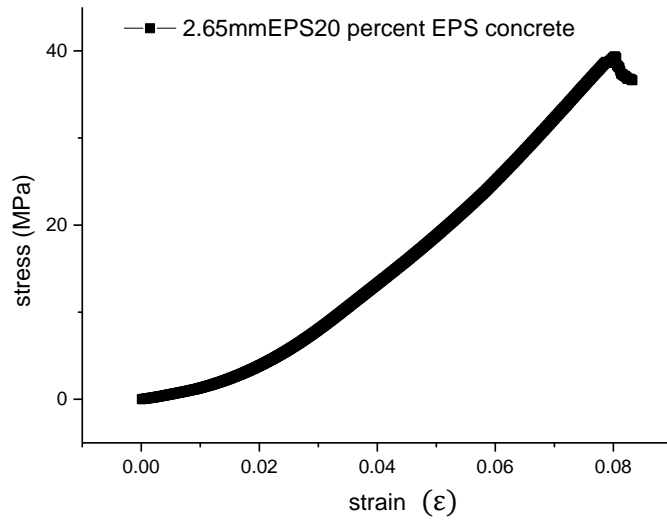
Figure 3. 13 Stress-strain relationship of Ø 2.68 mm EPS beads with 20% volume fraction

When strain is lower than 0.02, the stress increases slowly as the strain increasing. When the strain value exceeds 0.02, the relationship between stress-strain approximates linear relationship and the maximum stress is 40 MPa when the strain is 0.08. According to stress-strain relationship, Young's modulus is $E = \frac{\delta f}{\delta \varepsilon} = 502.27$ MPa.

The stress-strain relationship of Ø2.68 mm EPS beads with 30% volume fraction is evident in Figure 3.14.
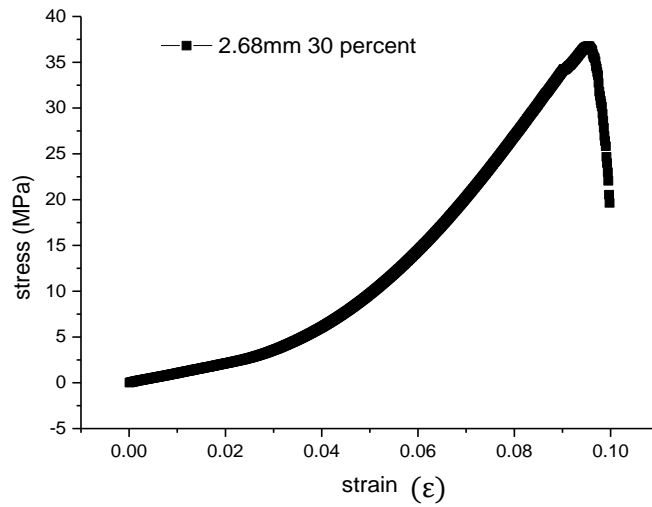
Figure 3. 14 Stress-strain relationship of Ø2.68 mm EPS beads with 30% volume fraction, a) is displacement-force relationship; b) is stress-strain relationship

With strains lower than 0.04, the stress increases slowly as strain increases. When the strain value exceeds 0.04, the relationship between stress-strain approximates a linear relationship, and the maximum stress is 37 MPa when the strain is 0.08. According to the strain-stress relationship, the linear section is regarded as elastic deformation with a Young's modulus value of $E = \frac{\delta f}{\delta \varepsilon} = 609.19$ MPa
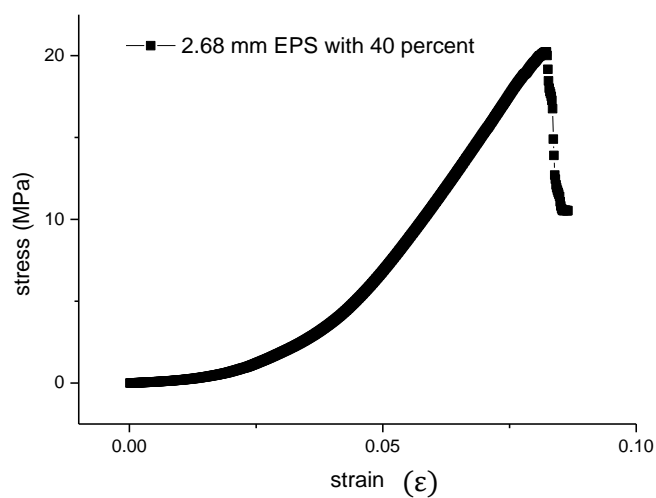
Figure 3. 15 Stress-strain relationship of Ø2.68 mm EPS beads with 40% volume fraction

As the strain is less than 0.04, the stress increases slowly as strain increases. When the strain value exceeds 0.04, the relationship between stress-strain approximate a linear relationship, and the maximum stress is 20 MPa when the strain is 0.08. The linear section can be regarded as elastic deformation with a Young's modulus value of $E = \frac{\delta f}{\delta \varepsilon} = 427.52$ MPa.

2. Stress-strain relationship and Young's modulus of EPS concrete with Ø7.04 mm EPS beads
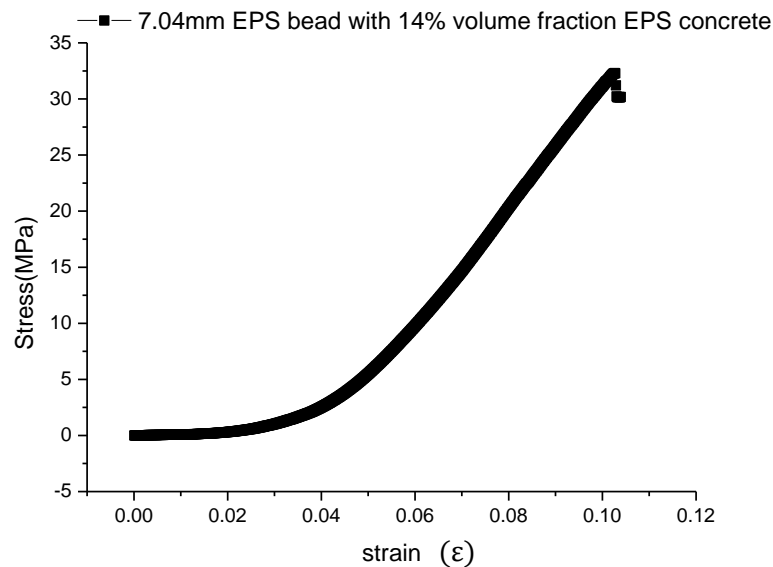
Figure 3. 16 Stress-strain relationship of 14% EPS concrete with Ø7.04 mm EPS beads

At lower strain than 0.05, the stress increases slowly as strain increases. When the strain value is above 0.05, the relationship between stress-strain is nearly linear, and the maximum stress is 32 MPa when the strain is lower than 0.1 with a Young's modulus of $E = \frac{\delta f}{\delta \varepsilon} = 536$ MPa.
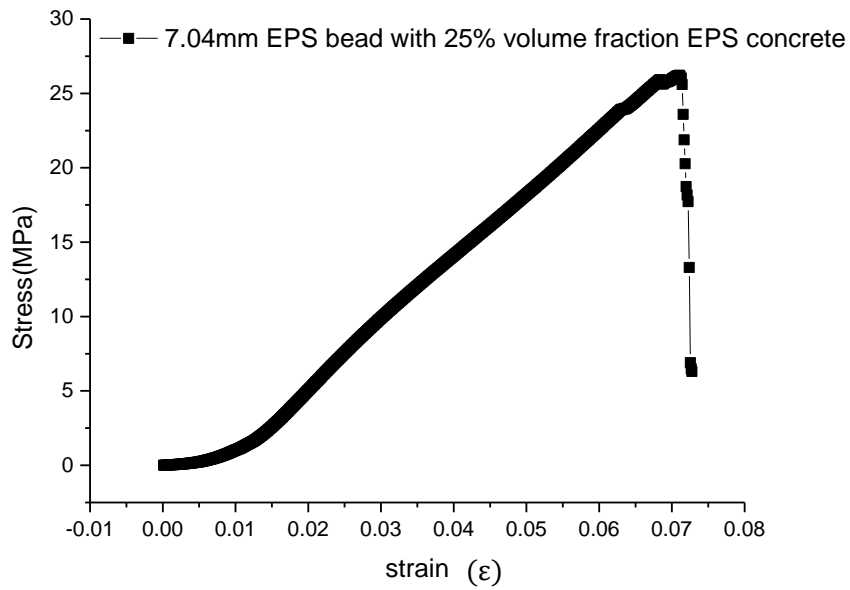
Figure 3. 17   Stress-strain relationship of 25% EPS concrete with Ø7.04 mm EPS beads

The stress-strain relationship of 25% EPS concrete with Ø7.04 mm EPS beads is plotted in Figure 3.17. As the strain is less than 0.01, the stress increases slowly as strain increases. When the strain value is above 0.01, the relationship between stress-strain is close to linear relationship, and the maximum stress is 27 MPa when the strain is 0.07 with a Young's modulus of $E = \frac{\delta f}{\delta \varepsilon} = 438$ MPa.
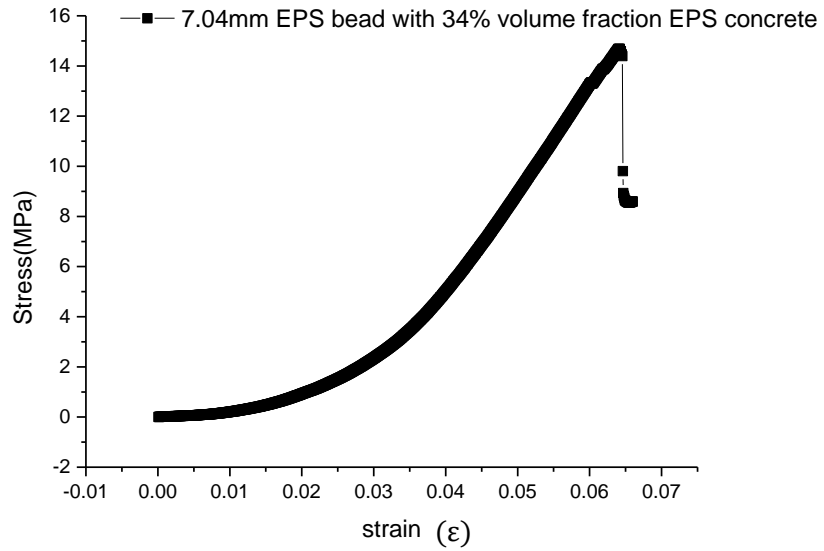
Figure 3. 18   Stress-strain relationship of 34% EPS concrete with Ø7.04 mm EPS beads

The stress-strain relationship of 34% EPS concrete with Ø7.04 mm EPS beads is depicted in Figure 3.18. With the strain values is less than 0.035, the stress increases slowly as strain increases. When the strain value exceeds 0.035, the relationship between strain and stress approximated a linear relationship. When the strain is 0.065, the maximum stress reached 15 MPa with a Young's modulus value of $E = \frac{\delta f}{\delta \varepsilon} = 408$ MPa.
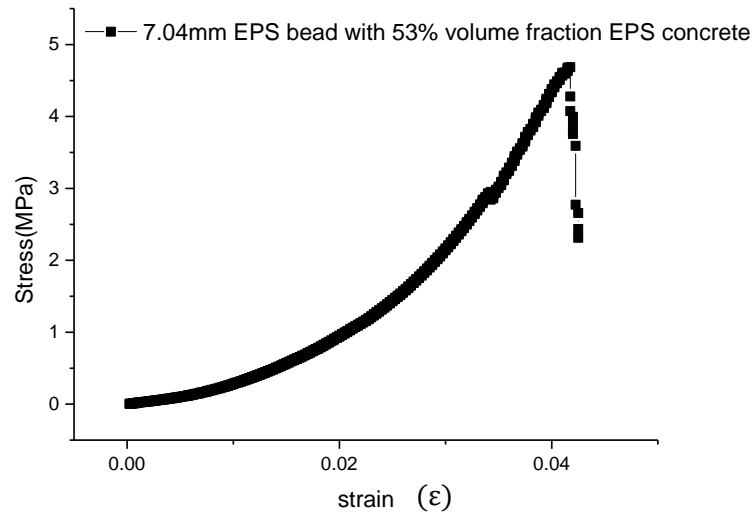
Figure 3. 19   Stress-strain relationship of 53% EPS concrete with 7.04 mm EPS beads

The stress-strain relationship for 53% EPS concrete with Ø7.04 mm EPS beads is depicted in Figure 3.19. As the strain is lower than 0.03, the stress increases slowly. When the strain value is above 0.03, the relationship between stress-strain is nearly linear, and the maximum stress is 5 MPa when the strain is 0.04 with a Young's modulus is given: $E = \frac{\delta f}{\delta \varepsilon} = 277$ MPa.

From Figures 3.10~3.19, it can be deduced that the strain of foam concrete is much larger than that of common concrete, and this is attributed to the auxiliary equipment. Firstly, the loading force is exerted on the auxiliary equipment, especially for the wooden plate. Due to its lower strength, the wooden plates contribute a majority part of the strain, which creates higher the strain values. When the strain values greatly exceed the true strain of concrete, the stress value approaches the former calculating value, and Young's modulus is much lower than the real value. This is because the loading force is transferred directly to the sample and there is no loss of force during the pressing process. So, there is no deviation in stress applied on, and strain is the main reason for Young's modulus deviation.

3.4 Relationship between Volume Fraction and Compressive Strength

Throughout the experimental measurements, compressive strength of foam cement is determined by different volume fractions as listed in Table 3.8.

Table 3. 8 Different density of foam concrete

Foam adding percent (mass %)	Density (kg/m^3)	compressive strength (MPa)	Foam Volume fraction
0	1373	48.5	0
1.3	1194	32.2	0.13
3.3	1016	17.4	0.26
5	902	12.6	0.34
6.6	817	9.1	0.41
10	761	8.3	0.45
13	608	4.5	0.56
16	580	3.5	0.58

* The experimental results are provided by Dr Zuhua Zhang

From these data, a numerical fitting method is used and the relationship between the volume fraction and compressive strength for foam concrete established. This is portrayed in Figure 3.20.
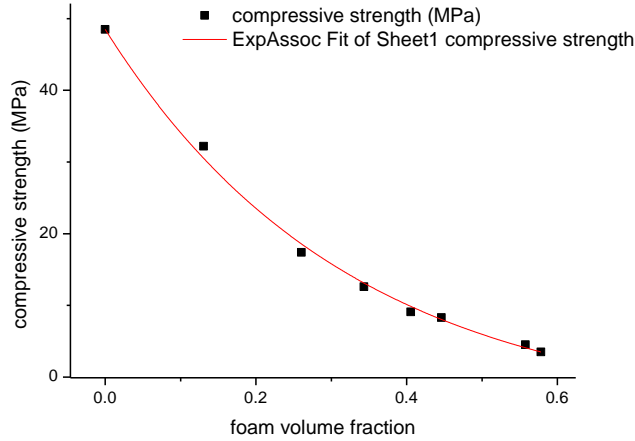
Figure 3. 20 Relationship between compressive strength and volume fraction

The relationship between compressive strength and volume fraction is plotted in Figure 3.20. The squares represent the experimental results; the line is the relationship between the volume fraction and compressive strength from numerical analogue with the expression below:

$$f = 49.00 - 54.10 * (1 - e^{(-V_f/0.31)}) \tag{3.11}$$

where f is compressive strength, V_f is the volume fraction.

The statistics of fitting curve can be seen in Table 3.9.

Table 3. 9 Fitting parameter of compressive strength of foam concrete

	Y_0	A_1	t_1	Statistics	
	Value	Value	Value	Reduced Chi-Sqr	Adj.R-Square
Compressive strength	49.00	54.10	0.31	1.66	0.99

3.5 Model Deduced from Experimental Results for Compressive Strength Related to Pore Feature

In order to reflect the influence of pore feature on the compressive strength of foam cement, pore size distribution, averaged pore size, pore shape factor and pore area fraction are investigated separately.

Initially, the relationship between the mass of foam and the foam volume fraction is measured. Next the relationship between volume fraction and pore size distribution is constructed. Then the relationship between volume fraction and pore shape is constructed. This is then followed by the relationship between volume fraction and pore area fraction. Finally the relationship between pore features and compressive strength is formulated.

When the specimen is made, the compressive strength with different volume fraction of foam mass can be measured by compressive strength test machine, and then specimens with different volume fraction of foam are picked and cut through. The cross section of the specimen can be observed and recorded by optical microscope. Then, the recorded images are counted by image statistics software to determine pore size distribution, pore area fraction, pore shape factor.

According to the experimentally measured data, pore features with different pore volume fractions can be derived in Table 3.10.

Table 3. 10 Pore features and compressive strength

adding foam %(mass)	pore size μm	pore size possibility	pore shape	pore area	compressive strength MPa
0	100	0.88	0.83	0.022	48.5
0	200	0.10	0.73	0.022	48.5
0	400	0.02	0.7	0.013	48.5
0	600	0	0	0	48.5

0	800	0	0.65	0.006	48.5
0	1000	0	0	0	48.5
0	1500	0	0	0	48.5
0	2000	0	0	0	48.5
1.3	100	0.83	0.82	0.034	32.2
1.3	200	0.13	0.62	0.056	32.2
1.3	400	0.03	0.44	0.050	32.2
1.3	600	0.003	0.27	0.015	32.2
1.3	800	0	0.41	0.005	32.2
1.3	1000	0	0.42	0.004	32.2
1.3	1500	0	0.32	0.005	32.2
1.3	2000	0	0	0	32.2
3.3	100	0.683	0.8	0.026	17.4
3.3	200	0.223	0.65	0.075	17.4
3.3	400	0.088	0.43	0.104	17.4
3.3	600	0.005	0.27	0.017	17.4
3.3	800	0.001	0.22	0.005	17.4
3.3	1000	0	0.23	0.002	17.4
3.3	1500	0	0	0	17.4
3.3	2000	0	0	0	17.4
5	100	0.615	0.79	0.015	12.6
5	200	0.200	0.7	0.043	12.6
5	400	0.132	0.52	0.109	12.6
5	600	0.037	0.31	0.089	12.6
5	800	0.013	0.22	0.058	12.6
5	1000	0.002	0.17	0.019	12.6
5	1500	0.001	0.09	0.009	12.6
5	2000	0	0	0	12.6

6.6	100	0.629	0.79	0.010	9.1
6.6	200	0.174	0.69	0.028	9.1
6.6	400	0.118	0.52	0.076	9.1
6.6	600	0.039	0.32	0.074	9.1
6.6	800	0.021	0.21	0.079	9.1
6.6	1000	0.008	0.14	0.052	9.1
6.6	1500	0.008	0.1	0.0871	9.1
6.6	2000	0.003	0.06	0.090	9.1
10	100	0.674	0.8	0.006	8.3
10	200	0.153	0.68	0.020	8.3
10	400	0.089	0.51	0.047	8.3
10	600	0.039	0.33	0.058	8.3
10	800	0.019	0.18	0.059	8.3
10	1000	0.008	0.14	0.041	8.3
10	1500	0.010	0.08	0.099	8.3
10	2000	0.007	0.05	0.207	8.3
13	100	0.683	0.8	0.005	4.5
13	200	0.131	0.69	0.014	4.5
13	400	0.096	0.57	0.040	4.5
13	600	0.035	0.4	0.040	4.5
13	800	0.017	0.28	0.041	4.5
13	1000	0.013	0.21	0.055	4.5
13	1500	0.014	0.16	0.099	4.5
13	2000	0.010	0.07	0.285	4.5
16	100	0.734	0.8	0.004	3.5
16	200	0.125	0.66	0.010	3.5
16	400	0.077	0.56	0.023	3.5
16	600	0.024	0.42	0.023	3.5

16	800	0.008	0.3	0.013	3.5
16	1000	0.010	0.25	0.029	3.5
16	1500	0.009	0.17	0.048	3.5
16	2000	0.012	0.06	0.510	3.5

*The experimental data are provided by Dr Zuhua Zhang at USQ

3.5.1 Pore Size Distribution and Average Pore Size

An exponential function is used to relate the added foam content to pore size distribution, as expressed below:

$$y(x) = \exp(a + bx) \tag{3.12}$$

where *a* and *b* are constant, *y(x)* is probability of pore size, *x* is pore size.
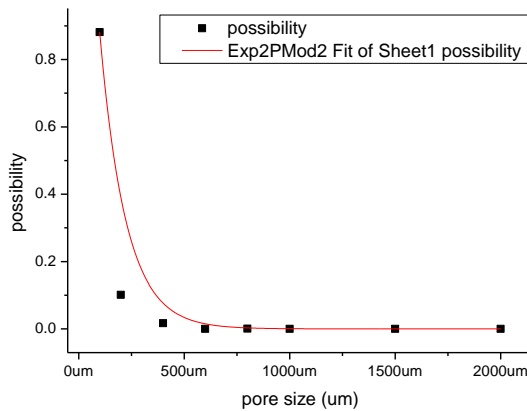
a) $V_f = 0$

b) $V_f = 0.13$

b) $V_f = 0.26$

d) $V_f = 0.34$

e) $V_f = 0.41$ f) $V_f = 0.45$

g) $V_f = 0.56$ h) $V_f = 0.58$
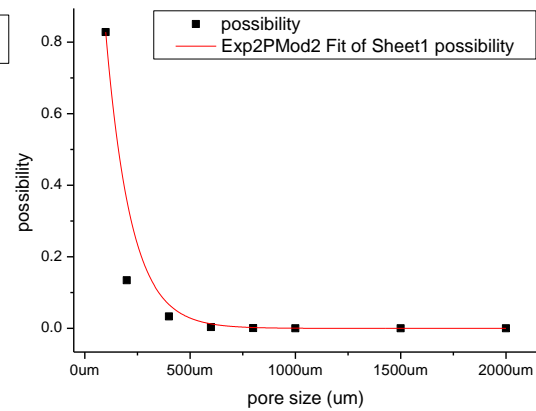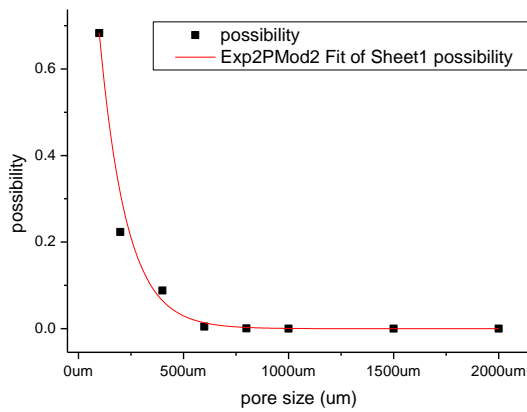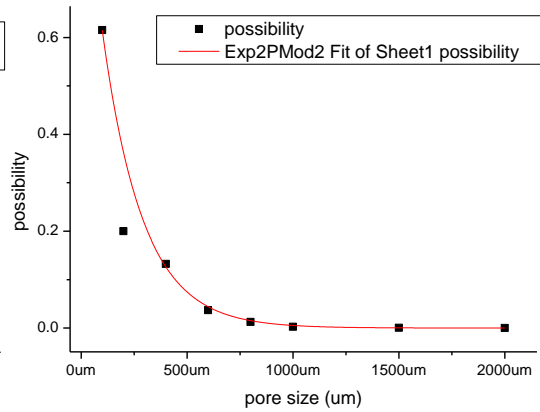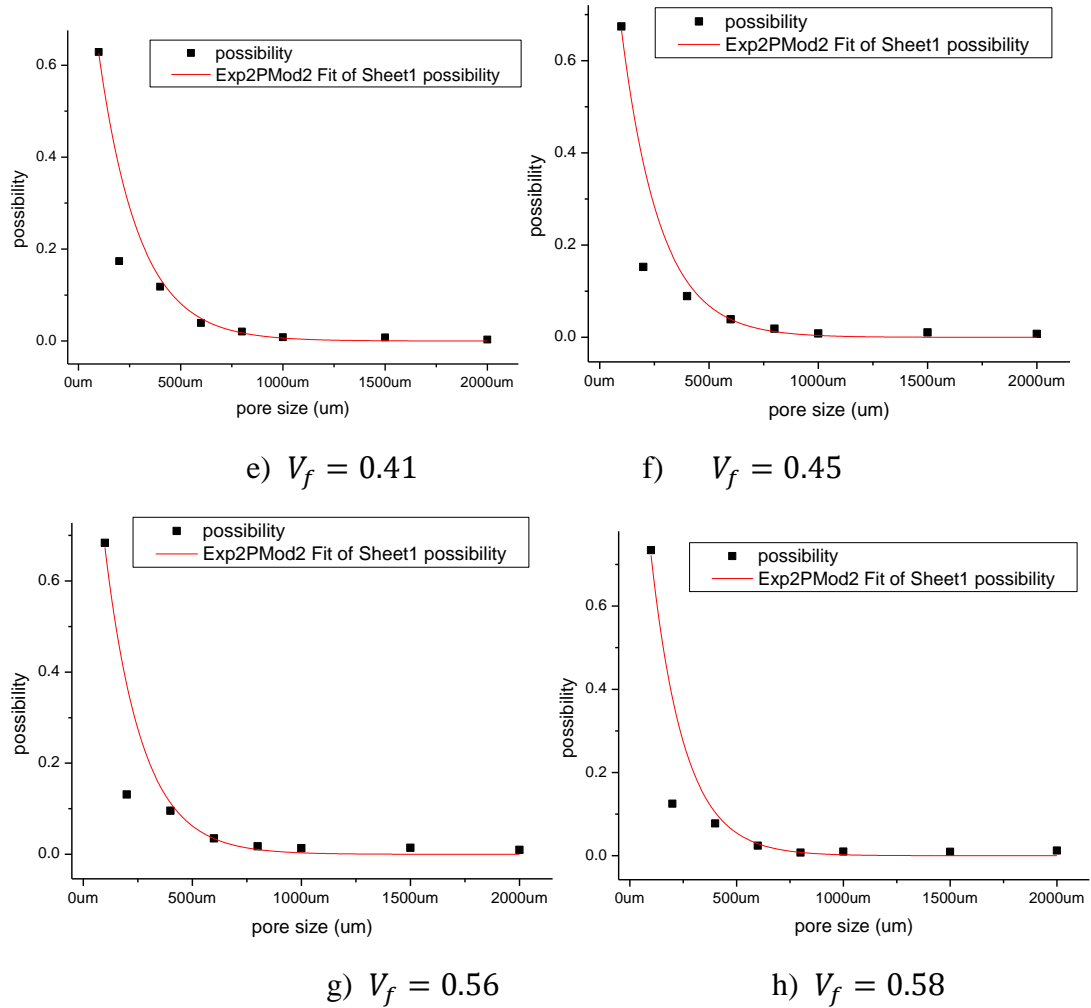
Figure 3. 21 Pore size distribution with different volume fraction

The pore size distributions with different pore volume fractions are depicted in Figure 3.21. The squares represent the experimental results, and the line is the fitting curve, in which a) $V_f = 0$, b) $V_f = 0.13$, c) $V_f = 0.26$, d) $V_f = 0.34$, e) $V_f = 0.41$, f) $V_f = 0.45$, g) $V_f = 0.56$, h) $V_f = 0.58$. When no foam is introduced into the concrete, more than 98% of pores are less than 0.5mm, and 88% of pore sizes are approximately 100μm and 10% of the pore size are 200μm. As the pore volume fraction increases, the percent of 100μm pores decreases gradually from 83% at $V_f = 0.13$ to 62% at $V_f = 0.34$, and then the percent of 100μm pores keeps nearly same. One the contrary, the percent of pore with over 600μm increases gradually as the pore volume fraction increases. In Figure 3.21, as the pore

volume fraction increases continuously, the percentage of pore size ranging from 100 μ m to 400 μ m remains nearly constant, and the percentage of pore size over 800 μ m shows little increase. Also, the numerical simulation curve and the experimental results for pore size distribution matches well. These with numerical fitting, pore size probabilities under different volume fractions are given in Table3.11.

Table 3. 11 Pore size distributed function under different foam content

Foam adding (mass weight)	Pore size Possibility $y(V_f) = \exp(A + B \cdot x)$	A value	B value	Adj.R-Square
$V_f = 0$	$y(0) = \exp(0.69 - 0.00814x)$	0.69	-0.00814	0.85
$V_f = 0.13$	$y(1.3) = \exp(0.65 - 0.00839x)$	0.65	-0.00839	0.90
$V_f = 0.26$	$y(3.3) = \exp(0.40 - 0.00784x)$	0.40	-0.00784	0.98
$V_f = 0.34$	$y(5) = \exp(0.04 - 0.00528x)$	0.04	-0.00528	0.90
$V_f = 0.41$	$y(6.6) = \exp(0.04 - 0.00509x)$	0.04	-0.00509	0.85
$V_f = 0.45$	$y(10) = \exp(0.16 - 0.00569x)$	0.16	-0.00569	0.83
$V_f = 0.56$	$y(13) = \exp(0.20 - 0.00595x)$	0.20	-0.00595	0.82
$V_f = 0.58$	$y(16) = \exp(0.32 - 0.00645x)$	0.32	-0.00645	0.82

Following on Table 3.11, the pore size distribution with different pore volume fractions can be expressed as an exponential function, in which coefficient of A and

B in $y(V_f) = \exp(A + Bx)$ varied under different volume fraction. Therefore, coefficient of A and B in $y(V_f) = \exp(A + B \cdot x)$ is correlated with the pore volume fraction; A is fitted by an exponential function and B is fitted by a cubic function related to volume fraction as follow:

$$A(V_f) = 0.69 - 0.65 \exp\left(-\exp\left(-\frac{V_f - 0.41}{0.14}\right) - \frac{V_f - 0.41}{0.14} + 1\right) \quad (3.13)$$

$$B(V_f) = -0.0081 - 0.016 V_f + 0.11 V_f{}^2 - 0.14 V_f{}^3 \quad (3.14)$$

where V_f is the pore volume fraction.

3.5.2 Pore shape factor

With regard to the experimental data, it is discovered that the pore shape factor is related to pore size, and pore size distribution depended on the volume fraction. Therefore, the pore shape factor is a function of volume fraction and size. In Table3.10 the data illustrated that when 0 and 3.3 mass percent of foam are added, there are more than two items of zero value, and therefore these data can be excluded from the model.

For identical material, the pore shape is determined by the content of added foam and the pore size. Therefore, the development of model for the pore shape factor is based on two steps: in the first step, for each volume fraction, the relationship between pore size and pore shape factor is deduced; secondly combining these equations with the content of added foam, an equation is achieved.

Table 3. 12 Coefficient of shape factor fitted by 5 order polynomial curve

Volume fraction	B0(V_f)	B1(V_f)	B2(V_f)	B3(V_f)	B4(V_f)	B5(V_f)
0.13	1.020	0.00216	7.11E-7	3.15E-9	-3.00E-12	7.32E-16
0.34	0.809	1.29E-4	-4.22E-6	6.31E-9	-3.54E-12	6.87E-16
0.41	0.845	-4.16E-4	-2.07E-6	3.05E-9	-1.54E-12	2.65E-16
0.45	0.872	-6.79E-4	-1.37E-6	2.25E-9	-1.13E-12	1.92E-16

| 0.56 | 0.88 | -8.78E-4 | 2.09E-7 | -2.98E-10 | 4.30E-13 | -1.37E-16 |
| 0.59 | 0.92 | -1.55E-3 | 2.32E-6 | -2.73E-9 | 1.62E-12 | -3.50E-16 |

Note: *B0*, *B1*, *B2*, *B3*, *B4* and *B5* are the coefficient of constant term, first order term, second order term, third order term, fourth order term and fifth order term.

Employing a polynomial fitting function, the coefficients from $B0(V_f)$ to $B5(V_f)$ under the different volume fraction conditions are obtained as follows:

$$B0(V_f) = 1.44 - 0.45 * V_f + 0.11 * V_f{}^2 - 0.01 * V_f{}^3 + 6.64 \times 10^{-4} * V_f{}^4 - 1.3 \times 10^{-5} * V_f{}^5$$

$$B1(V_f) = 0.0024 + 1.15 \times 10^{-4} * V_f - 2.90 \times 10^{-4} * V_f{}^2 + 4.88 \times 10^{-5} * V_f{}^3 - 3.08 \times 10^{-6} * V_f{}^4 + 6.69 \times 10^{-8} * V_f{}^5$$

$$B2(V_f) = 1.89 \times 10^{-5} - 2.06 \times 10^{-5} * V_f + 6.00 \times 10^{-6} * V_f{}^2 - 7.55 \times 10^{-7} * V_f{}^3 + 4.33 \times 10^{-8} * V_f{}^4 - 9.22 \times 10^{-10} * V_f{}^5$$

$$B3(V_f) = -1.94 \times 10^{-8} + 2.63 \times 10^{-8} * V_f - 8.15 \times 10^{-9} * V_f{}^2 + 1.06 \times 10^{-10} * V_f{}^3 - 6.24 \times 10^{-11} * V_f{}^4 + 1.36 \times 10^{-12} * V_f{}^5$$

$$B4(V_f) = 9.27 \times 10^{-12} - 1.45 \times 10^{-11} * V_f + 4.70 \times 10^{-12} * V_f{}^2 - 6.25 \times 10^{-13} * V_f{}^3 + 3.72 \times 10^{-14} * V_f{}^4 - 8.17 \times 10^{-16} * V_f{}^5$$

$$B5(V_f) = -1.68 \times 10^{-15} + 2.89 \times 10^{-15} * V_f - 9.57 \times 10^{-16} * V_f{}^2 + 1.29 \times 10^{-16} * V_f{}^3 - 7.74 \times 10^{-18} * V_f{}^4 + 1.71 \times 10^{-19} * V_f$$

So pore shape factor is depicted as:

$$f_{sp}(V_f, s) = B0(V_f) + B1(V_f)s + B2(V_f)s^2 + B3(V_f)s^3 + B4(V_f)s^4 + B5(V_f)s^5$$

(3.15)

where V_f is the volume fraction of foam concrete, *s* is pore size.

According to Equation 3.15 the shape factor fitting curve of V_f=0.34 foam concrete is drawn in Figure 3.22, and the coefficient of determination is listed in Table 3.13.
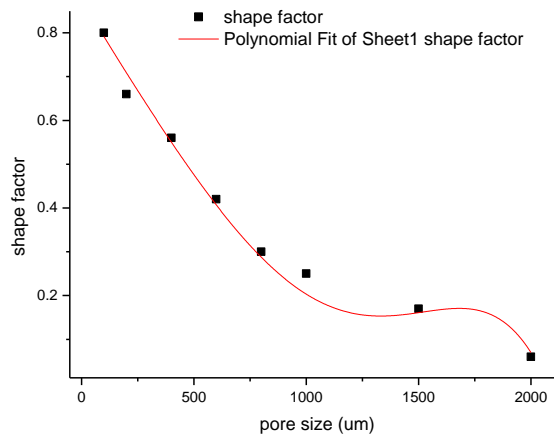
Figure 3. 22 Five order polynomial fitting curve of shape factor for V_f=0.34 foam concrete

Figure 3.22 shows that the five order polynomial fitting curve fits the black squares well, which indicates that the fitting curve matches the pore shape factor well with different pore size and the pore shape factor decreases as the pore size increases. The coefficient of determination is shown in Table 3.13.

Table 3. 13 Coefficient of determination for the regression of curve fitting

	B1	B2	B3	B4	B5	Adj.R-Square
Pore shape factor	0.809	1.29E-04	-4.22E-06	6.31E-09	-3.54E-12	0.9966

3.5.3 Pore area model

It is established that the pore area fraction corresponds to the pore size at different volume fractions, and each size pore area is determined by the pore size and pore shape factor. Therefore, the compressive strength of foam concrete can be fitted by the pore size and area fraction.

With reference to Table 3.10, the averaged pore size, total pore area fraction and compressive strength value can be derived as appeared in Table 3.14.

Table 3. 14 Averaged pore size, total pore area fraction and compressive strength value with different volume fractions of foam concrete

Volume fraction	averaged pore size (um)	Pore area fraction	compressive strength (MPa)
0	115.7	0.0623	48.5
0.13	125.8	0.1703	32.2
0.26	151.8	0.2291	17.4
0.34	189.8	0.3397	12.6
0.41	211.5	0.4958	9.1
0.45	210	0.5384	8.3
0.56	222	0.5797	4.5
0.59	199	0.6613	3.5

Using Table 3.14, the averaged pore size can be fitted by a 4th order equation and related it to volume fraction as follows:

$$\overline{l(V_f)} = 115.81 + 26.97V_f + 16.49V_f^2 + 3010.26V_f^3 - 4565.42V_f^4 \quad (3.16)$$

where $\overline{l(V_f)}$ is the averaged pore size under the volume fraction V_f.

$$\overline{s(V_f)} = 0.07 + 1.27V_f - 7.40V_f^2 + 26.97V_f^3 - 25.98V_f^4 \quad (3.17)$$

where $\overline{s(V_f)}$ is the pore area fraction.

The averaged pore size and pore area fraction are two important parameters for determining the compressive strength of foam concrete, the compressive strength of foam concrete can be expressed as a function of these two variables as follow:

$$f = f(\bar{l}, \bar{s}) \quad (3.18)$$

where $f(\bar{l}, \bar{s})$ is an unknown function, $\bar{l}$ is averaged pore size, and $\bar{s}$ is pore area fraction.

According to Table 3.14 and Equation3.18, compressive strength can be described by an error function, which is given as:

$$f = 3.5 + 11.25 * \left(1 + erf\left(\frac{\bar{l} - 158.45792}{39.04898\sqrt{2}}\right)\right) * \left(1 + erf\left(\frac{\bar{s} - 0.37955}{0.2995\sqrt{2}}\right)\right) \quad (3.19)$$

where f is the compressive strength of foam concrete, and erf is an error function, which can be expressed : $erf(x) = \frac{2}{\sqrt{\pi}}\int_0^x e^{-t^2}dt$.
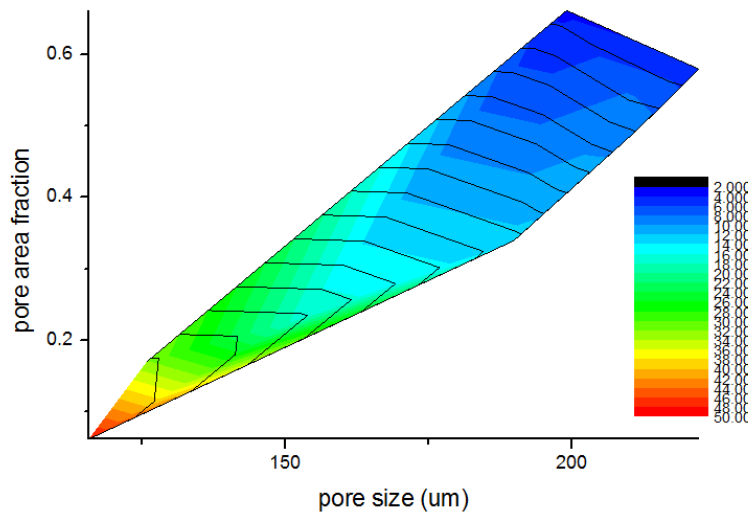
Figure 3. 23 Compressive strength related to pore size and pore area fraction

Figure 3.23, a diagram of the numerical fitting of compressive strength by pore size and pore area fraction, in which different colours stand for different compressive strength values. As pore size increases or pore area fraction increases, compressive strength of foam concrete declines, indicating that reduced pore size and pore area fraction are effective ways to enhance its compressive strength.

Comparing the compressive strength model by volume fraction and pore features, it is found that the model by volume fraction is more closely approached to the experimental result. This phenomenon is explained by cumulative error in the pore feature model where in each step error is gradually accumulated leading to the relative error becoming bigger.

3.6 Summary

In this chapter, EPS concrete is used to study the EPS size and volume effects on compressive strength, and its Young's modulus is deduced according to the compression test, in which the strain gauge is used. In addition, a numerically fitting method is adopted to describe pore features of foam concrete. With a series of experiments, improved experiments and results analysis, it is established that:

1) The compressive strength of EPS concrete containing 2.68mm EPS beads can be expressed as a density function: $f_{2.68} = 5.58 \times 10^{-8} \times \rho^{2.72}$; while the compressive strength of EPS concrete containing 7.04mm EPS beads can be expressed as $f_7 = 3.2 \times 10^{-9} \times \rho^{3.07}$.

2) For the smaller size of EPS beads in EPS concrete, the experimental measurements are more closely approximate the theoretical calculation. Additionally, the lower the volume fraction of EPS beads in EPS concrete is, values tend to converge between the approaches.

3) Through numerically fitting, both the pore volume fraction and compressive strength of foam concrete can be expressed as: $f = 49.00 - 54.10 * (1 - e^{(-V_f/0.31)})$;

4) Pores size distribution in foam concrete is described as: $y(V_f, x) = \exp\left(0.69 - 0.65 \exp\left(-\exp\left(-\frac{V_f - 0.40}{0.14}\right) - \frac{V_f - 0.40}{0.14} + 1\right) + \left(-0.0081 - 0.0165V_f + 0.114V_f{}^2 - 0.139V_f{}^3\right)x\right)$; pore averaged sizes is $\bar{l}(V_f, x) = \frac{1}{5-0} \int_0^5 y(V_f, x) \cdot x dx = \frac{1}{5} \int_0^5 \exp\left(0.69 - 0.65 \exp\left(-\exp\left(-\frac{V_f - 0.40}{0.14}\right) - \frac{V_f - 0.40}{0.14} + 1\right) + \left(-0.0081 - 0.016\varepsilon + 0.11V_f{}^2 - 0.14V_f{}^3\right)x\right) dx$;

5) The Pore shape factor is described as: $f_{sp}(V_f, s) = B0(V_f) + B1(V_f)s + B2(V_f)s^2 + B3(V_f)s^3 + B4(V_f)s^4 + B5(V_f)s^5$, where V_f is the volume fraction of the foam cement, and s is the pore size.

6) Pore area fraction is described as: $\overline{s(V_f)} = 0.065 + 1.267V_f - 7.404V_f{}^2 + 26.967V_f{}^3 - 25.979V_f{}^4$;

7) The compressive strength of foam concrete is expressed as:

$f = 3.5 + 11.25 * \left(1 + erf\left(\frac{\bar{l}-158.45792}{39.04898\sqrt{2}}\right)\right) * \left(1 + erf\left(\frac{\bar{s}-0.37955}{0.2995\sqrt{2}}\right)\right)$, where erf is the error function.

CHAPTER 4 A THEORETICAL METHOD TO DEDUCE THE COMPRESSIVE STRENGTH OF EPS CONCRETE

In this study, a theoretical method is employed to determine the influence of beads size of EPS concrete on the compressive strength of EPS concrete, and then compressive strength of two sizes mixing together model is built to predict the possible maximum compressive strength of EPS concrete.

4.1 Physical Model for Uniformed EPS Beads

To enable the study of EPS bead size and its impact of the ratio of EPS beads size to sample size on the compressive strength of concrete, following assumptions are made:

1) All the EPS beads are spherical shape and that their radii are uniform;
2) The EPS beads are distributed in the concrete body uniformly, which means that the distance between any neighbouring EPS beads is homogeneous;
3) The shape and size of all the EPS beads do not change during the mixing, casting, curing and aging period.
4) EPS beads have no strength, and that the compressive strength of EPS concrete is solely that of the solid concrete matrix.

According to C.M.Song et al[102], the upper limitation of the volume fraction for randomly packing of equal radius spheres in a cubic container is 0.634. When the volume fraction exceeds 0.6, the EPS beads will be in contact with each other. Therefore, the upper limitation for EPS beads volume fraction is set at less than 0.6. In order to simplify the model, the EPS beads in concrete are regarded as regularly ordered as depicted in Figure 4.1, and a cubic shape for specimen with a size of $a \times a \times a$ is adopted; the radius of EPS bead size is r.
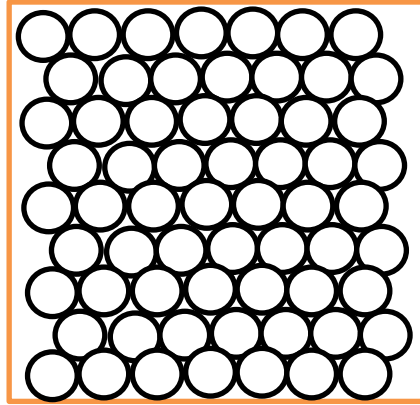
Figure 4. 1 Schematic figure of EPS beads arrangement in concrete body

Representable bead array is illustrated in Figure 4.1 in 2 dimensions, in which the maximum volume fraction of EPS will be where EPS beads are in mutual contact with each other. In order to simplify the model, EPS beads are assumed as rigid ball without any deformation during mixing and casting procedures.

The volume fraction of EPS beads is expressed as:

$$V_f = \frac{\rho_c - \rho_{mix}}{\rho_c - \rho_{eps}}$$ (4.1)

where V_f is the volume fraction of EPS beads in the whole EPS concrete specimen, ρ_c is concrete density without any EPS beads, ρ_{eps} is EPS bead density, ρ_{mix} is EPS concrete density.

To explain the model clearly, the EPS beads distribution is divided into two situations, one is loose packing condition where the EPS volume fraction is relative low and there is no overlapped layer between any two neighbour EPS bead layers; the other is high packing condition that there is overlapped layer between two neighbour EPS beads layers. The overlapped layer means that the distance of two neighbour EPS bead layers is less than 2*r*, and *r* is the EPS beads radius.

4.1.1 Loose packing model of EPS beads

When the volume fraction of EPS beads is very small, the total number of EPS beads can be expressed as:

$$n = \frac{3a^3 V_f}{4\pi r^3}$$ (4.2)

where *n* is the total number of EPS beads, *r* is the radius of EPS bead, *a* is the size of the specimen.

When there is no overlap between two neighbouring layers of beads, the relationship between the EPS bead radius and the specimen size follows Equation4.3.

$$a > n^{\frac{1}{3}}2r \tag{4.3}$$

Put Equation4.3 into Equation4.2, yielding $V_f < \frac{\pi}{6} \approx 0.523$.

The compressive strength of EPS concrete is expressed as:

$$f_c = f_0 \left(1 - n^{\frac{2}{3}}\pi \frac{r^2}{a^2}\right) \tag{4.4}$$

where f_0 is the compressive strength of the concrete without any EPS beads, and f_c is the compressive strength of EPS concrete.

Incorporating Equation 4.2 into Equation 4.4, provides:

$$f_c = f_0 \left(1 - n^{\frac{2}{3}}\pi \frac{r^2}{a^2}\right) = f_0 \left(1 - \left(\frac{9\pi V_f^2}{16}\right)^{\frac{1}{3}}\right) \tag{4.5}$$

In Equation 4.5, the compressive strength of EPS concrete is determined singly by the EPS volume fraction, which means that the compressive strength in the uniformed distribution EPS concrete is only determined by the volume fraction of EPS beads.

4.1.2 High density packing of EPS beads

When there is overlap between the two neighbouring layers of EPS beads, the schematic figure of the EPS beads pile is depicted in Figure 4.2.
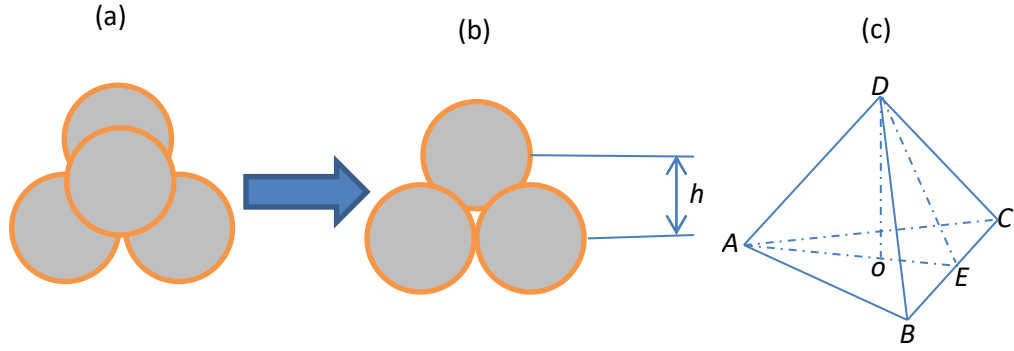
Figure 4. 2 Schematic figure of overlap between neighbouring EPS beads

Figure 4.2 is a schematic figure of the maximum volume fraction for a packing mode for neighbouring layers of EPS bead. Figure 4.2(a) is the top view of EPS beads piled up, in which the bottom layer of EPS beads are arranged in triangle order, and the EPS bead in the upper layer is in contact with the three neighbouring EPS beads. Figure 4.2 (b) is the front view that shows the distance between the two layers' centre h, which is less than $2r$. Figure 4.2 (c) is a schematic figure of neighbouring layers, where are $ABCD$ stands for centre of four EPS beads structure, in which point D is the upper layer, and A,B and C are bottom layers. Because all the EPS beads are in mutual contact with the each other, there is a relationship: $AB = BC = CA = AD = BD = CD = 2r$.

In the overlapping zone, the maximum cross section is located in the middle of DO position, and the distance of h is DO that can be expressed as:

$$h = DO = \sqrt{DE^2 - OE^2} = \sqrt{BD^2 - BE^2 - OE^2} = \sqrt{4r^2 - r^2 - OE^2} \qquad (4.6)$$

$$AE = AO + OE = \sqrt{3}r \qquad (4.7)$$

$$h = \sqrt{AD^2 - AO^2} = \sqrt{4r^2 - AO^2} = \sqrt{DE^2 - OE^2} = \sqrt{3r^2 - OE^2} \qquad (4.8)$$

According to Equation 4.8, AO can be deduced as:

$$AO^2 = r^2 + OE^2 \qquad (4.9)$$

Incorporating Equation 4.6 into Equation 4.9, Equation 4.10 can be derived:

$$AO^2 = r^2 + OE^2 = \left(\sqrt{3}r - OE\right)^2 = 3r^2 - 2\sqrt{3}r \times OE + OE^2 \rightarrow OE = \frac{1}{\sqrt{3}}r \qquad (4.10)$$

Therefore, h can be ascertained:

$$h = \sqrt{3r^2 - OE^2} = \frac{2\sqrt{6}}{3}r \tag{4.11}$$

In the middle of DO, all the radii of circles are the same, and given by:

$$r_1 = \sqrt{r^2 - \left(\frac{h}{2}\right)^2} = \frac{\sqrt{3}r}{3} \tag{4.12}$$

where r_1 is the cross-section radius of EPS beads in the middle of DO.

The maximum area fraction of EPS beads will be: $S = 2n_s\pi r_1^2 = n_s\pi r^2$, where n_s is the total number of EPS beads in each layer, S is the maximum area of EPS beads. In the specimen, there is a relationship: $n_s n_h = n$, where n_h is the total number of layers. And n_h and n_s can be deduced as Equation 4.13 and 4.14 as related in Figure 4.2.

$$n_h = \frac{a-2r}{h} = \frac{a-2r}{r2\sqrt{6}/3} \tag{4.13}$$

$$n_s = \left(\frac{a-2r}{2r}\right) \times \left(\frac{a-2r}{AE}\right) = \frac{(a-2r)^2}{2r\times\sqrt{3}r} = \frac{(a-2r)^2}{2\sqrt{3}r^2} \tag{4.14}$$

The maximum volume fraction of EPS beads in EPS concrete can be deduced as Equation 4.15

$$V_f = \frac{\frac{N_s N_h 4\pi r^3}{3}}{a^3} = \frac{\frac{a-2r}{r2\sqrt{6}}\frac{(a-2r)^2}{2\sqrt{3}r^2}4\pi r^3}{3a^3} = \frac{\pi(a-2r)^3}{3\sqrt{2}a^3} = \frac{\pi}{3\sqrt{2}}\left(1 - \frac{2r}{a}\right)^3 \tag{4.15}$$

From Equation 4.15, the following can be assured: $\frac{2r}{a} \to 0, V_f \to \frac{\pi}{3\sqrt{2}} \cong 0.7405$. The maximum volume fraction of EPS beads is 0.6413, and this value is applicable only when all EPS beads are packed in an orderly array with all the neighbouring EPS beads in contact with each other. Therefore, the maximum area fraction of EPS beads can be expressed as:

$$S_e = \frac{N_s\pi r^2}{a^2} = \frac{\frac{(a-2r)^2}{2\sqrt{3}r^2}\pi r^2}{a^2} = \frac{\pi}{2\sqrt{3}}\left(1 - \frac{2r}{a}\right)^2 \tag{4.16}$$

where S_e is the maximum area fraction of EPS beads in EPS concrete specimen.

When $\frac{2r}{a} \to 0$ and $V_f \to \frac{\pi}{3\sqrt{2}} \cong 0.7405$, $S_e \to \frac{\pi}{2\sqrt{3}} \cong 0.9069$, which means that the maximum EPS beads surface fraction in EPS concrete is 0.9069. Meanwhile the compressive strength of EPS concrete is expressed as Equation 4.17.

$$f_{c-min} = f_0(1 - S_e) \cong 0.0931 f_0 \qquad (4.17)$$

where f_{c-min} is the minimum compressive strength of EPS concrete where the volume fraction of EPS beads reaches the maximum value 0.9069, and its compressive strength is nearly 1/10 of the dense concrete. This implies that for equal radius EPS beads that cast EPS concrete, the lowest compressive strength will be greater than 0.0931 times that of dense concrete. Here f_0 is set as 40 MPa. According to Equation 4.17, the relationship between compressive strength and the ratio of EPS beads radius to specimen size can be drawn as Figure 4.3.
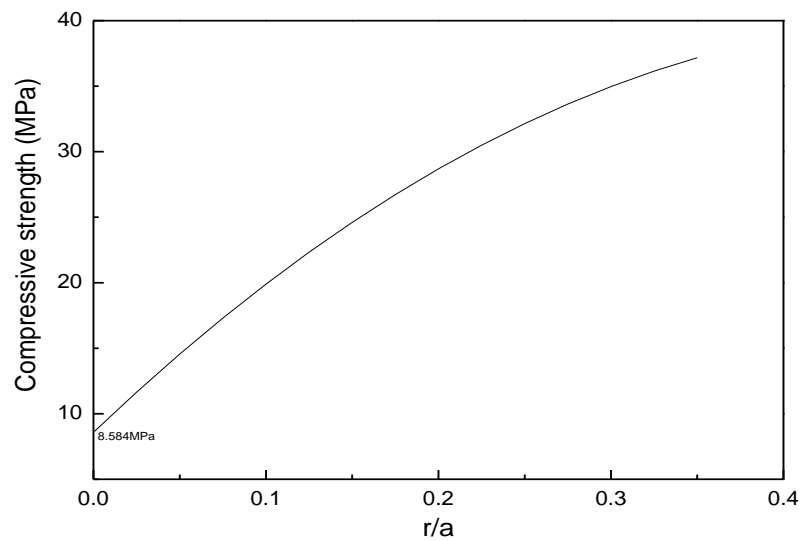
Figure 4. 3 Relationship between the ratio of EPS bead to specimen and compressive strength under the maximum volume fraction

From Figure 4.3 it can be seen that the minimum compressive strength will be higher than 8.58MPa. As ratio *r/a* increases, the compressive strength increases too. Actually, when *r/a*>0.317, there is only one EPS bead in any cross section of the cubic specimen that is not satisfied with a maximum volume fraction of 0.7405.

However, when the *r/a* approaches to 0.5, there is only one EPS bead in the cubic specimen. At that time, the volume fraction of EPS is given by Equation 4.18:

$$V_f = \frac{\frac{4\pi r^3}{3}}{a^3} \cong \frac{4\pi}{(3*8)} = \frac{\pi}{6} \cong 0.52 \tag{4.18}$$

and its maximum area fraction of EPS beads is determined as:

$$S_e = \frac{\pi r^2}{a^2} = \frac{\pi}{4} \cong 0.7854 \tag{4.19}$$

Applying Equation 4.4 and Equation 4.19, the compressive strength is 8.58 MPa.

4.1.3 Different situation of packing EPS beads

In order to investigate the effect of *r/a* on compressive strength, *r/a* can be divided into the following situations.

Condition 1 $2r < a < (2 + 2/\sqrt{3})r$, $(\frac{1}{2+2/\sqrt{3}} < \frac{r}{a} < \frac{1}{2})$, there is only one EPS bead in the cubic sample, and the volume fraction can be expressed as:

$$V_f = \frac{4\pi r^3}{3a^3} \rightarrow V_f \in (0.1334, 0.524) \rightarrow \frac{r}{a} = \left(\frac{3\varepsilon}{4\pi}\right)^{\frac{1}{3}}$$

$$\tag{4.20}$$

The maximum area fraction of a single EPS bead in EPS concrete will be:

$$S_e = \frac{\pi r^2}{a^2} = \pi \left(\frac{3V_f}{4\pi}\right)^{\frac{2}{3}} \tag{4.21}$$

For only one EPS bead, the maximum volume fraction is $V_f = \frac{4\pi r^3}{3a^3} = \frac{\pi}{6} \approx 0.52$.

If follows that with a single EPS bead occupying the maximum volume fraction, the maximum area fraction can be deduced as: $S_e = \frac{\pi r^2}{a^2} = \frac{\pi}{4} \approx 0.79$ where $r = a/2$, and the compressive strength is given as Equation 4.22.

$$f_c = f_0(1 - S_e) = 0.21f_0 \tag{4.22}$$

When there is only one EPS bead in the concrete specimen and the radius of EPS bead gradually increases from very tiny value to half of the specimen size, the compressive strength will be expressed as:

$$f_c = f_0(1 - S_e) = f_0\left(1 - \pi\frac{r^2}{a^2}\right) \tag{4.23}$$

According to Equation 4.23, the relationship between compressive strength and the volume fraction for a specimen with a single 1 EPS bead in EPS concrete can be plotted as Figure 4.4.
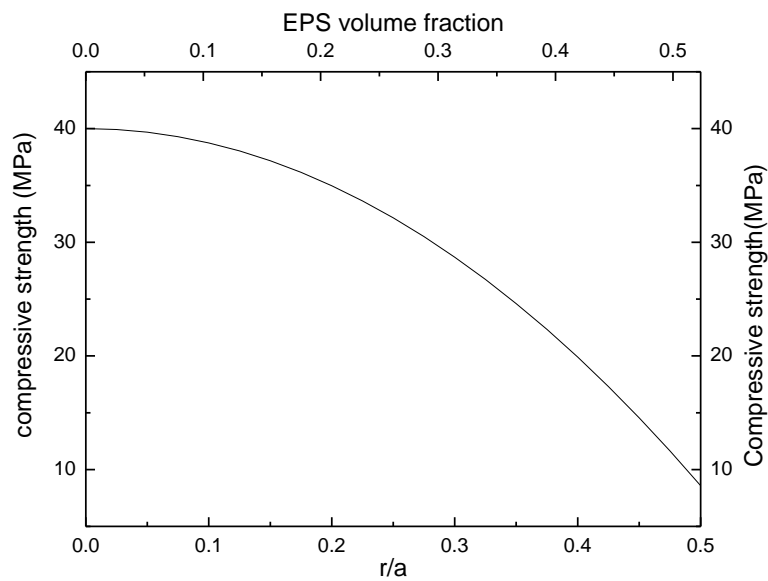
Figure 4. 4 Relationship between ratio of EPS bead to specimen and compressive strength for a single EPS bead in concrete body

In Figure 4.4 where there is only a single EPS bead in the specimen, and when *r/a*=0, the volume fraction of EPS is zero and EPS concrete has the maximum compressive strength, which is 40 MPa. When *r/a* increases, the volume fraction of EPS beads also increases and the compressive strength decreases gradually. As *r/a* reaches 0.5, the compressive strength drops down to 8MPa.

Condition 2 The situation of two EPS beads
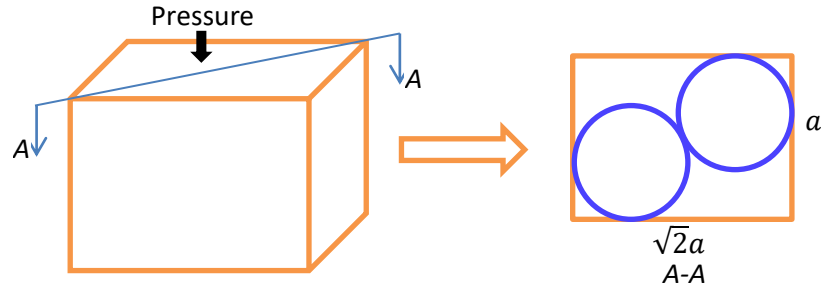
Figure 4. 5 Schematic figure of packing mode of two EPS beads in a cubic specimen

EPS concrete under a pressure condition, the cross *A-A* section along the diagonal of the top surface exists two EPS beads when $\left(2 + \frac{2}{\sqrt{3}}\right)r \leq a < \left(2 + \sqrt{2}\right)r$, ($\frac{1}{2+\sqrt{2}} < \frac{r}{a} < \frac{1}{2+2/\sqrt{3}}$) applied. The cubic specimen size is $a \times a \times a$, and the radius of EPS bead is *r*. The volume fraction of EPS beads is $V_f = \frac{n \times 4\pi r^3}{3a^3}$ $(n \leq 2)$, and the total number of EPS beads is $n = \frac{3V_f a^3}{4\pi r^3}$. In this situation, EPS beads volume fraction has a volume between $V_f \in (0.11 - 0.13)$.

The maximum area fraction of EPS beads can be deduced as $S_e = \frac{\pi r^2}{a^2} \in (0.27 - 0.32)$, which means that the maximum cross section area must be the section across through one of the two beads centre, and the maximum EPS area fraction will be in the range of $V_f \in (0.27 - 0.32)$. Therefore, the compressive strength of EPS concrete is the same as Equation 4.23.

As Figure 4.5 indicates that even for the cube when there is more than one EPS bead present, there is overlap, but the maximum area fraction of EPS is only determined by one EPS bead.

When the two kinds of *r/a* EPS concrete have the same volume fraction, one *r/a* is as stated in condition 1, and the other *r/a* is as stated in condition 2 where there are two EPS beads in EPS concrete.

$$V_{f_1} = \frac{4\pi}{3}\left(\frac{r_1}{a}\right)^3 = V_{f_2} = 2\frac{4\pi}{3}\left(\frac{r_2}{a}\right)^3 \tag{4.24}$$

where r_1 and r_2 are the radius of EPS bead in condition 1) and condition 2), respectively, V_{f_1} and V_{f_2} are the volume fraction of EPS bead in condition 1) and condition 2) respectively.

And then Equation 4. 24 applies:

$$\frac{r_1}{a} = 2^{\frac{1}{3}}\frac{r_2}{a} \tag{4.25}$$

So the maximum EPS area fraction of situation 1) is:

$$S_{e1} = \pi\left(\frac{r_1}{a}\right)^2 = \pi\left(\frac{2^{\frac{1}{3}}r_2}{a}\right)^2 = 2^{\frac{2}{3}}S_{e2} \tag{4.26}$$

From Equation 4.26, it can be established that if the volume fraction is the same, the maximum EPS area fraction of condition 1) is $2^{\frac{2}{3}}$ times of condition 2), which means that one EPS bead has a higher area fraction than the EPS area fraction of two EPS beads embedded in concrete.

Condition 3 when $(2 + \sqrt{2})r \le a$, $\frac{r}{a} \le \frac{1}{2+\sqrt{2}}$, the volume fraction of EPS is $V_f = \frac{n\times 4\pi r^3}{3a^3}$, and the total number of EPS beads are $n = \frac{3V_f a^3}{4\pi r^3}$ (n<8).

Similarly to condition 2), the maximum area fraction of EPS beads must be the cross section containing integer number of EPS beads, and the maximum area face must be the theoretical face through these EPS beads centre. In such a cross-section, the maximum number of EPS beads is deduced from Equation 4.27.

$$n_{cs} = fix(n^{\frac{2}{3}}) \tag{4.27}$$

where n_{cs} is the maximum EPS bead number, fix is a round function, which transforms $n^{\frac{2}{3}}$ into an integer and towards to the zero direction because in real samples, there are no divided EPS beads.

According to Equation 4.27, the maximum EPS beads area fraction is expressed as Equation 4.28.

$$S_e = n_{cs}\pi r^2/a^2 \tag{4.28}$$

The compressive strength is deduced as:

$$f_c = f_0(1 - S_e) = f_0(1 - \frac{fix\left(\frac{3V_f a^3}{4\pi r^3}\right)^{\frac{2}{3}} \pi r^2}{a^2})$$ (4.29)

When the volume fraction is set as a constant, the effect of EPS bead size can be rewritten as a function of the ratio of EPS beads to specimen. For this study, two different sizes of EPS beads are adopted, which are $\alpha_1 = \frac{r_1}{a}$ and $\alpha_2 = \frac{r_2}{a}$, respectively, and then the compressive strength is provided by Equation 4. 30:

$$\begin{cases} f_{c1} = f_0(1 - S_{e1}) = f_0\left(1 - \frac{fix\left(\frac{3V_f a^3}{4\pi r_1^3}\right)^{\frac{2}{3}} \pi r_1^2}{a^2}\right) = f_0\left(1 - fix\left(\frac{3V_f}{4\pi \alpha_1^3}\right)^{\frac{2}{3}} \pi \alpha_1^2\right) \\ \\ f_{c2} = f_0(1 - S_{e2}) = f_0\left(1 - \frac{fix\left(\frac{3V_f a^3}{4\pi r_2^3}\right)^{\frac{2}{3}} \pi r_2^2}{a^2}\right) = f_0\left(1 - fix\left(\frac{3V_f}{4\pi \alpha_2^3}\right)^{\frac{2}{3}} \pi \alpha_2^2\right) \end{cases}$$

(4.30)

Where S_{e1} and S_{e2} are the maximum area fractions of EPS beads corresponding to α_1 and α_2.

4.1.3 Results and discussion

When the volume fraction of EPS beads is determined, the total number of EPS beads can got as a function of *r/a* according to Equation 4.24. Using Equation 4.27 the total number of EPS beads in the cross section can be obtained, then the EPS beads area fraction can be predicted by Equation 4.28. When the ESP beads area fraction is determined, the compressive strength can be got according to Equation 4.29. Equation 4.24 and 4.29 are function of *r/a*. Based on Eq.4.24, 4.27 and Eq.4.29, the relationship between *r/a* and the possible maximum compressive strength can be plotted.

Here the volume fraction of EPS bead is adopted as 5%, 20% and 40% to find the role of *r/a* on compressive strength, in which 5% volume fraction represents the

loose EPS bead distribution; 20% a middle level of EPS distribution, and 40% the upper level of EPS density distribution. The maximum r/a value can be deduced by using Equation 4.30.

$$V_f = \begin{cases} 5\% & \dfrac{r}{a} \leq \left(\dfrac{3 * 5\%}{4\pi}\right)^{\frac{1}{3}} = 0.2285 \\[2ex] 20\% & \dfrac{r}{a} \leq \left(\dfrac{3 * 20\%}{4\pi}\right)^{\frac{1}{3}} = 0.3629 \\[2ex] 40\% & \dfrac{r}{a} \leq \left(\dfrac{40\%}{4\pi}\right)^{\frac{1}{3}} = 0.4571 \end{cases}$$

For $\varepsilon = 5\%$, the ratio of EPS beads to specimen should be $\dfrac{r}{a} \leq 0.2285$. The relationship between r/a and compressive strength can be calculated as Figure 4.6 according to Equation 4.30.

The relationship between the r/a and compressive strength with the EPS volume fraction of 5% is plotted in Figure 4.6, where the number *1,2,3,4* and *5* represent the total number of EPS beads in one of direction of the maximum cross-section of the specimen.
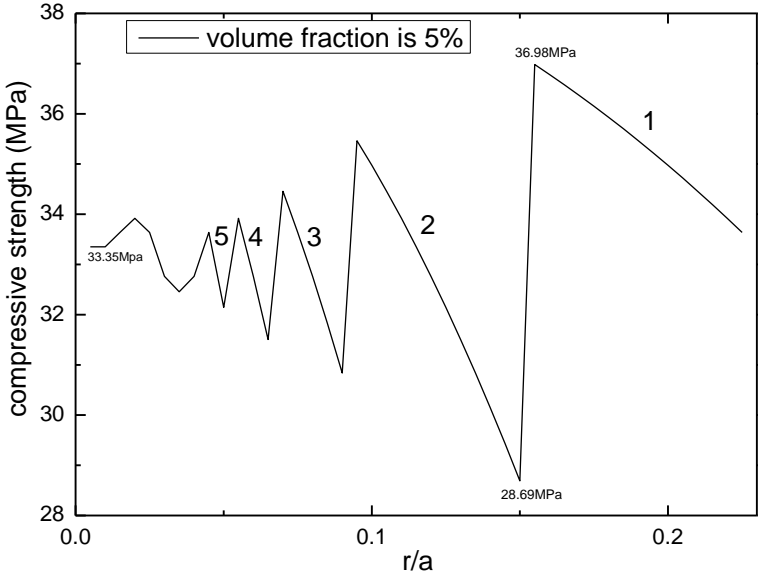
Figure 4. 6 Relationship between r/a and compressive strength when V_f=5%

The compressive strength value oscillates from the initial value of 33.35MPa when the *r/a* approaches to zero, which means that the radius is very tiny compared with specimen size and there are large number of EPS beads in each direction in the cross-section of the specimen. When the *r/a* is less than 0.05, the specimen size is 10 times of the EPS bead diameter, and in each direction of the maximum cross-section there are more than 5 EPS beads as shown in the left side of figure as marked 5, in which the amplitude of compressive strength from the averaged compressive strength is less than 1MPa. When the number of EPS beads in each direction of the specimen is less than 5, the amplitude of compressive strength varies greatly. From Figure 4.6, it can also be found that the maximum and the minimum compressive strength are 36.98MPa and 28.69MPa respectively, and the difference between the maximum and the minimum compressive strength reaches 8.19MPa, nearly 25% of the maximum compressive strength.

Neglecting the compressive strength of EPS beads, the compressive strength can be deduced theoretically by the method presented in Equation 4.29. A comparison the theoretical compressive strength with the experimental values of EPS concrete with Ø2.68mm EPS beads is provided in Figure 4.7.
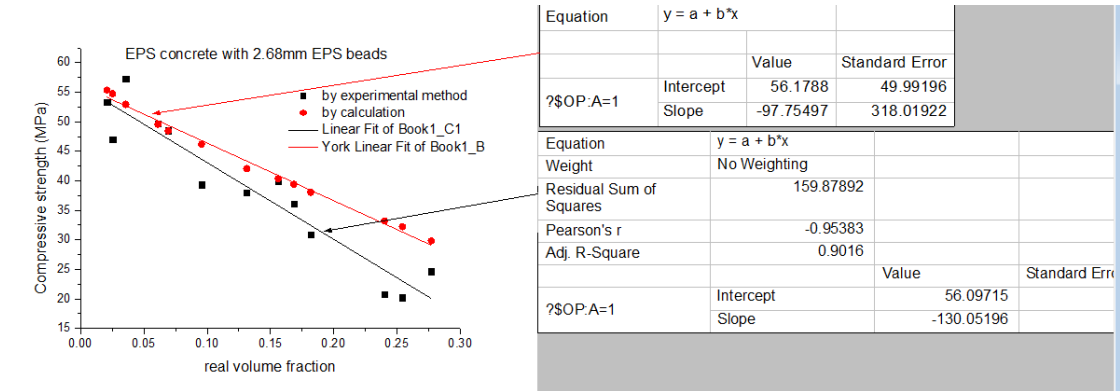
Figure 4. 7 A comparison between theoretically calculated and experimentally determined compressive strength values

In Figure 4.7, the comparison between theoretically calculated values and experimentally determined compressive strength of EPS concrete with diameter of Ø2.68mm EPS beads is provided. The theoretically calculated compressive strength

is higher than the experimentally determined value. However, some experimental values are very close to theoretically calculated values. The difference between theoretically calculated value and experimentally determined value is less than 15MPa. The difference is attributable to: 1) theoretical calculated values are based on the idealized EPS distribution model; 2) experimental condition may have generated handling and preparation error which have led to inaccuracies. Convergence but both methods are achieved by numerical means:

$$f_{cs}^2 = A + f_{ce}^2 => A = f_{cs}^2 - f_{ce}^2 = 56.1788 - 97.75497 \times V_f - \left(56.09715 - 130.05196 \times V_f\right) = 0.082 + 32.30 \times V_f \qquad (4.31)$$

where f_{cs}^2 is the compressive strength of Ø2.68 mm EPS beads by Equation 4.30, f_{ce}^2 is the compressive strength by the experimental method; A is the difference between predicting and experimental results. Therefore, the real compressive strength at any EPS volume fraction can be expressed as the theoretically calculated value subtracting the difference: $f_{ce}^2 = f_{cs}^2 - A$.

Table 4. 1 A comparison of compressive strength value for EPS concrete by the theoretical method and experimentally determined for Ø7.04 mm

Real volume fraction	Compressive strength by calculation (MPa)	Compressive strength by experimental method (MPa)
0.17	39.76	32.15
0.25	32.82	26.23
0.18	38.62	26.28
0.32	28.46	11.19
0.35	26.03	14.68
0.30	29.64	18.84
0.32	28.60	21.00
0.34	26.53	11.22
0.53	14.26	4.68

Equation	y = a + b*x		
Weight	No Weighting		
Residual Sum of Squares	110.6917	6.16228	
Pearson's r	-0.93564	-0.99599	
Adj. R-Square	0.86157	0.9911	
		Value	Standard Error
Compressive strength	Intercept	41.06276	2.76212
	Slope	-73.87873	9.29023
	Intercept	52.00656	0.65171
	Slope	-73.16429	2.192
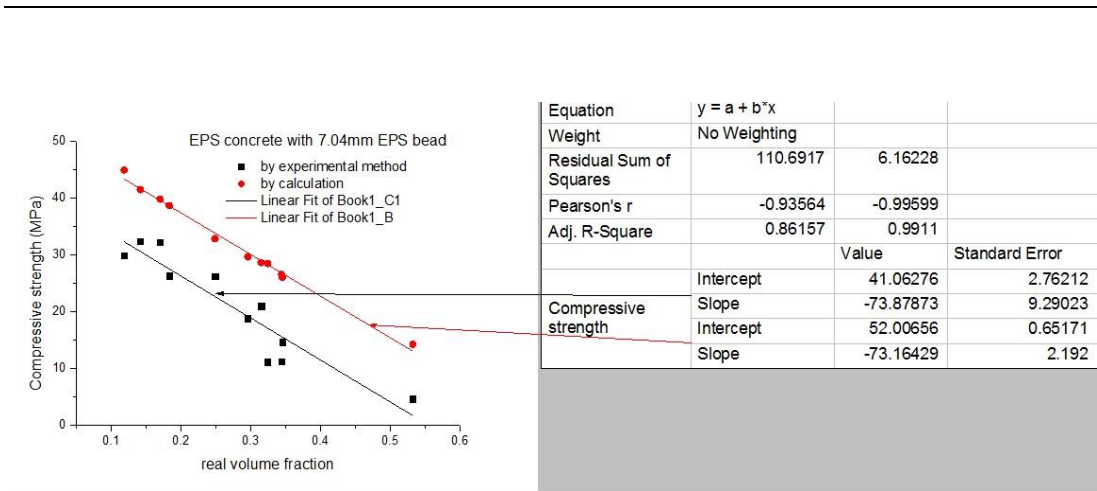
Figure 4. 8 Stress-strain relationship of EPS concrete with Ø 7.04mm EPS beads

The comparison of theoretically calculated and experimentally determined compressive strength of EPS concrete with diameter of Ø7.04 mm EPS beads is given in Figure 4.8. The theoretically calculated compressive strength is significantly higher than these measured experimentally. The maximum difference between theoretically calculated value and experimental measured value may be as much as 20MPa.

$$f_{cs}^7 = A + f_{ce}^7 => A = f_{cs}^7 - f_{ce}^7 = 52.01 - 73.16 \times V_f - (41.06 - 73.88 \times V_f) = 10.94 + 0.71 \times V_f$$

(4.32)

where f_{cs}^7 is the compressive strength of Ø2.68 mm EPS beads by the theoretical method, f_{ce}^7 is the compressive strength by experimental method; A is the difference between theoretical and experimental results. Therefore, the real compressive strength at any EPS volume fraction can be described as the theoretically calculated value subtracting the difference $f_{ce}^7 = f_{cs}^7 - A$. Knowledge of this relationship is helpful designing the EPS volume fraction.

The relationship between EPS volume fraction and Young's modulus is depicted in Figure 4.9, and a) for d=2.68 mm EPS beads and b) for d=7.04 mm EPS beads.
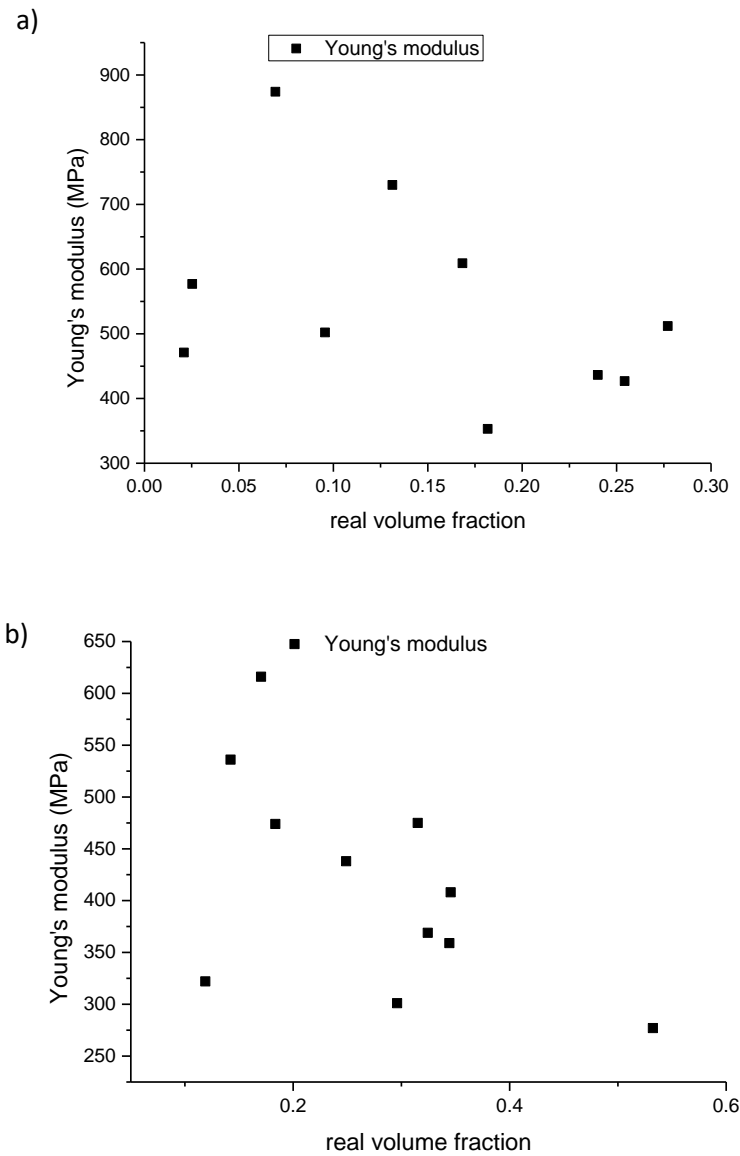
Figure 4. 9 Relationship between the EPS volume fraction and Young's modulus, a) *d*=2.68mm EPS beads, b) *d*=7.04mm EPS beads

Young's modulus totally decreases from 874MPa as EPS volume fraction increases. In Figure 4.9 b), the Young's modulus displays the similar trend that its value dropped from 648MPa as EPS volume fraction increases. Comparing Figure 4.9 a) and b), it can be deduced that the specimen containing Ø2.68 mm EPS beads has a higher Young's modulus than that containing 7.04 mm EPS beads. In addition, since the EPS beads are distributed unevenly in concrete, compressive strength and Young's modulus might vary even when the volume fraction is the same. There is a

big dispersion in compressive strength and Young's modulus values under experimental conditions due to unspecified variable.
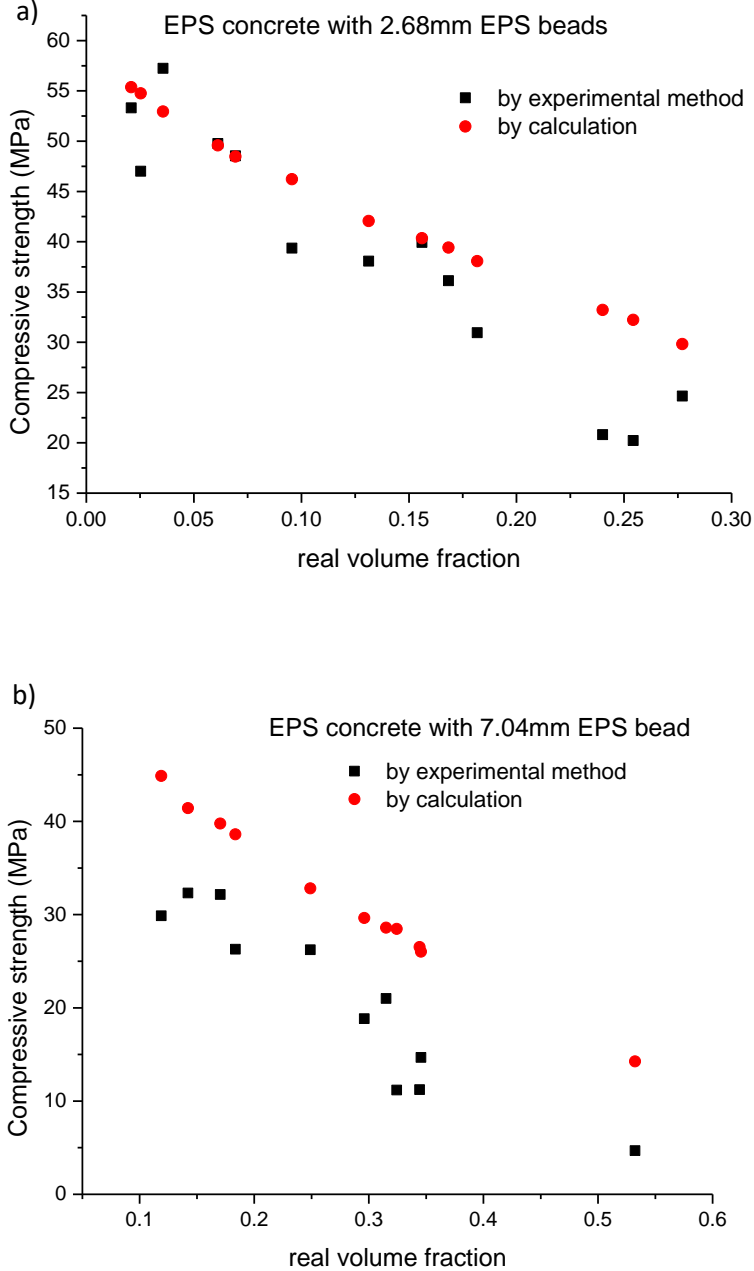
Figure 4. 10 Comparison of compressive strength values derived from the theoretical calculations and the experimental method

Compressive strength of both Ø2.68 mm and Ø7.04 mm EPS beads by the theoretical and experimental methods is presented in Figure 4.10. Circles represent the compressive strength calculated theoretically, while the squares are measured experimentally. Compressive strength decreases as EPS volume fraction increased in both theoretical and experimental methods (Figure 4.10 a), and experimentally compressive strength is generally lower than that by theoretical calculation. Compared both figures, the compressive strength of EPS concrete containing Ø 7.04 mm EPS beads has a lower compressive strength than that containing Ø 2.68 mm EPS beads. Furthermore, the difference between the theoretical and experimental approaches is smaller for the 2.68 mm EPS beads than that containing the 7.04 mm EPS beads. This may be experimented by the finer EPS beads having a more regular and uniform distribution in concrete than the coarser EPS beads.

Because EPS beads distribution is not uniform vertically in the tested sample, this meant that the EPS area fraction is not the same, and the maximum possible compressive strength of EPS concrete is limited by the maximum EPS beads area fraction. In the assumed model, EPS beads are distributed uniformly within EPS concrete sample. If EPS beads are distributed unevenly, there are some positions where the EPS beads area fraction is higher than the averaged area fraction. Therefore, the experimental compressive strength of EPS concrete is lower than the theoretical calculated value for these zones with large area fraction. For the lower volume fraction of EPS beads in EPS concrete, EPS beads distribution is closer to the idealized distribution than that higher volume fraction of EPS beads in EPS concrete. This minimizes compressive strength difference between the experimentally measured and theoretically calculated values can be obtained.

4.2 Mathematical Model for Two Sizes EPS Mixed Model

The compressive strength model for mono-size EPS beads is easy to build, and the upper limited volume fraction for closely packing EPS beads is 0.74 ($\frac{\pi}{\sqrt{18}}$) correspond to a tetrahedral structure. When there are two sizes of EPS beads, EPS volume fraction can reach: $0.93(1 - \left(1 - \frac{\pi}{\sqrt{18}}\right)^2)$ [103]. Therefore, adopting two or more size EPS beads mixed together can reduce its density greatly, providing a way

to manufacture lower density EPS concrete. However, as EPS volume fraction increases, the role of maximum area fraction plays in influencing its final compressive strength requires precise investigation. This is especially true for how the area fraction can be controlled by adjusting ratio of the volume fraction so that the compressive strength/density can be optimized.

With real construction, there is a great demand for light weight EPS concrete with high compressive strength. If relationship between the compressive strength and the ratio/volume fraction is known in two size EPS bead mixed model, the product will be more competitive.

4.2.1 Physical model for two-size-EPS beads mixed EPS concrete

In order to build a two-size-EPS bead mixed model, it is also assumed that the compressive strength only relies on the maximum area fraction of EPS beads in EPS concrete, and that all the EPS beads are distributed uniformly. The cubic sample size is $a \times a \times a$, and radius of EPS are r_1 and r_2 corresponding to the volume fraction v_1 and v_2, then the following equation applies.

$$f = f_0(1 - S) \tag{4.33}$$

where S is the area fraction of EPS beads (which includes two parts contributed by r_1 and r_2 EPS beads).

$$S = S_1 + S_2 \tag{4.34}$$

where S_1 is the area fraction of r_1 EPS bead, and S_2 is the area fraction of r_2 EPS beads.

The volume fraction is $V_f = v_1 + v_2$, where ε is the total volume fraction of EPS bead, v_1 is the volume fraction of r_1 EPS beads, and v_2 is the volume fraction of r_2 EPS beads.

$$v_1 = \frac{N_1 4\pi r_1^3}{3a^3} \rightarrow \frac{N_1 r_1^3}{a^3} = \frac{3v_1}{4\pi} \tag{4.35}$$

$$v_2 = \frac{N_2 4\pi r_2^3}{3a^3} \rightarrow \frac{N_2 r_2^3}{a^3} = \frac{3v_2}{4\pi} \qquad (4.36)$$

$$V_f = v_1 + v_2 = \frac{N_1 4\pi r_1^3}{3a^3} + \frac{N_2 4\pi r_2^3}{3a^3} \qquad (4.37)$$

where N_1 and N_2 are total number of EPS beads corresponding to r_1 and r_2 EPS beads.

If the total volume fraction of EPS beads is constant, $V_f = constant$, the maximum compressive strength can be calculated only after the minimum area fraction of EPS beads.

$$V_f = v_1 + v_2 = \frac{N_1 4\pi r_1^3}{3a^3} + \frac{N_2 4\pi r_2^3}{3a^3} = constant \qquad (4.38)$$

Rewriting Equation 4.38 yields Equation 4.39:

$$v_2 = V_f - v_1 = \varepsilon - \frac{N_1 4\pi r_1^3}{3a^3} = \frac{N_2 4\pi r_2^3}{3a^3} \qquad (4.39)$$

Equation 4.39 can be rewritten as:

$$\frac{N_2 r_2^3}{a^3} = \frac{3V_f}{4\pi} - \frac{N_1 r_1^3}{a^3} \qquad (4.40)$$

That is:

$$\frac{N_2^{\frac{1}{3}} r_2}{a} = \left(\frac{3V_f}{4\pi} - \frac{N_1 r_1^3}{a^3}\right)^{\frac{1}{3}} \qquad (4.41)$$

If the minimum EPS area fraction is determined by the ratio of r_1 and r_2 EPS beads, the maximum compressive strength of EPS can be calculated. Therefore, when the total volume fraction of EPS beads is determined, the ratio of two sizes EPS volume fraction plays the mainly decisive role in affecting the compressive strength. The total EPS area fraction is given as Equation 4. 42.

$$S = S_1 + S_2 = \pi \left(\frac{N_1^{\frac{2}{3}} r_1^2}{a^2} + \left(\frac{3V_f}{4\pi} - \frac{N_1 r_1^3}{a^3}\right)^{\frac{2}{3}} \right) = \pi \left(\left(\frac{3v_1}{4\pi}\right)^{\frac{2}{3}} + \left(\frac{3V_f}{4\pi} - \frac{3v_1}{4\pi}\right)^{\frac{2}{3}} \right) \qquad (4.42)$$

The minimum EPS area fraction can be obtained only when the partial derivative for v_1 is equal to zero, which is given as Equation 4.43.

$$\frac{\partial S}{\partial v_1} = \pi \left(\frac{1}{2\pi} \left(\frac{3v_1}{4\pi} \right)^{-\frac{1}{3}} - \frac{1}{2\pi} \left(\frac{3V_f}{4\pi} - \frac{3v_1}{4\pi} \right)^{-\frac{1}{3}} \right) = 0 \tag{4.43}$$

Equation 4.43 can be simplified as Equation 4.44:

$$\left(\frac{3v_1}{4\pi} \right)^{-\frac{1}{3}} = \left(\frac{3V_f}{4\pi} - \frac{3v_1}{4\pi} \right)^{-\frac{1}{3}} \tag{4.44}$$

From Equation 4.44, Equation 4.45 can be deduced directly.

$$v_1 = \frac{1}{2}V_f, \text{ and } v_2 = \frac{1}{2}V_f \tag{4.45}$$

According to Equation 4.45, it is evident that the minimum area fraction can be obtained only when $v_1 = v_2 = \frac{1}{2}V_f$, and the minimum area fraction is expressed as:

$$S = S_1 + S_2 = \pi \left(\left(\frac{3v_1}{4\pi} \right)^{\frac{2}{3}} + \left(\frac{3V_f}{4\pi} - \frac{3v_1}{4\pi} \right)^{\frac{2}{3}} \right) = 2\pi \left(\frac{3V_f}{8\pi} \right)^{\frac{2}{3}} \tag{4.46}$$

The maximum compressive strength of mixed EPS beads is:

$$f = f_0(1 - S) = f_0 \left(1 - 2\pi \left(\frac{3V_f}{8\pi} \right)^{\frac{2}{3}} \right) \tag{4.47}$$

According to Equation 4.47, the highest possibility of maximum compressive strength can be achieved only when the two size EPS beads have the same volume fraction.

4.2.2 Compressive strength by two sizes EPS beads model

Employing Equation 4.41 with only one single sized EPS bead, compressive strength can be expressed as: $f_c = f_0(1 - S_e) = f_0(1 - \frac{fix\left(\frac{3V_f a^3}{4\pi r^3} \right)^{\frac{2}{3}} \pi r^2}{a^2})$. If the $r/a \ll 0.05$, the size effect can be neglected, and the compressive strength can be expressed as $f_c = f_0(1 - S_e) = f_0 \left(1 - \pi \left(\frac{3V_f}{4\pi} \right)^{\frac{2}{3}} \right)$. Holding the volume fraction to the same, adoption of two sizes of EPS bead causes its compressive strength to decrease a little. The compressive strength of ESP concrete comparison between only one kind of EPS beads and two kinds of EPS is depicted in Figure 4.11.
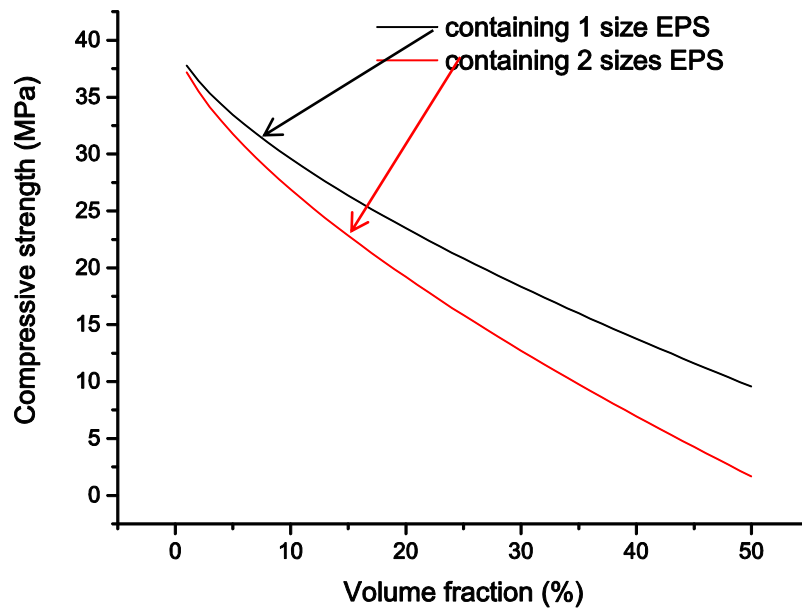
Figure 4. 11 Compressive strength comparisons between EPS concrete containing one size EPS and two sizes EPS beads

As the volume fraction of EPS beads increases, the compressive strength drops gradually, but the EPS concrete containing two kinds of EPS beads declines more quickly than that containing only one size EPS beads under the same volume fraction condition. Moreover, if the EPS concrete contains a certain volume fraction of both EPS beads, as the volume fraction of EPS beads increases, the difference between that the single EPS bead size to that with both increases. Therefore, for a given volume fraction, higher compressive strength can be achieved by using uniformed size of EPS beads rather than by employing two sizes of EPS beads.

4.3 Summary

By evaluating the suitability of one size and two sizes mixed together in models, the following conclusions can be described:

1) If there is only one size of EPS beads in the concrete matrix, the ratio of r/a plays an important role in determining the volume fraction and the compressive

strength. When *r/a*<<0.05, the compressive strength can be regarded as a function of EPS volume fraction only.

2) For EPS concrete contained single sizes of EPS beads, the compressive strength can be expressed as: $f_c = f_0(1 - S_e) = f_0(1 - \frac{fix\left(\frac{3V_f a^3}{4\pi r^3}\right)\pi r^2}{a^2})$, where f_0 is the initial compressive strength without EPS beads, fix is a round function, V_f is EPS volume fraction;

3) If EPS concrete contains two sizes EPS beads, the maximum compressive strength can be obtained only when the volume fraction ratio is 50:50, and at that time the compressive strength of EPS concrete is: $f = f_0(1 - S) = f_0\left(1 - 2\pi\left(\frac{3V_f}{8\pi}\right)^{\frac{2}{3}}\right)$.

4) If the EPS concrete contains two sizes of EPS beads, its compressive strength is inherently lower than that containing single size EPS beads with the same volume fraction.

CHAPTER 5 SIMULATION OF EPS BEADS DISTRIBUTION IN EPS CONCRETE

With traditional concrete, the shape and distribution of aggregates directly affect the final compressive strength and its failure mode [104-107]. However, there is less research work focused on EPS beads distribution and its impact on the compressive strength. In 2004 K.Miled et al studied the compressive strength and failure mode assuming an idealized EPS beads distribution [78]. However, EPS beads are distributed randomly in a real EPS concrete specimen meaning that the inter-bead distance between neighbouring EPS beads is not uniform. Therefore, further study the EPS distribution will advance understanding of the failure mode of EPS concrete.

5.1 A 2D EPS Beads Distribution Model

Knowledge of the distribution of EPS beads is crucial for predicting the compressive strength of EPS concrete. The EPS beads occupy a greater area fraction, and the solid concrete matrix occupies less area fraction decreasing compressive strength. However, the distribution of EPS beads is influenced by many factors, including concrete mixing time, the mixing processes, ratio of cement to water etc. Although it is difficult to predict the EPS beads distribution, a probability model can provide a plausible approximated description for the random distribution of EPS beads in EPS concrete.

EPS beads are essentially distributed randomly throughout concrete matrix, and each idealised cross-section will be different. However, the averaged area fraction of the EPS beads is related to its volume fraction. Therefore, there is an approximated relationship between EPS beads volume fraction and averaged area fraction.

In a 2D model, the volume fraction can be transformed into an area fraction firstly, and this can be expressed as:

$$V_f = \sum \frac{4\pi r_i^3}{3a^3} \tag{5.1}$$

where V_f is EPS beads volume fraction in EPS concrete, r_i is radius of the ith EPS bead, and a is size of a theoretical cubic sample. If the radius of each EPS bead is the same, Equation 5.1 can be rewritten as:

$$V_f = n \times \frac{4\pi r_i^3}{3a^3} \tag{5.2}$$

where n is the total number of EPS beads in the EPS concrete. The area fraction of EPS beads in any cross-section is expressed as:

$$S = \sum \frac{\pi r_i^2}{a^2} \tag{5.3}$$

where S is EPS area fraction in an idealised cross-section of EPS concrete. Employing Equation 5.2, the ratio of $\frac{r}{a}$ can be deduced directly by:

$$\frac{r}{a} = \left(\frac{3V_f}{4n\pi}\right)^{\frac{1}{3}} \tag{5.4}$$

Combining Equation 5.4 with Equation 5.3, the following relationship can be formulated:

$$S = \pi \left(\frac{3V_f}{4\pi}\right)^{\frac{2}{3}} \tag{5.5}$$

Hence the area fraction can be determined by V_f. For a given volume fraction, the area fraction is determined based on Equation 5.5. However, if the ratio $\frac{r}{a}$ is larger than 0.05, it cannot be neglected, and the area fraction of EPS beads will be affected by the selected position (see Chapter 4 page 74). To simplify the problem, the ratio of $\frac{r}{a}$ is assumed to be lower than 0.05. Area fractions corresponding to the volume fractions from 10% to 50% are listed in Table 5.1 based on the assumption of a random distribution of EPS beads embedded within the concrete body.
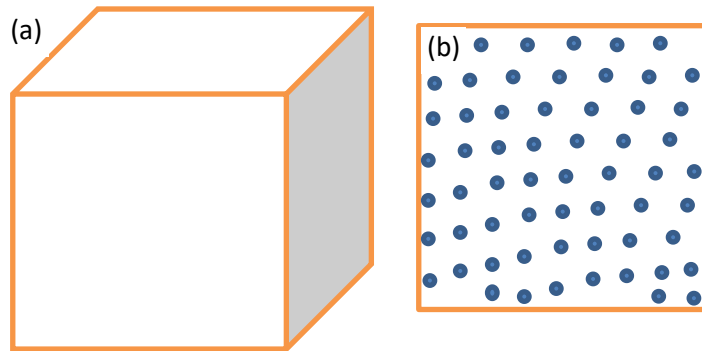
Figure 5. 1 Schematic of EPS area fraction in EPS concrete

Randomly distributed EPS beads within a cubic sample are illustrated in Figure 5.1. Area fraction increases with increasing the volume fraction of EPS beads.

As previously stated, the EPS area fraction is affected by many factors. Since the EPS beads are randomly distributed in the EPS concrete sample, each EPS bead has the same probability of appearing in any position within the sample. There is a general relationship between the volume fraction and averaged area fraction by Equation 5.5. The different averaged area fractions corresponding to the different volume fractions are listed in Table 5.1.

Table 5. 1 Area fraction corresponding to volume fraction

Volume fraction	Area fraction
0.1	0.26
0.15	0.34
0.2	0.41
0.25	0.48
0.3	0.54
0.35	0.60
0.4	0.66
0.45	0.71
0.5	0.76

Two radii of EPS beads are adopted in the following modelling process with 1.35 mm and 3.5 mm, respectively, and the volume fraction ranges from 10% to 50%.

The cubic shape experimental samples are employed and its size is $40 \times 40 \times 40 \text{mm}^3$.

In order to simulate EPS beads distribution, Matlab®[2] software is employed and a *m* file is compiled based on the following assumptions:

1) All EPS beads are rigid solid spheres, and that they experience no deformation during mixing or curing process;

2) All EPS beads have the same possibility appearing in any position within cubic sample;

3) All EPS beads are separated from each other, implying that any two EPS beads do not contacting with each other;

The *m* file for EPS beads distribution is compiled, and it is reported in appendix 1.

5.1.1 2D EPS beads distribution of *r*=3.5mm

For a certain volume fraction, the EPS beads are distributed randomly in three dimensions, and in any arbitrarily cross section not all EPS beads are cut through the spherical centre and not all circles has the same radius, but the maximum radius of these circles is the 3.5mm. For a certain volume fraction, the total number of EPS beads can be deduced from Equation 5.2, and the total number of EPS beads is given by:

$$\text{n} = fix(V_f \times \frac{\text{a}^3}{4 \times \pi \times \frac{r^3}{3}}) \tag{5.6}$$

where *fix* is a round function. According to Equation 5.6, the total number of EPS beads can be calculated and are listed in Table 5.2 together with related area fraction.

Table 5. 2 Relationship among volume fraction, total number and area fraction

volume fraction	total number	area fraction
0.05	18	0.16
0.1	36	0.26

---

[2] Matlab is a software trade mark developed by MathWorks.

0.15	53	0.34
0.2	71	0.41
0.25	89	0.48
0.3	107	0.54
0.35	125	0.60
0.4	143	0.66
0.45	160	0.71
0.5	178	0.76

During the experimental determination, all the EPS beads distribution images are for cross section of the cubic samples taken in 2 dimensions to facilitate comparison with the simulated results. To optimise the calculating times, when volume fraction exceeds 0.3, the EPS beads distribution is not calculated.

a)
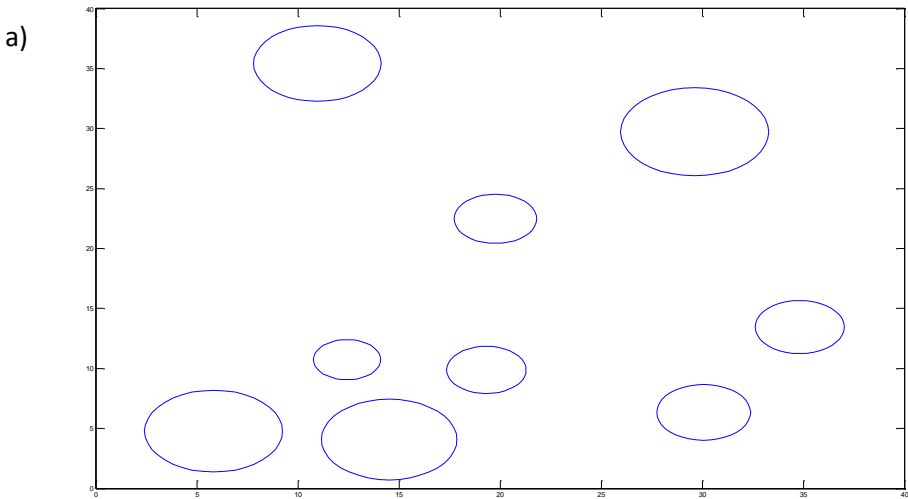
Figure 5. 2 Representation of EPS beads distribution of r=3.5mm, $V_f = 5\%$, s=16%; a) simulated EPS beads distribution; b) experimental images

Images of both experimental and simulated EPS bead distribution are predicted in Figure 5.2 with r=3.5mm and volume fraction of 5% and area fraction of 14% EPS beads, in which the circle zones represent EPS beads in Figure 5.2. In Figure 5.2 a), all the EPS beads are randomly distributed in this cross-section and the area fraction occupied by EPS beads is 14%. For the reason of random distribution, the cut EPS beads may have the different radii. The actual images of EPS beads distribution in an arbitrary cross-section (Figure 5.2 b) exhibit the some variation in EPS bead radii. Comparing Figure 5.2 a) and b), the simulated area fractions of EPS beads is very close to the experimental image, which proves the validity of random distribution model to describe EPS bead distribution. In addition, the total number of EPS beads in simulated image is a very similar to that for the experimental images despite EPS beads being randomly distributed in the cubic sample.

A further example of the comparison of experimental and simulated EPS bead distribution at a volume fraction of 20% is provided in Figure 5.3.

Figure 5. 3 EPS beads distribution of r=3.5mm, $V_f = 20\%$, S=34%; a) simulated EPS beads distribution; b) real experimental image

Figure 5.3 a) is for EPS beads randomly distributed by simulation, and Figure 5.3 b) is an image of a sawn section through a cubic EPS sample real experimental image. In Figure 5.3 a), EPS beads occupies 34% area fraction of the whole cross section. The increment of the area fraction leads to the averaged distance between any two neighbouring EPS beads less than that in Figure 5.2 a). Comparing Figure 5.3 with

Figure 5.2, it is evident that while the volume fraction of EPS beads increases from 5% to 20%, there are more EPS beads than that in Figure 5.2 b).
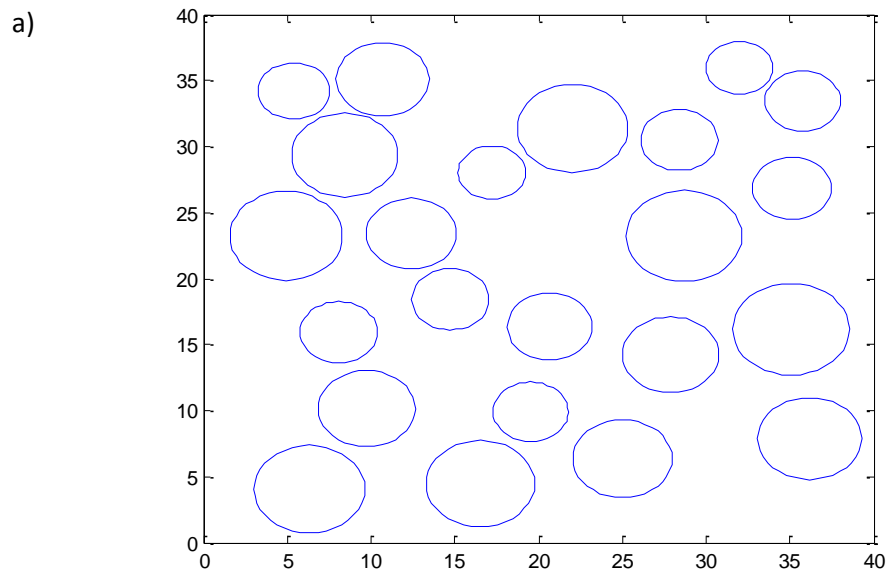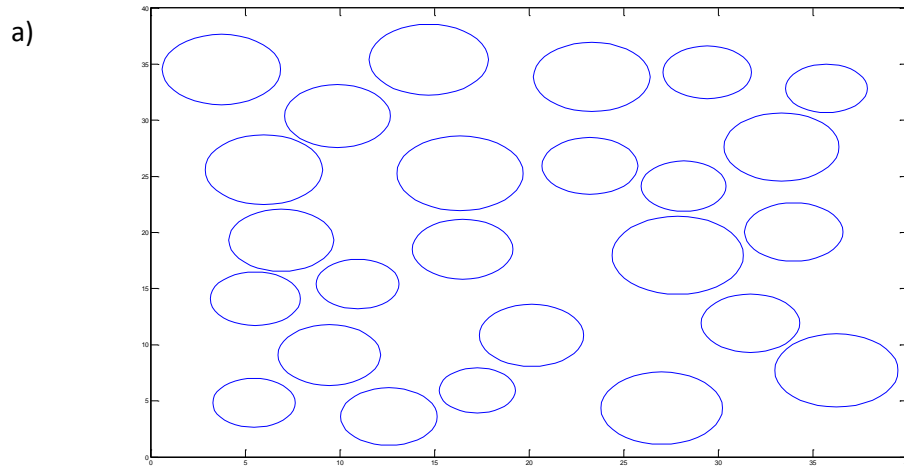

Figure 5. 4 EPS beads distribution of r=3.5mm, $V_f = 30\%$, S=41%; a) simulated EPS beads distribution; b) real experimental image

Similarly, Figure 5.4 is comparison of r=3.5mm EPS beads distributions with volume fraction of 30%. Figure 5.4 a) is EPS distribution by numerical simulating, and in Figure 5.4 b) EPS beads distribution is derived from experimental laboratory

procedures. As the EPS bead volume fraction increases, the EPS beads area fraction increases. For Figure 5.4 a), the area fraction reaches 41%, but experimentally the EPS beads distribution is affected by random factors during mixing process, and appears different (Figure 5.4 b). The area fraction of EPS beads in the different cross section will vary , so on average there will be a little difference between Figure 5.4a) and 5.4 b). However, the trend for both random model and experimental method is the same that as the EPS beads volume fraction increases, there are more EPS beads appearing in the cross section.

When the volume fraction exceeds 30%, more EPS beads are appeared in the cross section of sample leading to more computing time. Therefore, EPS beads random distribution is not simulated when the volume fraction exceeds 30%.

Based on evidence from Figures 5.2, 5.3 and Figure 5.4, the EPS beads distribution model can simulate the random distribution of EPS beads in concrete, and the simulated EPS beads distributions closely approximate the real EPS distribution established experimentally.

5.1.2 2D EPS beads distribution of r=1.35mm

Applying Equation 5.6, when the radius of EPS beads is 1.35mm, r=1.35mm, the total number of EPS beads in EPS concrete along with the area fraction is listed in Table 5.3.

Table 5. 3 Relationship among volume fraction, total number and area fraction

volume fraction	total number	area fraction
0.05	310	0.16
0.1	621	0.26
0.15	931	0.34
0.2	1242	0.41
0.25	1552	0.48
0.3	1863	0.54
0.35	2173	0.60
0.4	2484	0.65
0.45	2794	0.71
0.5	3105	0.76

From Table 5.3, it is evident that total number of EPS beads varied from 310 to 3105 while the volume fraction is from 5% to 50%. To economise on computing time, only 5% and 10% volume fractions of EPS bead distribution are simulated.

a)

b)
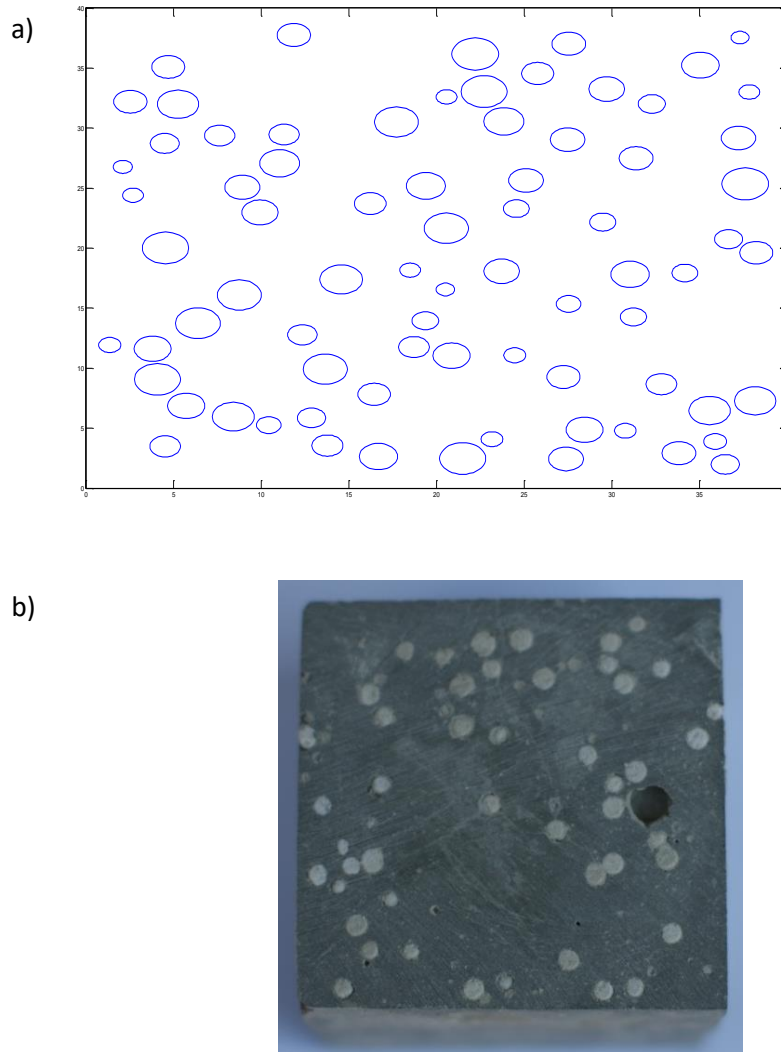
Figure 5. 5 EPS beads distribution while r=1.35mm, and volume fraction is 5%; a) is simulated EPS beads distribution; b) is the experimental image

The r=1.35mm EPS beads distribution by simulated and experimental method with volume fraction of 5% are imaged in Figure 5.5. In Figure 5.5 a) the EPS area fraction is 16% while EPS beads volume fraction is 5%. In Figure 5.5 b), Experimental image of r=1.35mm EPS bead distribution in an arbitrary cross-section is depicted in Figure5.5 b). Comparing Figure 5.5 a) with 5.5 b), the

EPS area fraction of the experimental image is little different from the simulated results.

a)

b)
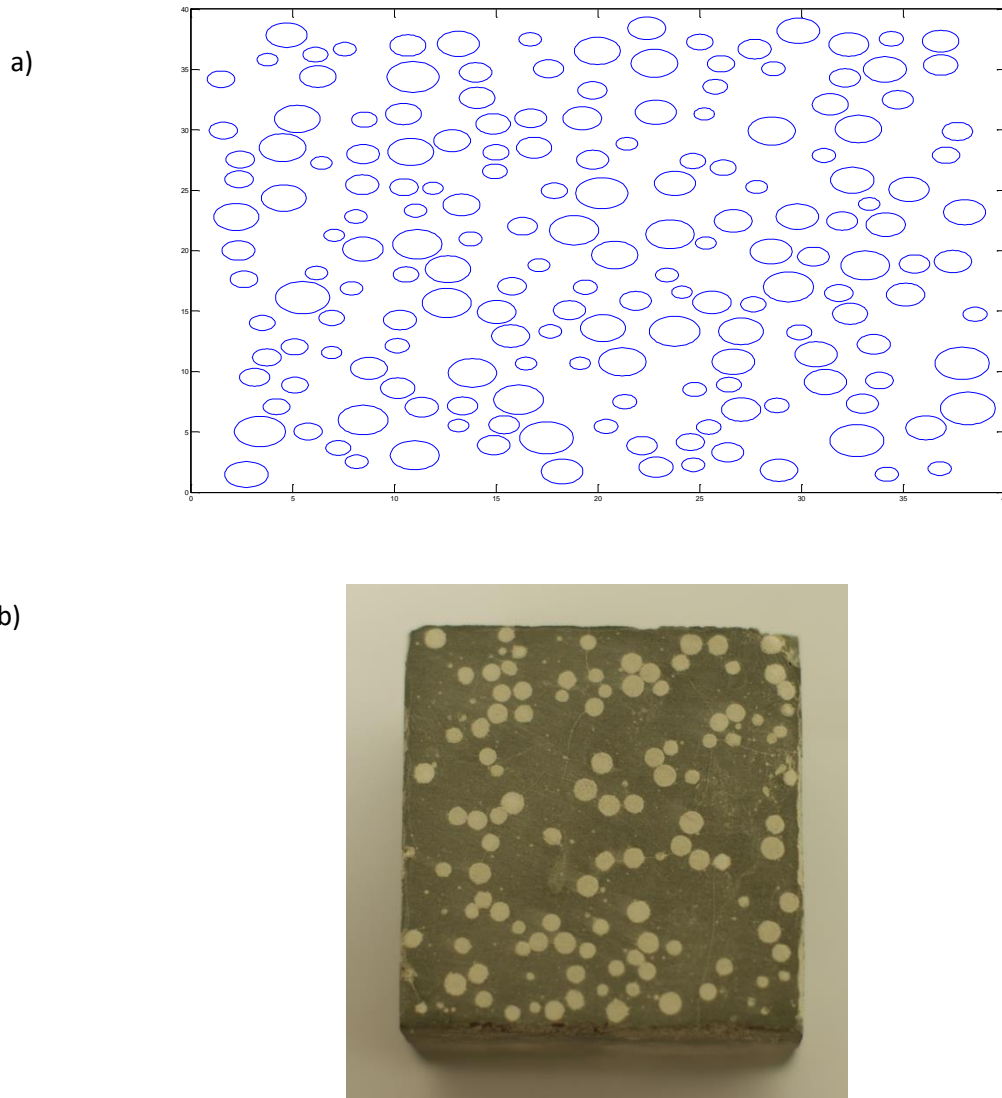
Figure 5. 6 EPS beads distribution while *r*=1.35mm, and volume fraction is 10%; a) is simulated EPS beads distribution, b) is the experimental image.

Similar images are presented in Figure 5.6 for *r*=1.35mm EPS beads distribution but for a volume fraction of 10%, in which the circles represent EPS beads, and the blank space for concrete matrix; Figure5.6 b) reveals the experimental images of EPS beads distribution and the white solid circles are EPS beads and remainder concrete. When the volume fraction is 10% and the averaged area fraction was

26%(Figure 5.6 a), there are many EPS beads appearing in the experimentally solid concrete cross section. Comparing Figure 5.6 a) with Figure 5.5 b), there are more EPS beads appearing in cross sections when volume fraction is 10%.

Figure 5.2 to 5.6 confirm that the simulated distribution of EPS beads by Matlab program closely matches those obtained by experimental method.

5.2 3D EPS Beads Distribution Model

To generate the randomly distributed EPS beads configuration in 3 dimensions, the Python language is utilized, and this program has the advantage that the geometrical figure generated by this program can be imported directly into the Abaqus software, a necessary important step for simulating stress distribution.

It is necessary to assume that the positions of EPS beads centre are generated randomly without overlapping; and the distances between any two EPS beads centres are greater than the sum of the two radii of EPS beads. The above assumption is expressed as Equations 5.7 and 5.8.

$$\text{p}(x, y, z) = \{r + (a - r) * rand, r + (a - r) * rand, r + (a - r) * rand\} \quad (5.7)$$

where p is the coordinate position of the EPS bead centre, r is the radius of EPS bead, a is the length of each edge of the cubic sample, and *rand* is a random function to generate random decimal. In Equation 5.7, it is implied that all the EPS beads are within the cubic sample.

$$\text{d}_{\text{ij}} = \sqrt{\left(x_i - x_j\right)^2 + \left(y_i - y_j\right)^2 + \left(z_i - z_j\right)^2} \geq r_i + r_j \quad (5.8)$$

where d_{ij} is the distance between the ith EPS bead centre and the jth EPS bead centre, *x,y,z* are the coordinate position, subscript i and j are the ith and the jth EPS beads, and r is radius of the EPS bead. In Equation 5.8, the distance between any two EPS beads is greater than the sum of the radii of both EPS beads, and all the EPS beads are separated by each other.

Initially, the first two positions of EPS beads are selected according to Equation 5.7 and their centre marked as a series number. Next, the distance between the two

beads is calculated according to Equation 5.8. If the distance matches Equation 5.8, these positions are valid, or else, the second position would be relocated according to Equation 5.7. And then, repeating the above steps until the volume fraction reaches the planned volume fraction.

According to Table 5.2 and Table 5.3, the total number of EPS beads for r=3.5mm and 1.35mm are calculated for different volume fractions; and then these EPS beads are randomly placed in the concrete sample. The EPS concrete samples' size is $40 \times 40 \times 40\text{mm}^3$.

5.2.1 3D r=3.5mm EPS beads distribution
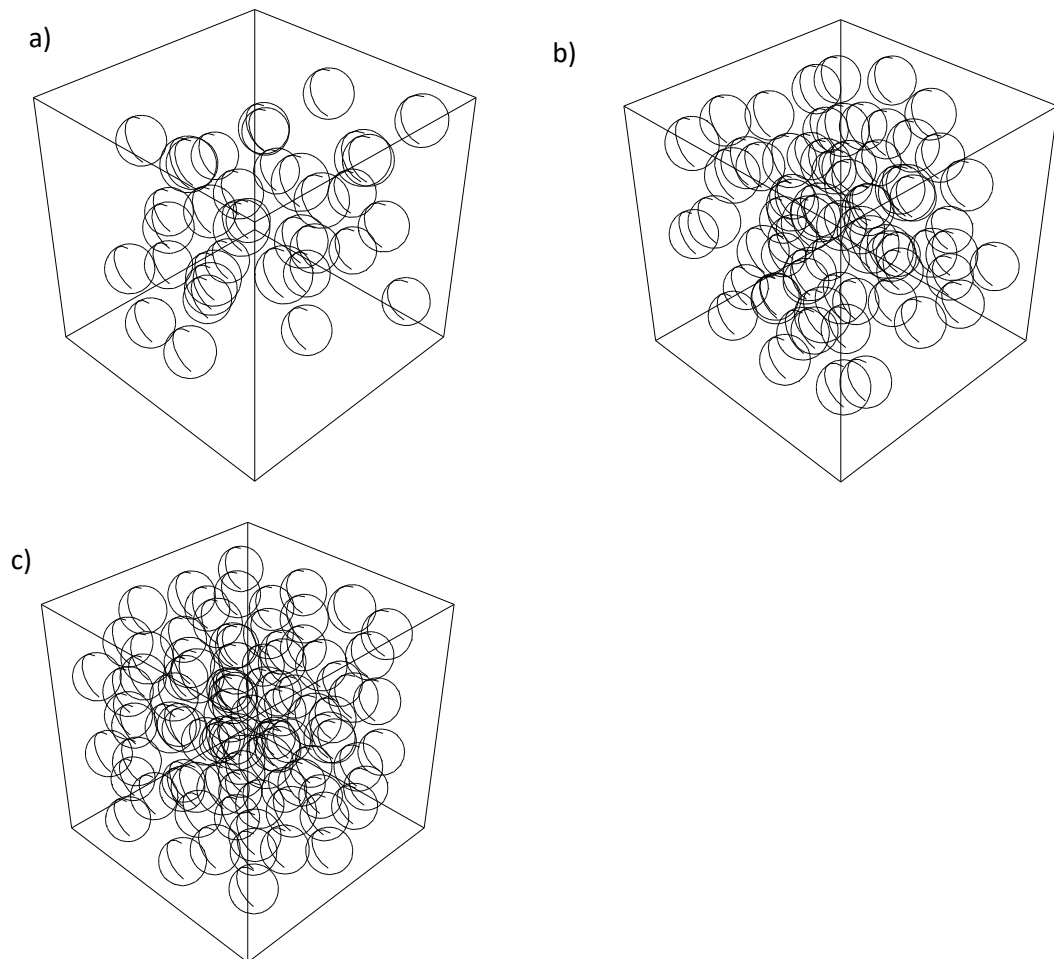
Figure 5. 7 3-dimensional $r = 3.5$mm EPS beads distribution, a) is $V_f = 10\%$; b) is $V_f = 20\%$; c) is $V_f = 30\%$

Figure 5.7 represent a three-dimensional $r = 3.5mm$ EPS beads random distribution in concrete by using numerical method. Figure 5.7 a) for 10%, Figure 5.7 b) for 20%, and Figure 5.7 c) for 30% volume fraction of EPS beads. The black spheres in Figure 5.7are the EPS beads and the remainder concrete. The central positions of the EPS beads are placed randomly, so the EPS beads can be placed in any internal position of sample. When the volume fraction is 10%, the total number of $r = 3.5$ mm EPS beads of is 36. These EPS beads are laid sparsely in the cubic sample. When the volume fraction increases from 10% to 20%, (Figure 5.7 b), the total number of EPS also increases from 36 to 71, and the average distance between neighbouring EPS beads became less than in Figure 5.7 a). When the EPS beads volume fraction increases from 20% to 30%, (Figure 5.7 c), the total number of EPS beads rises to 107, and the averaged distance between neighbouring EPS beads becomes even less than that for both 10% and 20% volume fractions.

5.2.2 3D r=1.35 mm EPS beads distribution

With the reduction of radius to 1.35mm EPS bead, there are more EPS beads with the same volume fraction than with r=3.5mm EPS beads. Hence, in order to efficiently use the calculation time, only 5% and 10% volume fraction EPS beads distributions are calculated.
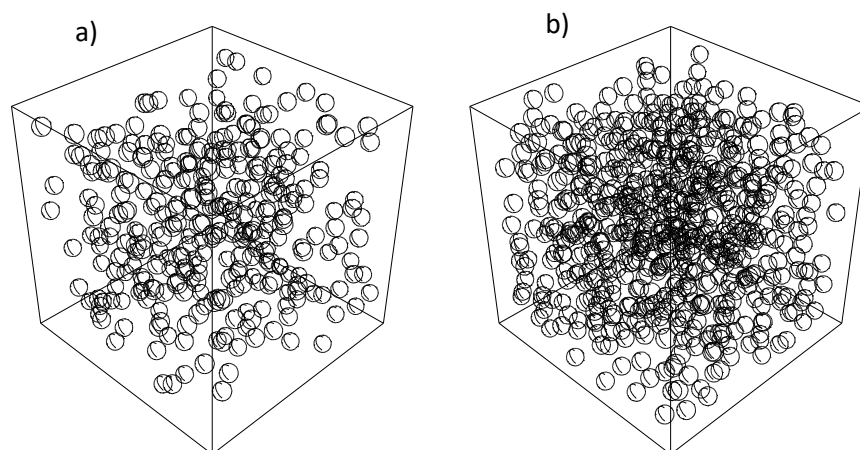
Figure 5. 8 3-dimensional $r = 1.35mm$ EPS beads distribution, a) is $V_f = 5\%$; b) is $V_f = 10\%$

Finally, a three-dimensional $r = 1.35$mm EPS beads randomly distributed in concrete is given in Figure 5.8. Figure 5.8 a) is for a 5% volume fraction of EPS bead and total EPS bead number of 310, and Figure 5.8 b) is for a 10% volume fraction of EPS beads, and the total EPS beads number is 621. As volume fraction of EPS beads increases, the more EPS beads are placed in sample. Comparing Figure 5.8 with Figure 5.7, it can be found that the smaller radius of EPS beads led to the EPS distribution more homogeneous.

5.3 Summary

Employing numerical simulation mythology, 2-dimensional EPS beads distribution and 3-dimensional EPS beads distribution can be simulated, and the simulated EPS beads distributions for different volume fraction are compared with experimental images. The following conclusions are obtained:

1) The program compiled by Matlab is applied to random 2-dimensional of EPS beads distribution, and the simulated EPS distributions closely matched these obtained by actual experiments.

2) The program coded by Python is developed to describe the random distribution EPS beads in 3 dimensions. The EPS beads distribution generated by the program can be imported into Abaqus software, which provides crucial geometry information to calculate the stress distribution within EPS concrete.

CHAPTER 6 SIMULATION OF THE STRESS DISTRIBUTION WITHIN FOAM CONCRETE

The compressive strength of EPS concrete is determined by the EPS volume fraction and EPS particle size [79, 108]. The EPS beads distribution in a concrete body directly affects the interface area fraction of EPS beads, which in turn exerts influence on the compressive strength. Reflecting the manufacturing process, the EPS beads were randomly distributed throughout the concrete. Likewise, the compressive strength of foam concrete was also determined by pore volume fraction as noted by others researchers [7, 9, 13]. However, the quantitative impact of pore size on compressive strength remains to be solved. Employing EPS concrete to investigate the pore size effect on the compressive strength provided a method to calculate the compressive strength of foam concrete. The proposed approach of this study is summarised in the following Figure 6.1.
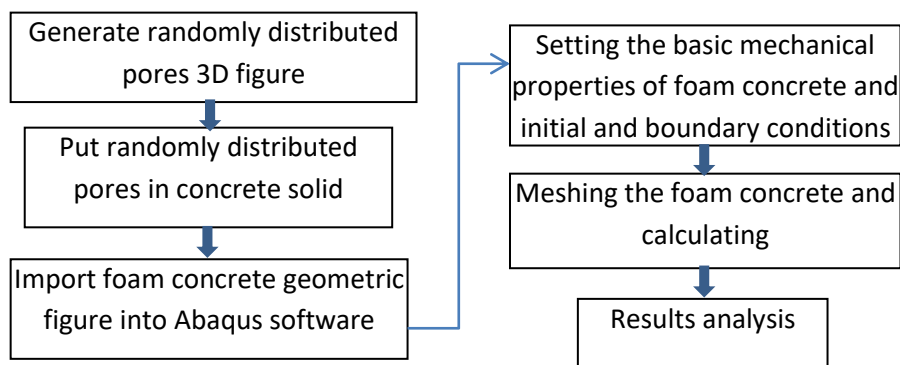
Figure 6. 1 Flow chart of the research strategy

Devising random distribution geometric figure is the initial step for the simulation. In this thesis a program is compiled by using the Python language to generate random distribution pores in EPS concrete as described in Chapter 5. The program is imported into Abaqus software by subscript mode. After the geometric figure is imported into Abaqus software, material properties are input, and boundary conditions and initial conditions are selected. For single direction loading, the loading force can be set as experimental value. A tetrahedral grid is applied to

meshed pores based on spherical shape of pores embedded in concrete sample. Finally, simulated results are displayed, analysed and discussed.

6.1 Physical Model

Since concrete is a brittle material, there is little plastic deformation during the loading process, so deformation can be regarded as an elastic process.

Applied Mises equivalent stress under the static stress condition [113], at equilibrium, the effective stress on each unit during the loading process is expressed as:

$$f_e = \sqrt{\frac{1}{2}\left[\left(\sigma_x - \sigma_y\right)^2 + \left(\sigma_y - \sigma_z\right)^2 + (\sigma_z - \sigma_x)^2 + 6\left(\tau_{xy}^2 + \tau_{yz}^2 + \tau_{zx}^2\right)\right]} \qquad (6.1)$$

where f_e is effective stress, σ_x is the main stress in the x direction, σ_y is the main stress in the y direction, σ_z is the main stress in the z direction, τ_{xy} is the shear stress in the xy face, τ_{yz} is the shear stress in the yz face, and τ_{zx} is the shear stress in the zx face. According to Equation 6.1, the effective stress distribution of concrete under any loading process can be calculated.

When the effective stress reaches or exceeds the compressive strength of concrete, the concrete fails:

$$f_e \geq f_c' \qquad (6.2)$$

where f_c' is the compressive strength of concrete.

Due to the random distribution of pores in the concrete solid, some pores experience higher stress than others. When the mounting stress in the sample reaches the compressive strength of foam concrete, it begins to break and fail at the pore level. Therefore, the effective stress distribution can be used to predict the weakest position within foam concrete.

6.2 Simulation Parameters

For the simulation to approach to the experimental situation, the physical properties play a fundamental role in affecting the simulated results. The physical properties of foam concrete are regarded as consisting of two phases mixed together: one solid (i.e. concrete) and the other void space (i.e. pores). While the concrete matrix bears the main strength, the strength of pores is regarded as negligible.

Similarly, the boundary and initial conditions have a direct impact on the stress and its distribution. Therefore, boundary and initial conditions are fixed based on the experimentally determined condition.

6.2.1 Physical properties

The mechanical properties of foam concrete are measured experimentally using dense concrete sample. The testing results on the key properties of concrete are listed in Table 6.1.

Table 6. 1 Mechanical properties of concrete

	Density (kg/m^3)	Young's modulus (GPa)	Poisson ratio	Compressive strength (MPa)
concrete	2240	2.1	0.25	60.6

* mechanical properties of concrete are measured experimentally.

6.2.2 Boundary and initial condition

1. Initial condition

Initially, the foam concrete sample is placed free between pressing heads. Once loading commences, loading pressure increases continuously along with loading time. The loading pressure is set as a linear function of time given by:

$$P(t) = 0.5 \times t \tag{6.3}$$

where t is time (s), and $P(t)$ is loading pressure (MPa). The maximum loading pressure is set as 60 MPa, equivalent to that for the experimentally measured concrete.

2. Boundary condition

The bottom face of the sample is set as the anchored condition, the top face as the loading surface, which is the same as the actual testing situation, and the other surfaces as free boundary conditions.

6.2.3 Meshed grid

Within the foam concrete sample, there are many spherical shaped pores, so a theoretical tetrahedral meshed grid is applied to represent their distribution. The finer meshed size, the more meshing and computing time required. This enforces a compromise between computing efficiency and precision of generated data. In order to save meshing yet give reasonable prediction and reliable precision, 2 mm meshed size is employed for r=1.35 mm pores in the foam concrete, and 4 mm meshed size is employed for r=3.5 mm pores in the foam concrete, the. These meshed arrays are depicted in Figure 6.2.
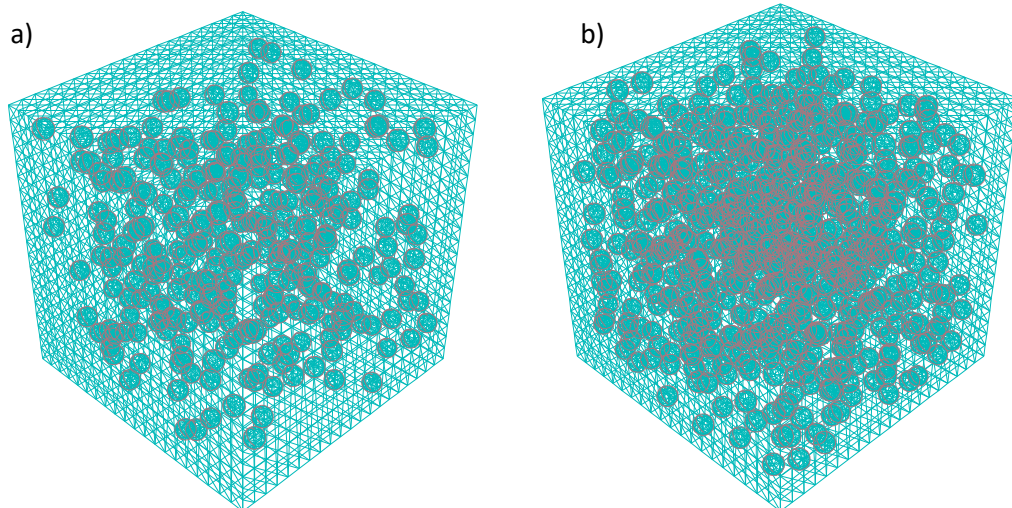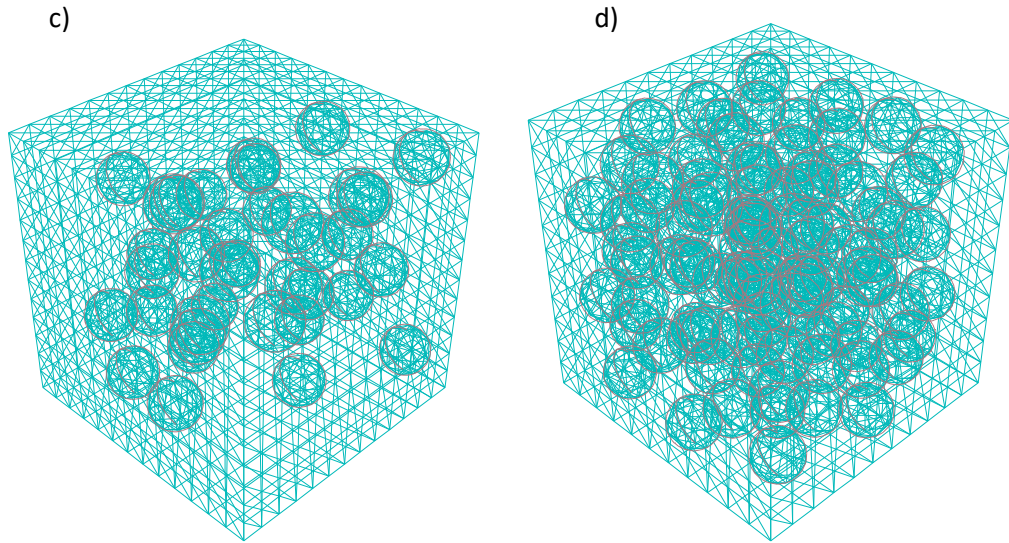
Figure 6. 2 Meshed grid for a) $r = 1.35\text{mm}$, $V_f = 5\%$; b) $r = 1.35\text{mm}$, $V_f = 10\%$; c) r = 3.5mm, $V_f = 10\%$; d) $r = 3.5\text{mm}$, $V_f = 30\%$.

The meshed grids of different radii and different volume fractions of pores in foam concrete samples are shown in Figure 6.2, in which a) is $r = 1.35$ mm and pore volume fraction is 5%; b) is $r = 1.35$ mm and pore volume fraction is 10%; c) is $r = 3.5$ mm and pore volume fraction is 10%; d) is $r = 3.5\text{mm}$ and pore volume fraction is 30%. As the pores volume is embedded in the concrete, the total number of meshed unit increases accordingly.

6.3 3-dimensional Stress Distribution Simulation

6.3.1 3D Random distribution of pores

The first step is to generate 3D pores random distribution model in cubic solid concrete, and then the work of simulating of influences of pore size and volume fraction of pores on compressive strength can be completed. 3D randomly distributed pores are generated with a short program written in Python code, in which different sizes and volume fractions of pores are employed to show 3-dimensional random distribution. In all the models size of pore is assumed as a constant during the mixing and solidification process, i.e. the pores are rigid. The diagrammatic representation of the 3D pore random distribution in concrete are depicted in Figures 5.7 and 5.8 in the 5th Chapter.

6.3.2 3D stress distributions

Stress distribution can locate the position of the maximum stress and determine of the initial failure position in foam concrete sample. Since there is very small plastic deformation during loading (fibre reinforced concrete can have plastic deformation), deformation process is regarded as completely elastic in this study. When local stress reaches the compressive strength of plain concrete, a foam concrete sample can be regarded as failure.

1. Stress distribution with $r = 3.5$mm pores

    (1) $V_f = 10\%$ stress distribution

Stress distribution during loading process and the maximum stress in one cross-section is calculated in Figure 6.3. Different colours represent different stress values, and which vary as loading time changes.
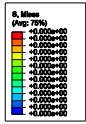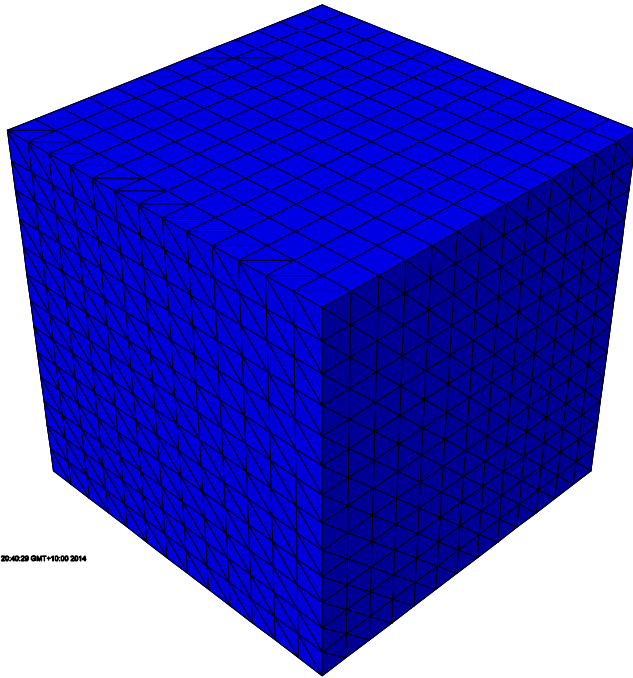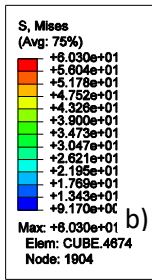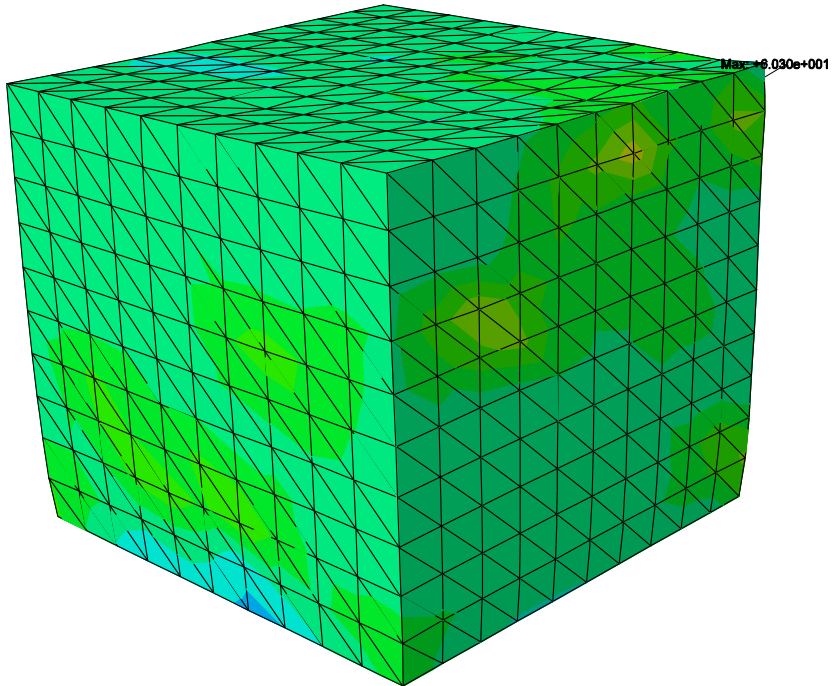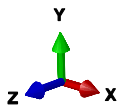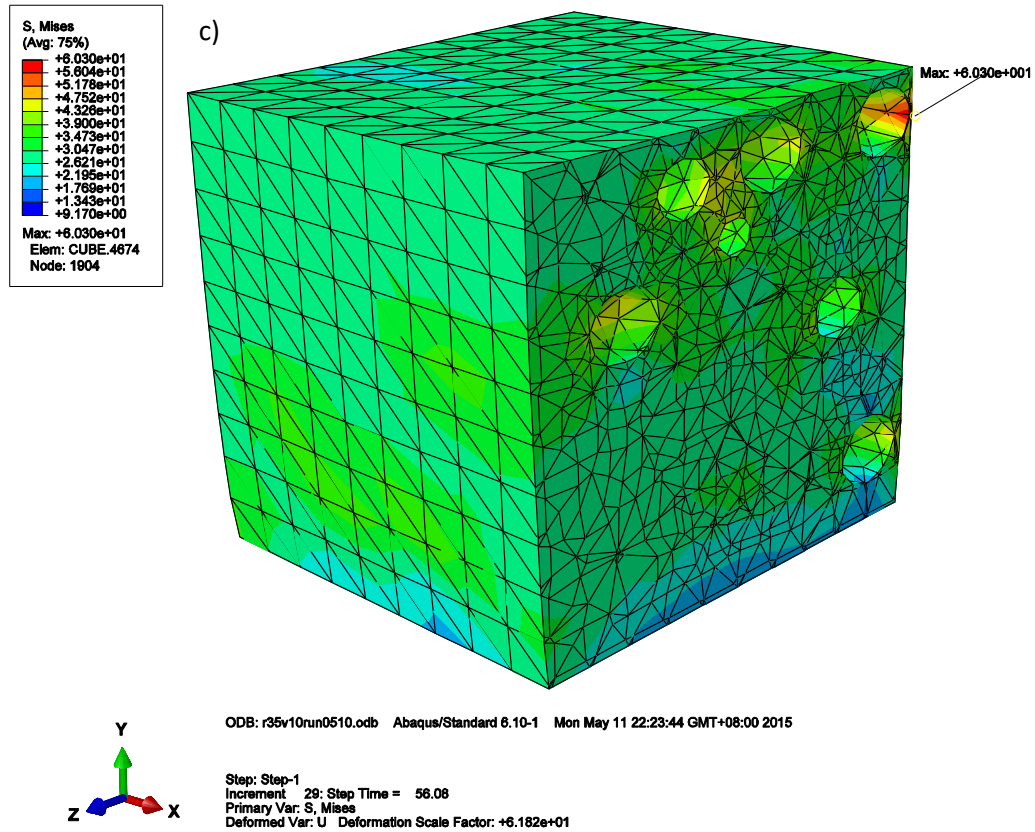
Figure 6. 3 Stress distribution of foam concrete with a 10% volume fraction and r=3.5mm pores; a) t=0s; b) t=95s on surface; c) t=95s on the maximum compressive strength cross-section.

At commencement of the loading process, the stress value is zero in the sample. When t=95s, in Figure 6.3 b), the stress distribution on the surface of the sample is plotted and the maximum stress value is 47 MPa. Viewing the different cross-sections of the sample, the maximum stress position is obtained in Figure 6.3 c) and its value is 60MPa when the position failures. Because the force is loading linearly, the effective compressive strength is given by: $f_e = 60 \times \frac{95}{120} = 47.5$MPa

Since the maximum stress position is located close to the pores, especially as repeated in Figure 6.3 c), the maximum stress position is also located between a pore and surface of the sample. The distance between the pores or pore and surfaces has a direct impact on the stress concentration. The smaller the inter pore distance is, the greater stress concentration will be.

(2) Stress distribution for $V_f = 20\%$ foam concrete

Stress distributions for 20% volume fraction pores foam concrete is depicted in Figure 6.4, in which different colour represents the different stress values.

S, Mises
(Avg: 75%)
+4.970e+01
+4.664e+01
+4.358e+01
+4.052e+01
+3.746e+01
+3.440e+01
+3.134e+01
+2.828e+01
+2.522e+01
+2.215e+01
+1.909e+01
+1.603e+01
+1.297e+01
+9.911e+00
+6.850e+00
+3.789e+00

c)

Y
Z X
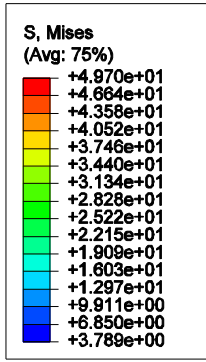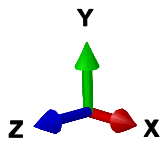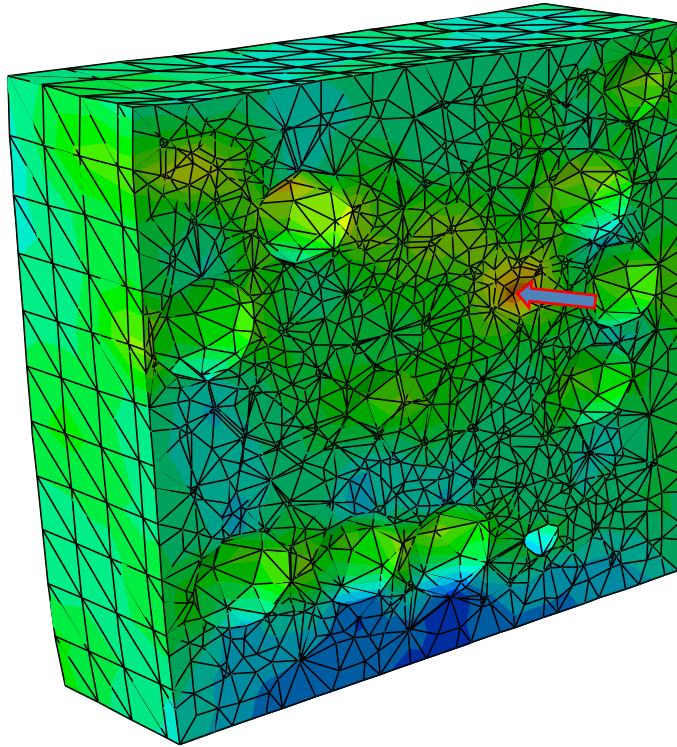
ODB: r35v20run0510.odb   Abaqus/Standard 6.10-1   Tue May 12 00:30:45 GMT+(

Step: Step-1
Increment   10: Step Time =   37.94
Primary Var: S, Mises
Deformed Var: U   Deformation Scale Factor: +7.787e+01

Figure 6. 4 Stress distributions for foam concrete with 20% volume fraction and r=3.5mm pores; a) t=0s; b) t=38s; c) t=38 and d) t=57s at different cross section stress distributions.

Figure 6.4 a) is the initial stress distribution at the stress value of 0 MPa. As the loading time increased to 38s, in Figure 6.4 b), the maximum stress value on the sample surfaces reaches 50 MPa. Considering the stress distribution in different cross-sections, the maximum stress position is located with a red arrow in Figure 6.4 c). When t=57s, the maximum stress rises to 76MPa, in Figure 6.4 d). In Figure 6.4 c) the maximum stress in sample is 49.7 MPa, but by t=57s the maximum stress reaches 76MPa. Using a linear fitting method, the time when the maximum stress reaches 60 MPa is $t = 38 + (60 - 50) \times \frac{57-38}{76-50} = 45s$. The effective compressive strength of the foam concrete sample is determined to be $f_e = 60 \times \frac{45}{120} = 22.5\text{MPa}$.

Comparing Figure 6.4 with Figure 6.3, it is established that for the same loading force the maximum stress value is higher as the volume fraction increases, indicating that the higher volume fraction leads to a higher stress concentration, and the more readily failure sample .

(3) $V_f = 30\%$ stress distribution

The stress distribution with 30% volume fraction pores in foam concrete is calculated in Abaqus and depicted in Figure 6.5.
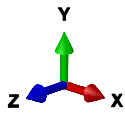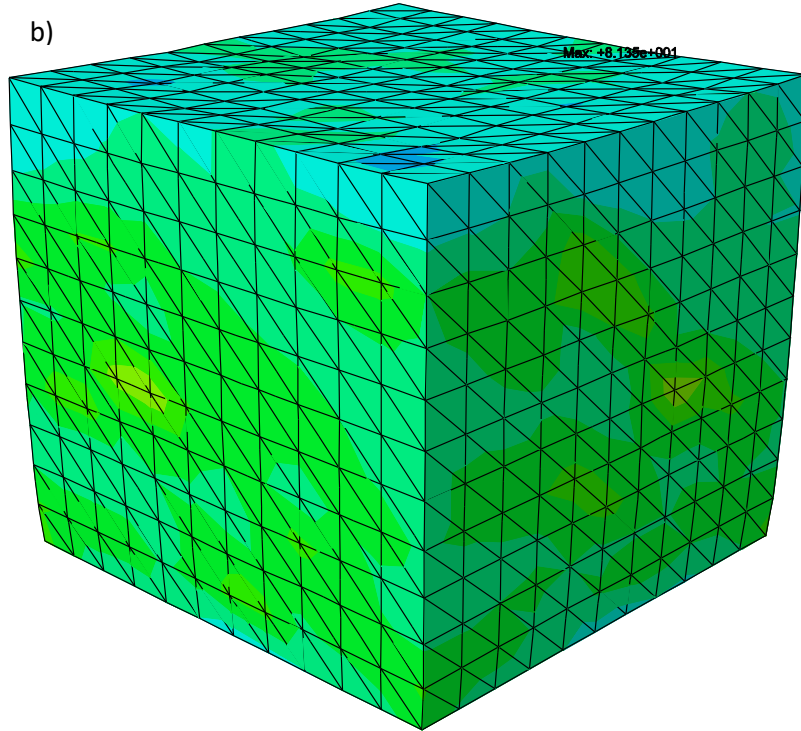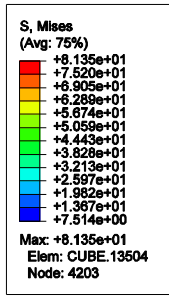
S, Mises
(Avg: 75%)
+8.135e+01
+7.520e+01
+6.905e+01
+6.289e+01
+5.674e+01
+5.059e+01
+4.443e+01
+3.828e+01
+3.213e+01
+2.597e+01
+1.982e+01
+1.367e+01
+7.514e+00

Max: +8.135e+01
Elem: CUBE.13504
Node: 4203

b)

Max: +8.135e+001

ODB: r35v30run0510.odb   Abaqus/Standard 6.10-1   Mon May 11 23:30:31 GMT+08:00 2015

Step: Step-1
Increment   11: Step Time =   57.17
Primary Var: S, Mises
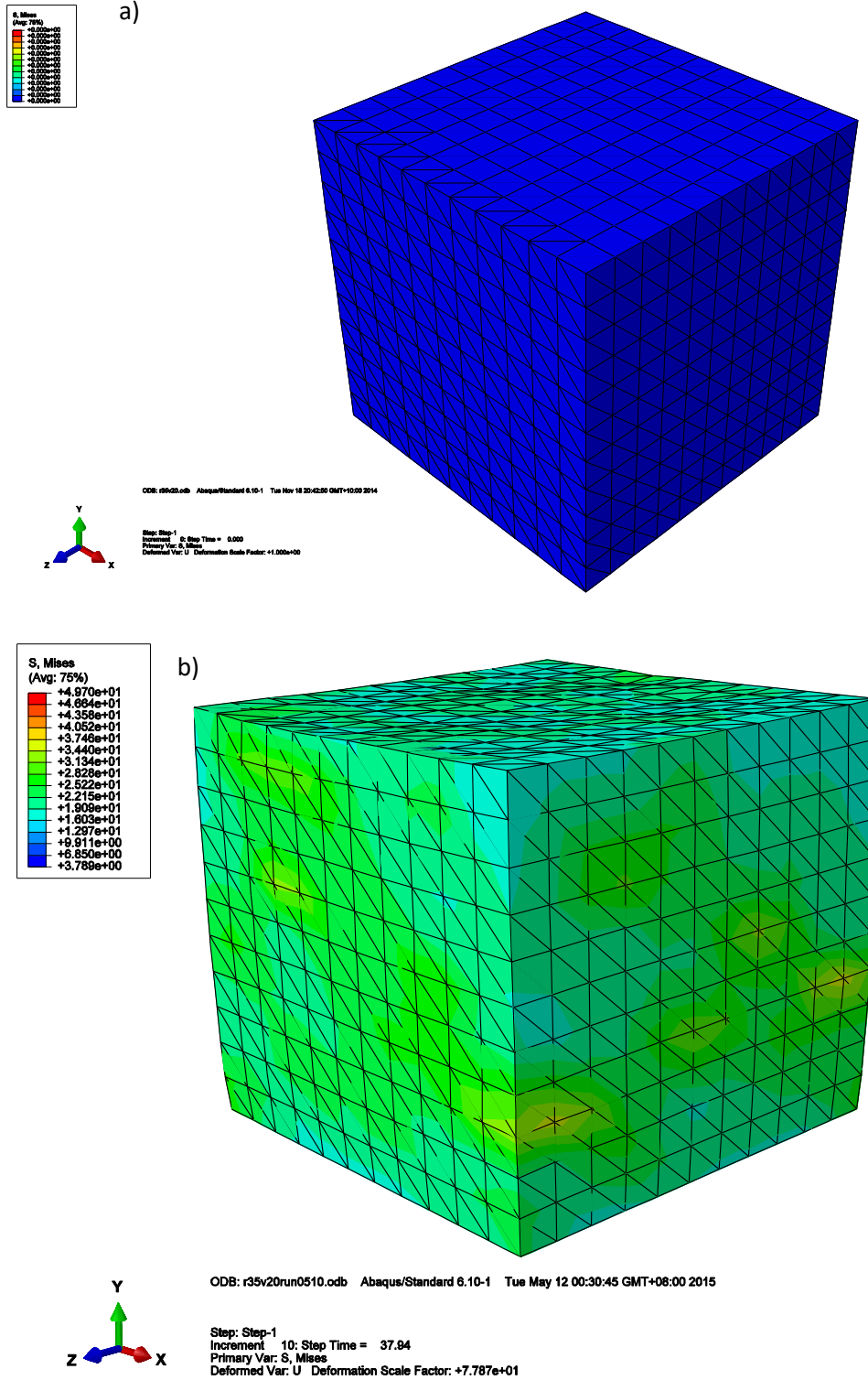Deformed Var: U   Deformation Scale Factor: +4.657e+01

S, Mises
(Avg: 75%)
+5.351e+01
+4.946e+01
+4.542e+01
+4.137e+01
+3.732e+01
+3.327e+01
+2.923e+01
+2.518e+01
+2.113e+01
+1.708e+01
+1.304e+01
+8.990e+00
+4.943e+00

Max: +5.351e+01
Elem: CUBE.13504
Node: 4203

c)

Max: +5.351e+001
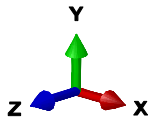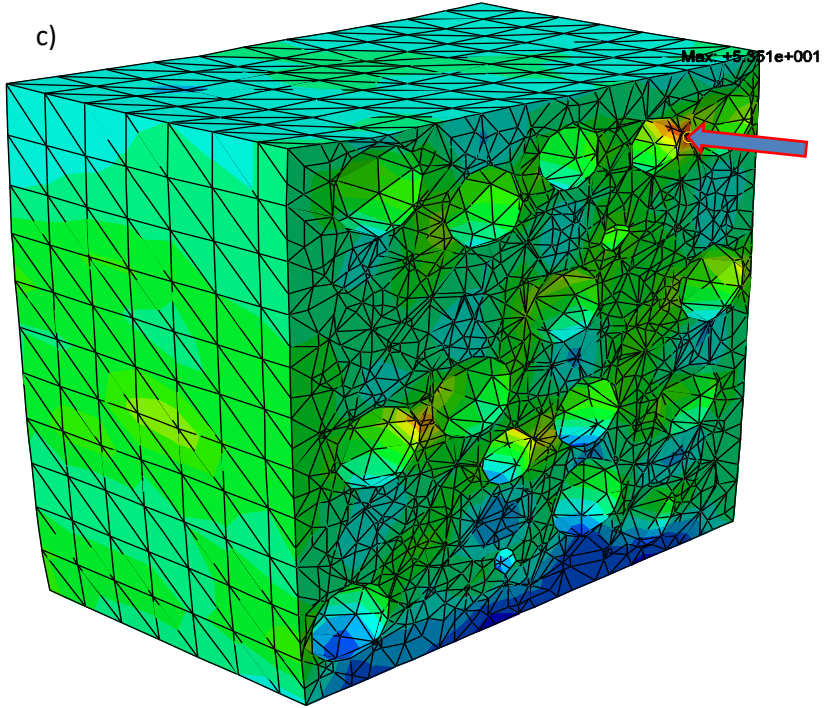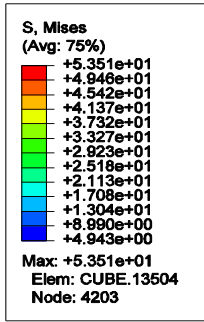
ODB: r35v30run0510.odb   Abaqus/Standard 6.10-1   Mon May 11 23:30:31 GMT+08:00 2015

Step: Step-1
Increment   10: Step Time =   37.94
Primary Var: S, Mises
Deformed Var: U   Deformation Scale Factor: +7.080e+01

110

S, Mises
(Avg: 75%)
+8.135e+01
+7.520e+01
+6.905e+01
+6.289e+01
+5.674e+01
+5.059e+01
+4.443e+01
+3.828e+01
+3.213e+01
+2.597e+01
+1.982e+01
+1.367e+01
+7.514e+00
Max: +8.135e+01
Elem: CUBE.13504
Node: 4203

d)

Max: +8.135e+001

Y
Z   X

ODB: r35v30run0510.odb   Abaqus/Standard 6.10-1   Mon May 11 23:30:31 GMT+08:00 2015

Step: Step-1
Increment   11: Step Time =   57.17
Primary Var: S, Mises
Deformed Var: U   Deformation Scale Factor: +4.657e+01

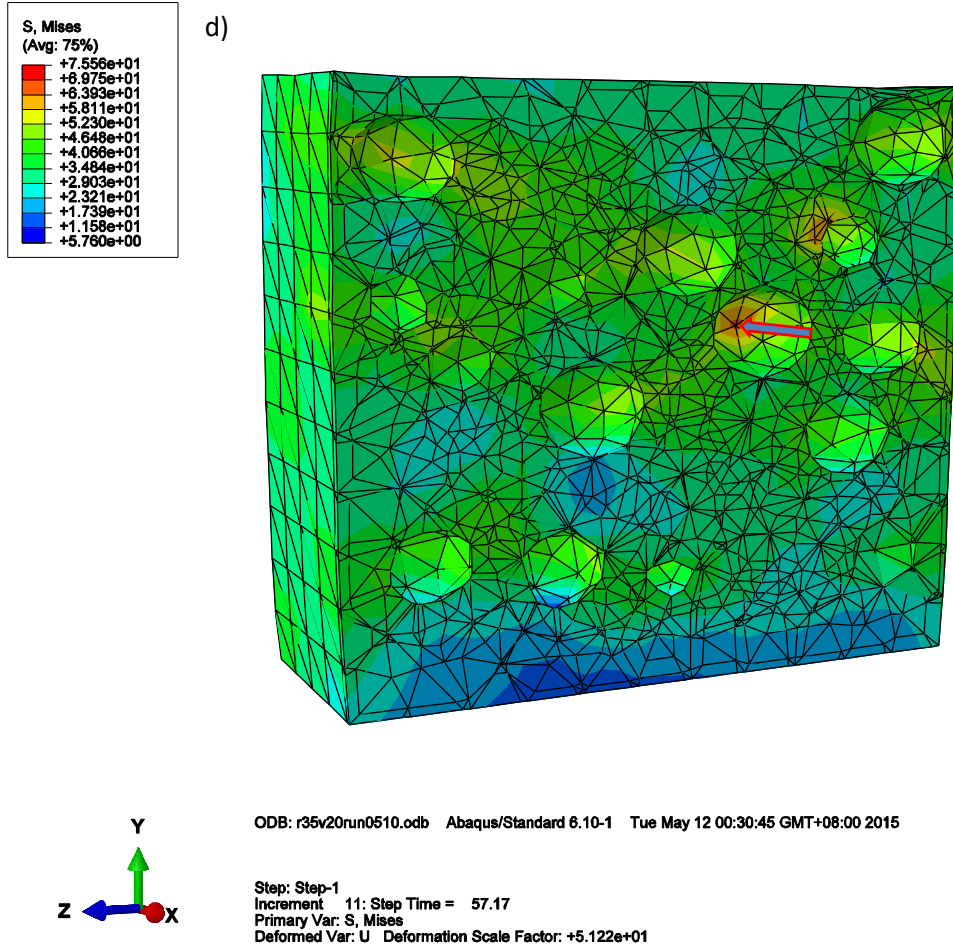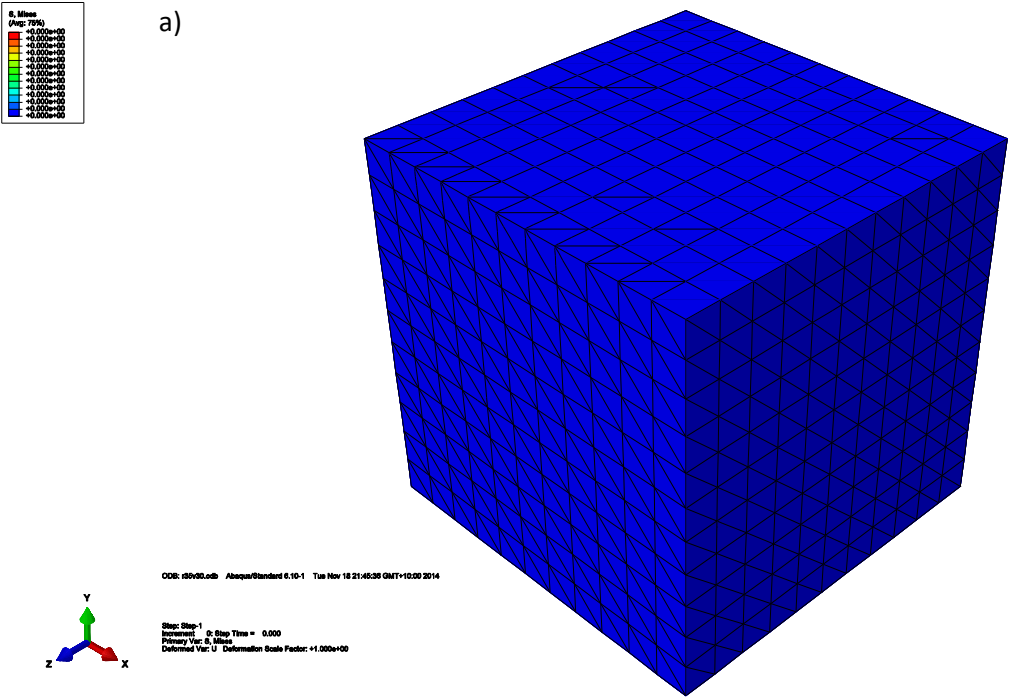Figure 6. 5 Stress distributions for foam concrete with 30% volume fraction and r=3.5mm pores; a) t=0s; b) t=38s; c) and d) are the maximum stress cross-section at t=38 and t=57s, respectively.

Figure 6.5 a) is the initial state of the foam concrete sample, the stress distribution is uniformed at 0MPa. At 38s, in Figure 6.5 b), the maximum stress value in the sample reaches 53.5 MPa as marked on the top of the sample. This value approaches to the compressive strength of concrete. Viewing the cross section, the maximum stress place at t=38s is located in Figure 6.5 c). For the next calculating step, the loading time is 57s, and the maximum compressive strength rises to 81MPa on the right upper corner of Figure 6.5 d). This significantly exceeds the threshold strength of 60 MPa for dense concrete sample and eventually the sample failures. Using a linear fitting method, the time when the maximum stress reaches 60 MPa is given by

$t = 38 + (60 - 53.5) \times \frac{57-38}{81-53.5} = 42.5s$. At 42.5s, the effective compressive

strength of the foam concrete sample is determined to be $f_e = 60 \times \frac{42.5}{120} = 21$MPa.

2. Stress distribution with r = 1.35mm pores

(1) Volume fraction is 5%
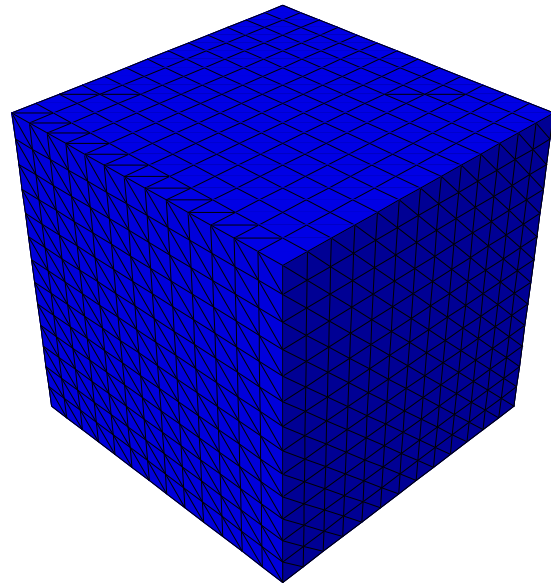
S, Mises
(Avg: 75%)
+6.011e+01
+5.570e+01
+5.129e+01
+4.687e+01
+4.246e+01
+3.805e+01
+3.364e+01
+2.922e+01
+2.481e+01
+2.040e+01
+1.598e+01
+1.157e+01
+7.157e+00
Max: +6.011e+01
Elem: CUBE.37689
Node: 4828

c)
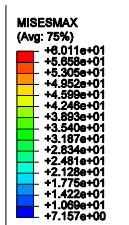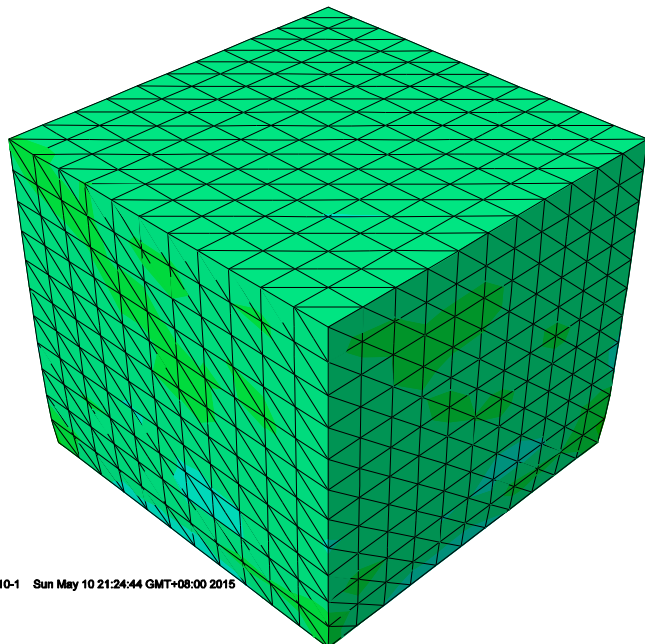
ODB: newr135v5run1.odb   Abaqus/Standard 6.10-1   Tue May 12 16:01:19 GMT+08:00 2015
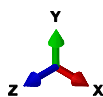
Step: Step-1
Increment   54: Step Time =   52.75
Primary Var: S, Mises
Deformed Var: U   Deformation Scale Factor: +7.643e+01
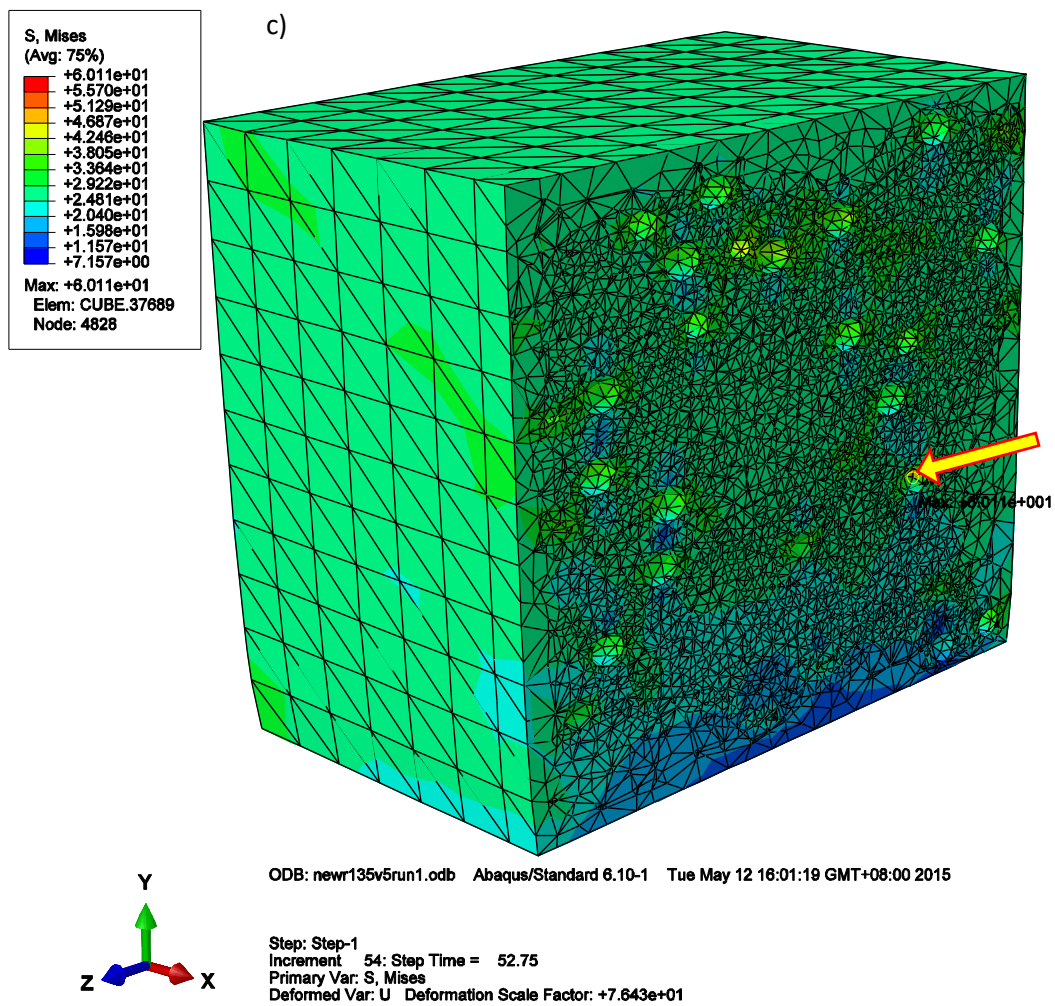
Figure 6. 6 Stress distributions for foam concrete with 5% volume fraction and *r*=1.35 mm pores; a) *t*=0s; b) *t*=120s; c) is the cross-section of stress distribution at 53s with the maximum stress value in the plane.

Stress distribution with 5% volume fraction and *r*=1.35mm pores in foam concrete is calculated in Figure 6.6. Figure 6.6 a) is initial state of foam concrete sample with stress value of 0 MPa. When it is 53s, in Figure 6.6 c) the maximum stress reaches 60.1 MPa located red arrows. At this point, these parts of the concrete sample failure because the compressive strength of a dense concrete sample is limited to 60 MPa. At 53s, the compressive strength at the red node reached 60 MPa, and for the whole sample, the effective compressive strength of foam concrete sample is given

by $f_e = 60 \times \frac{53}{120} = 26.5\,\text{MPa}$. Hence simulated compressive strength of foam concrete with radius 1.35mm and 5% volume fraction is 26.5 MPa.

(2) Volume fraction is 10%

S, Mises
(Avg: 75%)
+4.892e+01
+4.511e+01
+4.129e+01
+3.748e+01
+3.366e+01
+2.985e+01
+2.604e+01
+2.222e+01
+1.841e+01
+1.460e+01
+1.078e+01
+6.970e+00
+3.157e+00

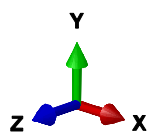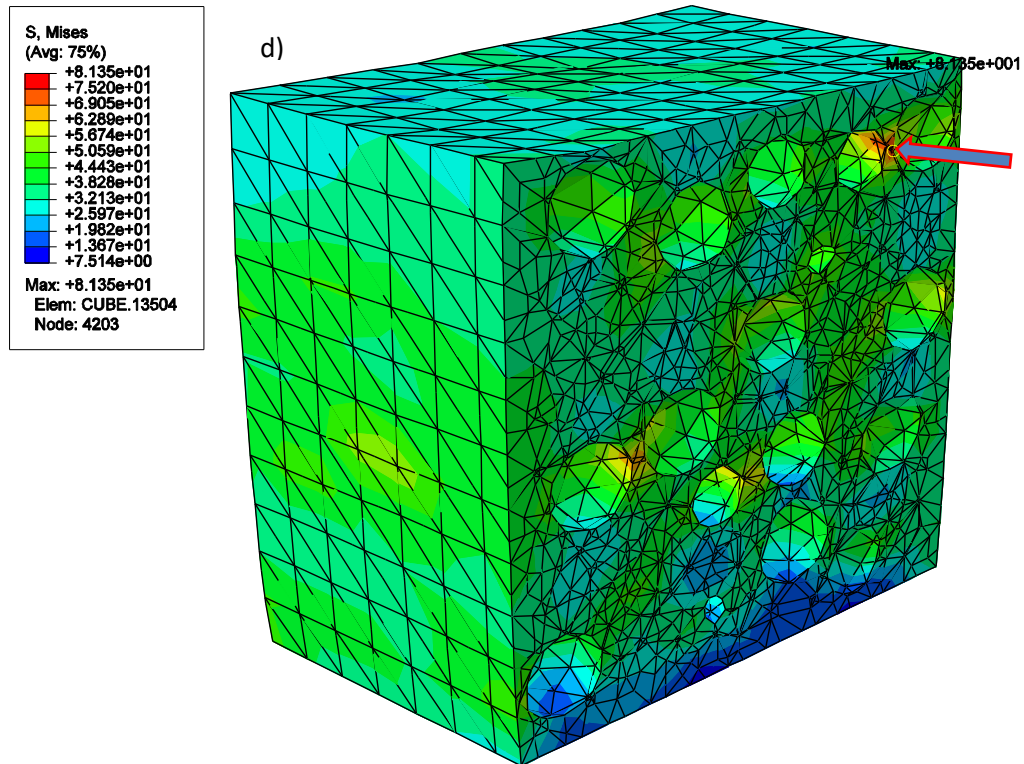Max: +4.892e+01
Elem: PART-3-1.162061
Node: 3065
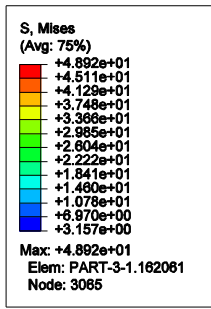
c)
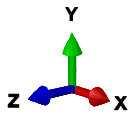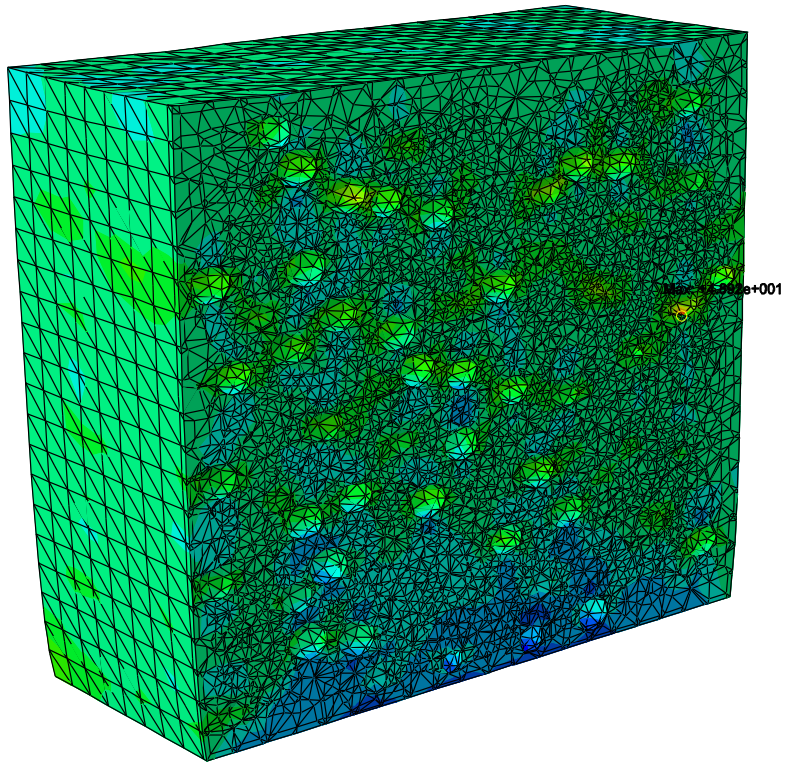
ODB: r135v10run1.odb   Abaqus/Standard 6.10-1   Mon May 11 13:19:01 GMT+08:00 2015

Step: Step-1
Increment   10: Step Time =   37.94
Primary Var: S, Mises
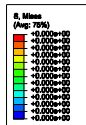Deformed Var: U   Deformation Scale Factor: +9.733e+01
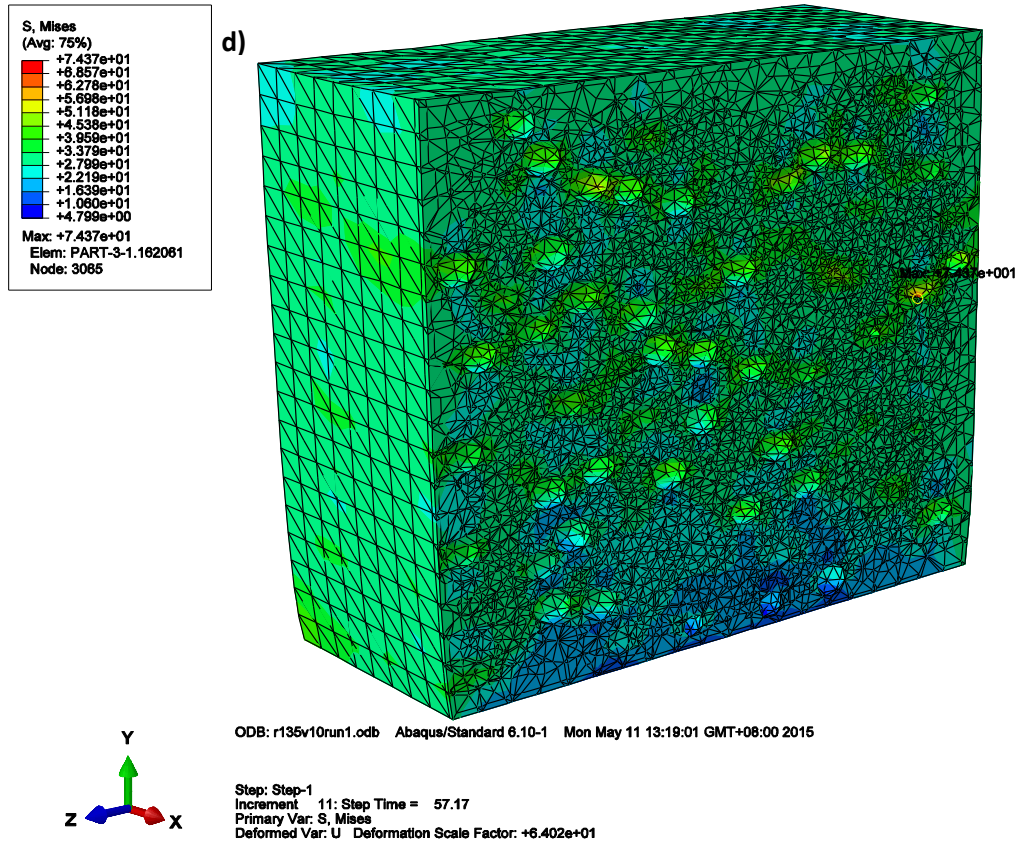
Figure 6. 7 Stress distribution for foam concrete with 10% volume fraction and *r*=1.35mm pores; a) *t*=0s; b) *t*=120s; c)-d) are the maximum stress in the cross sections at 38s and 57s.

Stress distributions of foam concrete consists of 10% volume fraction pores is shown in Figure 6.7. At beginning of test and the stress value is 0 MPa (Figure 6.7 a). When the time is 57s, as shown in figure 6.7 b), the maximum stress is 74MPa, which exceeds the dense concrete compressive strength. Figure 6.7 c) and d) are stress distributions in the maximum stress cross-section at 38s and 57s. When *t*=38s, the maximum stress in the sample is 49MPa, while at *t*=57s, the maximum stress rises to 74MPa. The maximum stress reaches 60MPa, corresponding time can be calculated by $t = 38 + (60 - 49) \times \frac{57-38}{74-49} = 46.4s$, and the effective compressive strength of the sample is given by $f_e = 60 \times \frac{46.4}{120} = 23.2$MPa.

Comparing Figure 6.7 with Figure 6.6, as the volume fraction increases, the averaged distance of neighbouring pores becomes less, which leads to a higher

possibility of stress concentration in these regions. Secondly, as the pore volume fraction increases, the maximum stress concentration value also increases. The maximum stress concentration is the position of fracturing. Furthermore, the maximum stress position in Figure 6.3-6.7 is located on the pores surface.

Comparing Figure 6.7 with Figure 6.3, it reveals that as the radius of pores decreases, the effective compressive strength of the foam concrete increases. Therefore, reducing the pore size is an effective way to enhance the compressive strength under the same volume fraction conditions. This gives a very important and quantitative principle for the manufacturing of foam concrete.

6.3 Summary

Through simulating stress distribution of foam concrete with the various volume fraction and pore sizes, the following conclusions are deduced:

1) The higher the volume fraction of pores in foam concrete, the more concentrated stress develops during loading process, thereby decreasing the effective compressive strength of foam concrete.

2) The smaller the pore size, the more uniformed the stress distributions. For the foam concrete smaller pores result in higher compressive strength than concrete containing coarser pores.

3) The inter-pore distance plays an important role in localizing the stress concentration. Smaller distance resulting in higher stress concentrations. This requires the mixing of pores or lightweight beads in foam concrete manufacturing to be homogeneous.

CHAPTER 7 THERMAL PROPERTIES OF FOAM CONCRETE

One of the advantages of foam concrete is its superior thermal insulation properties compared to normal dense concrete, which leads to its wide use in energy efficient buildings [29]. The insulation properties have raised wide researcher interests [109-111].

Thermal properties of foam concrete include heat conductivity, specific heat and the heat diffusing coefficient. The last can be expressed as a function relating heat conductivity and specific heat. As the specific heat for foam concrete is well established, the heat conductivity is the focus of research enabling an understanding of the heat transfer in foam concrete.

In this chapter, a hybrid model consisting of the mixed parallel and series concepts are used to define the heat conductivity model. Then the heat conductivity of foam concrete under the conditions of different volume fraction is predicted by the model, and its results are compared to experimentally determined heat conductivity.

One of the most serious situations leading to serious loss of life and properties is firing of building. Many researchers have investigated the fire resistance properties of building materials [112, 113]. Therefore, the developed heat conductivity model is utilized to calculate the temperature field evolution of foam concrete as a wall material and subsequently the temperature field is compared with that in dense concrete walls.

7.1 Heat Conductivity Model

Heat conductivity is an important parameter controlling heat transfer, and its determination is an important step in evaluating thermal insulation of foam concrete. In order to simulate the heat conductivity of foam concrete, the following assumptions are made:

1) Each pore is separated from others by concrete matrix, and there are no inter-connected pores in the foam concrete;

2) The pores are distributed uniformly throughout the foam concrete sample, and all pores are of the same size;

3) The pore space is fulfilled of air, in this way,the foam concrete can be regarded as an air-concrete two phases mix;

4) When the pore size is very small compared to the sample size, pores can be regarded as possessing cubic shape, an assumption that acts generation of the heat conductivity model;

Employing these assumptions, the effective heat conductivity of foam concrete can be regarded as both a mixed series heat transferring model and a parallel heat transferring model. The schematic figure of mixed heat conductivity model is depicted in Figure 7.1.
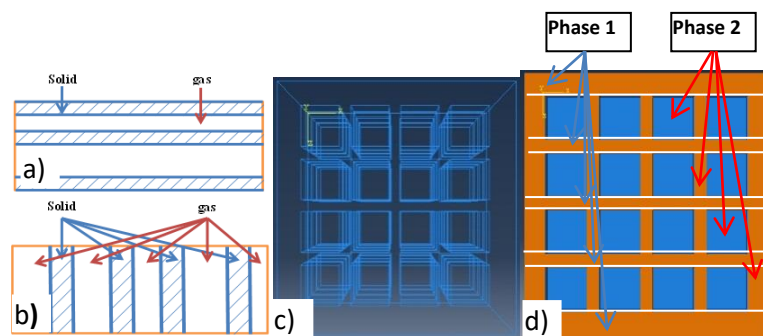
Figure 7. 1 Schematic figures for heat conductivity models, a) series model; b) parallel model; c) and d) series-parallel mixed model

In Figure 7.1, a) is a series model of heat transfer and b) is a parallel model of heat transfer; Figure 7.1 c) represents the schematic figure of cubic pores embedded in the concrete; the sample size of heat conductivity model in Figure 7.1 c) - d) is a unit cubic element ($1 \times 1 \times 1$). Figure 7.1c) represents cubic figure of air pores in solid concrete matrix. Figure 7.1 d) Phase 1 is solid phase, as marked in orange colour part, and Phase 2 is the solid/air pores one by one mixed together, in which blue colour represents air cave, and orange colour strip represents for the solid concrete body. For each Phase 2 it is regarded as a parallel heat conductivity model.

Therefore, the whole sample can be regarded as a serial heat conductivity model made up by Phase 1 and Phase 2 serially mixed together. In each Phase 2, the effective heat conductivity is calculated by the parallel heat transferring model. Then the effective heat conductivity for the whole sample can be calculated by using serial heat conductivity model combined the effective heat conductivity of Phase 2 and heat conductivity of Phase 1.

There are N^3 pores in the whole simulated zone and there is a relationship:

$$N^3 V_g^p = V_g \tag{7.1}$$

where V_g is air pore volume fraction, V_g^p is each air pore element volume,

According to Equation 7.1 each air pore volume can be expressed as:

$$V_g^p = \frac{V_g}{N^3} \tag{7.2}$$

For each length of the cubic, each pore size is expressed as:

$$l_g^p = \frac{\sqrt[3]{V_g}}{N} \tag{7.3}$$

The width of Phase l is w_1, which is expressed as:

$$w_1 = \frac{1 - \sqrt[3]{V_g}}{N+1} \tag{7.4}$$

For Figure 7.1), series heat conductivity is adopted where the Phase 1 is completely solid phase and its heat conductivity is k_s. In Phase 1, each slice area is deduced as:

$$A_1 = 1 * 1 = 1 \tag{7.5}$$

The height of A_l is

$$w_1 = \frac{1 - \sqrt[3]{V_g}}{N+1} \tag{7.6}$$

In Phase 2, the area of air phase is expressed as:

$$A_2^g = N^2 \times l_g^p \times l_g^p = N^2 \times \frac{\sqrt[3]{V_g}}{N} \frac{\sqrt[3]{V_g}}{N} = \sqrt[3]{V_g^2} \tag{7.7}$$

The area of solid phase in the Phase 2:

$$A_2^s = 1 - A_2^g = 1 - \sqrt[3]{V_g^2} \tag{7.8}$$

The height of Phase 2 is:

$$l_g^p = \frac{\sqrt[3]{V_g}}{N} \tag{7.9}$$

In the series model, the heat flux in Phase 1 and Phase 2 are the same, which is

$$q = -\frac{k_s S_1}{\Delta x_1}(T2 - T1) = -\frac{k_m S_2}{\Delta x_2}(T3 - T2) = \cdots = -\frac{k_n S_n}{\Delta x_n}(T(n+1) - Tn)$$

(7.10)

where q is the heat flux, $T(n)$ is the temperature of the nth unit, $k_n = \begin{pmatrix} k_s & n \text{ is odd number} \\ k_m & n \text{ is even number} \end{pmatrix}$, S_n is the area of the nth unit, k_m is the heat conductivity with mixed phases in Phase 2; due to the same width and length, $S_1 = S_2 = \cdots = S_n = 1$, Δx_n is the thickness of the nth unit, which is expressed as:

$$\Delta x_n = \begin{pmatrix} w_1 = \frac{1 - \sqrt[3]{V_g}}{N+1} & n \text{ is odder number} \\ l_g^p = \frac{\sqrt[3]{V_g}}{N} & n \text{ is even number} \end{pmatrix}.$$

Therefore, Equation 7.10 can be written as:

$$\frac{k_s}{\Delta x_1}(T2 - T1) = \frac{k_m}{\Delta x_2}(T3 - T2) = \cdots = \frac{k_n}{\Delta x_n}(T(n+1) - Tn) = -\frac{k_e}{1}(Tn - T1) = \frac{q}{A_1} \tag{7.11}$$

where k_e is the effective heat conductivity of foam concrete;

In the Phase 2, regardless of solid or gas phase, temperature gradient under equilibrium status between each input side and output side is the same.

$$(T3 - T2) = (T5 - T4) = \cdots = -\frac{q\Delta x_2}{1 * k_m} = -\frac{q l_g^p}{1 * k_m} = -\frac{q}{k_m}\frac{\sqrt[3]{V_g}}{N} \tag{7.12}$$

In each Phase 2, there are N^2 air pores, which can be regarded as parallel mode of heat transfer:

$$-\frac{k_g * l_g^p * l_g^p}{l_g^p}(T3 - T2)N^2 - \frac{k_s * w_1 * l_g^p}{l_g^p}(T3 - T2) \cdot 2N(N+1)$$

$$-\frac{k_s * w_1^2}{l_g^p}(T3 - T2)(N + 1)^2 = -\frac{k_m * A1}{l_g^p}(T3 - T2) \tag{7.13}$$

Equation 7.13 can be simplified as:

$$\frac{k_g * (l_g^p)^2}{l_g^p} * N^2 + \frac{k_s * w_1 * l_g^p}{l_g^p} * 2 * N(N + 1) + \frac{k_s * w_1^2}{l_g^p} * (N + 1)^2 = \frac{k_m * 1}{l_g^p} \tag{7.14}$$

Equation 7.14 is simplified as:

$$k_m = k_g \sqrt[3]{V_g^2} + 2k_s\left(1 - \sqrt[3]{V_g}\right)\sqrt[3]{V_g} + k_s\left(1 - \sqrt[3]{V_g}\right)^2 = k_g \sqrt[3]{V_g^2} + k_s(1 - \sqrt[3]{V_g^2}) \tag{7.15}$$

According to Equation 7.11 and Equation 7.12, following relationship is obtained:

$$\begin{cases} (T2 - T1) = (T4 - T3) = \cdots = -\frac{q}{k_s}w_1 \\ (T3 - T2) = (T5 - T4) = \cdots = -\frac{q}{k_m}l_g^p \end{cases} \tag{7.16}$$

Equation 7.16 can be transformed into:

$$(T2 - T1) + (T3 - T2) + \cdots + (T(n + 1) - Tn) =$$

$$-\frac{q}{k_s}w_1 * (N + 1) - \frac{q}{k_m}l_g^p * N = Tn - T1 = -\frac{q}{k_e} \tag{7.17}$$

Equation 7.17 can be rewritten as:

$$\frac{1}{k_e} = \frac{(1 - \sqrt[3]{V_g})}{k_s} + \frac{\sqrt[3]{V_g}}{k_m}. \tag{7.18}$$

Incorporating Equation 7.15 into Equation 7.18, the effective heat conductivity by series model is obtained:

$$k_e = \frac{k_s k_m}{(1 - \sqrt[3]{V_g})k_m + \sqrt[3]{V_g}k_s} = k_s \frac{k_g\sqrt[3]{V_g^2} + k_s\left(1 - \sqrt[3]{V_g^2}\right)}{k_g\left(\sqrt[3]{V_g^2} - V_g\right) + k_s\left(1 - \sqrt[3]{V_g^2} + V_g\right)} \tag{7.19}$$

According to Equation 7.19, the effective heat conductivity is obtained by means of series dominated model, and the results of the effective heat conductivity by the model and experimental method are listed in Table 7.1. Note that the heat conductivity of air is 0.024 W/m·K at room temperature[46].

Table 7. 1 Experimental and calculated effective heat conductivity of foam concrete*

Group No.	Density (kg/m^3)	Experimental heat conductivity (W/m·K)	Calculated value (W/m·K)	relative error(%)
1	1373	0.369	0.369	0
2	1194	0.325	0.318	2.2
3	902	0.239	0.232	3.1
4	817	0.217	0.208	4.3
5	761	0.185	0.192	4.0
6	608	0.162	0.152	6.0
7	580	0.142	0.145	2.3

*Experimental data is provided by Zuhua Zhang [93]

The heat conductivity are reported in Table 7.1, together with calculated volume fraction and the proposed method for different densities, for which there are seven density groups of foam concrete ranging from 580 kg/m^3 to 1373 kg/m^3. The first group density 1373 kg/m^3 is used as the initial value, for which no foam is added into concrete. Comparison of the calculated results with the experimental results reveals that the maximum relative error for heat conductivity is less than 6%.
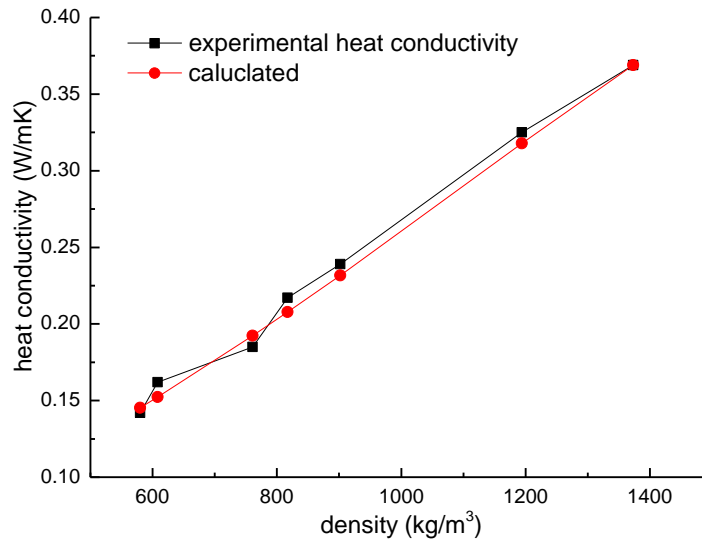
Figure 7. 2 A comparison of the calculated and experimentally measured heat conductivities

Theoretically calculated and experimentally measured heat conductivities for foam concrete with different densities is evident in Figure 7.2. Here the black squares represent experimentally measured heat conductivity and red circles represent theoretically calculated heat conductivities. The difference between the theoretically calculated heat conductivity and experimentally measured heat conductivity is very small.
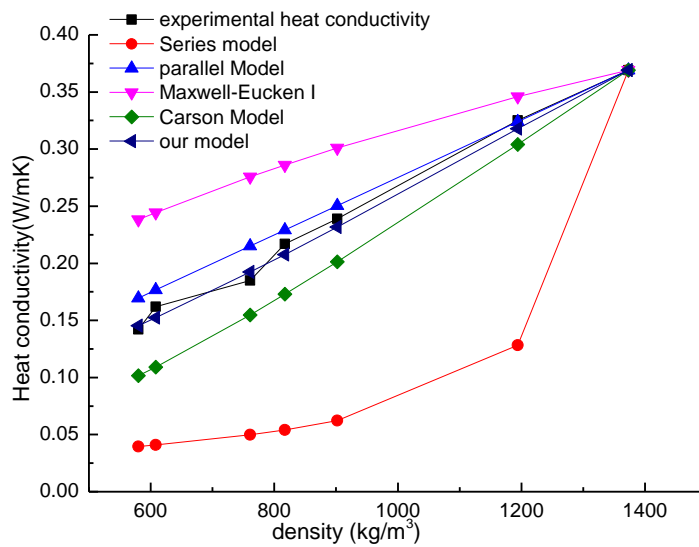
Figure 7. 3 Comparison among the heat conductivity by different models

In contrast, Figure 7.3 is a plot of the heat conductivity values predicted by different theoretical models and the obtained experimentally. The effective heat conductivity by our proposed model closer to the experimental results than that by series model, parallel model, Maxwell-Eucken I model and Carson model models. It proves that the proposed effective heat conductivity model is more reliable for predicting the effective heat conductivity of foam concrete.

7.2 Temperature Evolution during A Fire Incident

Building fire incidents are the most threat to the human lives in buildings, and the fire-resistance material in building walls and other parts are very important to protect human from life threat [114, 115]. As a kind of light weight thermal insulation material, foam concrete is regarded as an ideal fire resistance construction material for its lower heat conductivity and non-combustible properties [1, 3].

In this part, temperature fields in a traditional concrete wall and a foam concrete wall during a fire incident are simulated and compared. The temperature field evolution is used to quantitatively describe the thermal insulation properties of foam concrete.

According to Ref [116], the effective specific heat of foamed concrete is expressed as:

$$C_p = C_p^a m_a + C_p^c (1 - m_a) \tag{7.20}$$

where m_a is the mass fraction of the foam, which can be calculated as $m_a = \rho_a \times V_g / [\rho_a \times V_g + \rho_c \times (1 - V_g)]$. For 580 kg/m^3 foamed concrete, $m_a = 0.0012$. C_p^a is the specific heat of air, which is 1005 J/kg·K [117]. C_p^c is specific heat of the concrete matrix, which is 967 J/kg·K. So the effective specific heat of the foamed concrete is: $C_p = 967.05$ J/kg·K. Comparing with the experimental value 920 J/kg·K of foam concrete, the relative error is only 5.1%.

$$\rho = \rho_c (1 - V_g) + V_g \rho_a \tag{7.21}$$

where ρ_c is the concrete density, ρ_a is the air density in the pores.

The heat transfer in foamed concrete wall is expressed as:

$$\frac{\partial T}{\partial t} = \alpha \nabla^2(T) \tag{7.22}$$

where T is temperature ($\mathrm{°C}$); t is time (s); α is thermal diffusivity (m^2/s), which can be expressed as $\alpha = \frac{k_e}{\rho C_p}$, where k_e is the thermal conductivity from Equation 7.19, ρ is the density from Equation 7.21 and C_p is derived from Equation 7.20.

When there is a fire outside the wall, the temperature rising curve for such a fire incident is given as a function of firing time[118]:

$$T_f = 20 + 345\ln(1 + 8t) \tag{7.23}$$

At the beginning of a fire incident, the initial temperature of the wall (both external and internal) is set $T_0 = 20$ $\mathrm{°C}$. A typical fire temperature rising curve is drawn in Figure 7.4.
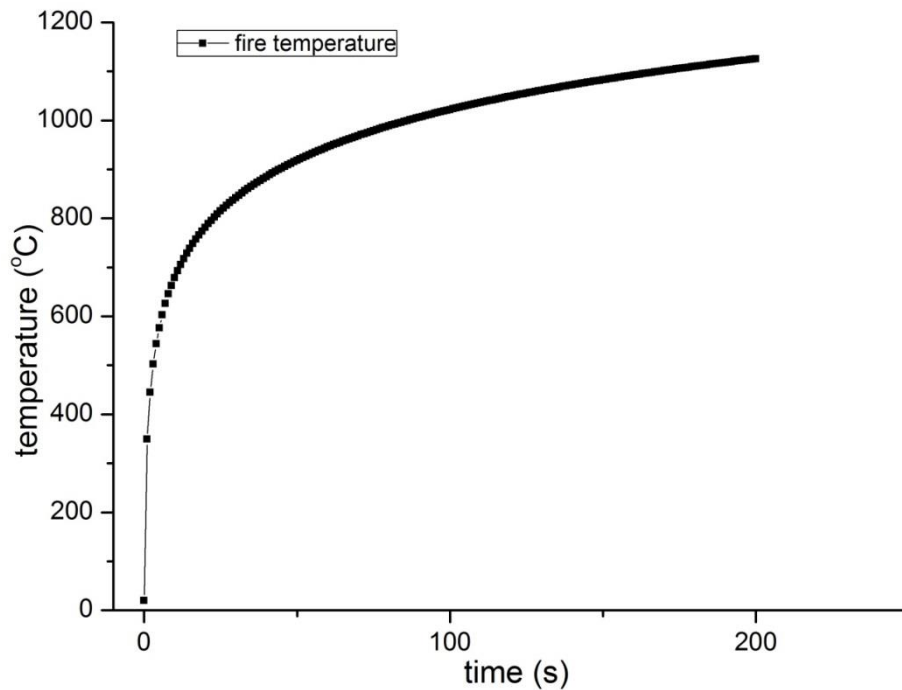
Figure 7. 4 A typical fire temperature versus time curve [111]

On the external of the wall, convection is applied:

$$\frac{\partial T}{\partial t} = -h_o(T_3 - T_f) \tag{7.24}$$

where h_o is the interface heat transfer coefficient between the fire surroundings and the outside wall surface; T_3 and T_f are fire surrounding temperature and outside wall surface temperature, respectively.

On the internal of the wall, the same convection and radiation heat transfer equation is applied:

$$\frac{\partial T}{\partial t} = -h_i(T_2 - T_1) \qquad q = \epsilon_1 \sigma A_1(T_1^4 - T_2^4) \tag{7.25}$$

where h_i is the interface heat transfer coefficient between the inside wall surface and inside of the room surrounding; T_2 and T_1 are the temperature inside the room surrounding (20 ℃) and inside wall surface, respectively; ϵ_1 is grey body emission coefficient, and its value is 0.63 [117]; σ is Stefan-Boltzmann constant, which is 5.669×10^{-8} W/m^2 ·K; and A_1 is the area of emissive zone (m^2).

In order to enhance calculation efficiency and to reduce computing time, a 30 mm wall thickness is adopted and the wall section has a length and width of 10 mm. The length and width directions are set as periodic boundary conditions, which indicates that there is no heat transference except inside and outside directions of the wall (Refer to Figure 7.5). The temperature field for a dense concrete wall under the same conditions is also calculated. The density, heat conductivity and specific heat of the dense concrete are 2300 kg/m^3, 1.8 W/m ·K and 912 J/kg ·K respectively. The meshed size is 1mm, and the wall is meshed into 3000 cubic units. The schematic figure and meshed shape are depicted in Figure 7.5.
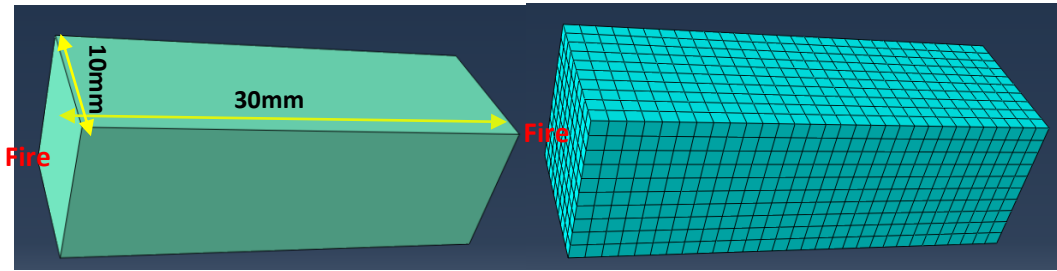
Figure 7. 5 Schematic figure of wall and its meshed figure
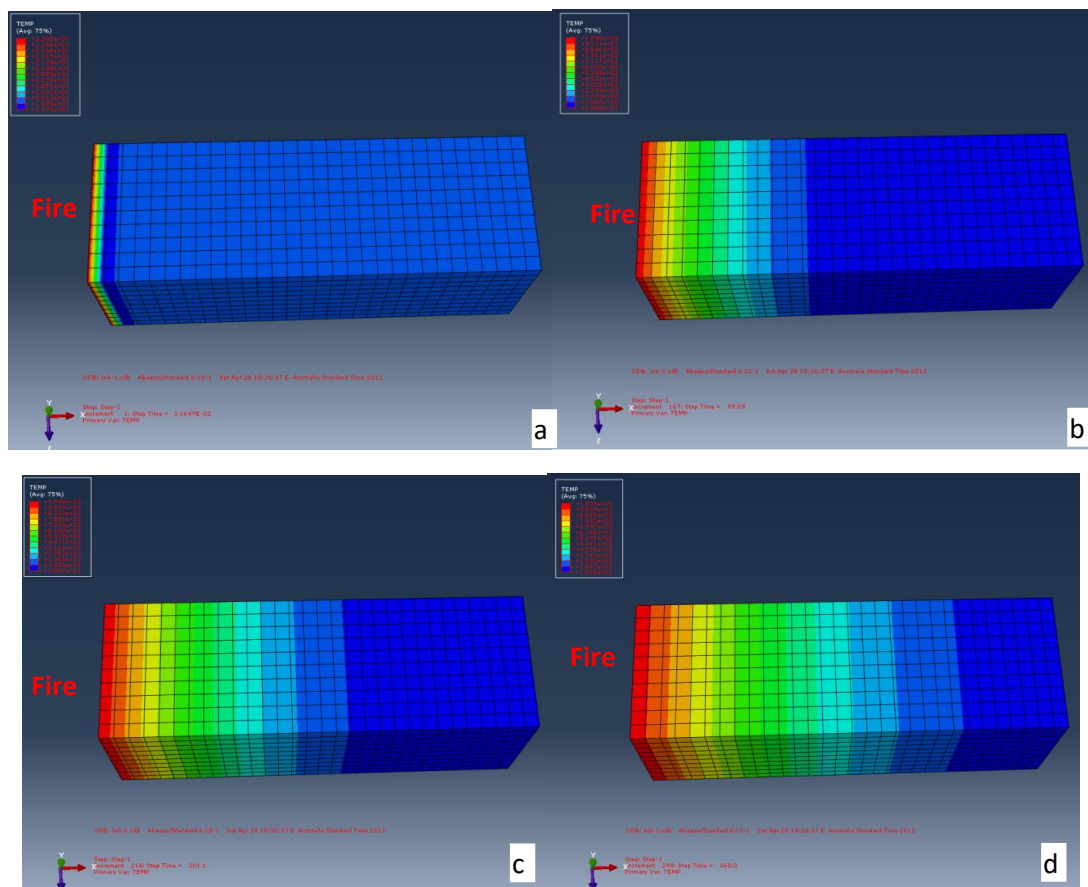
Figure 7. 6 Simulated temperature field of foamed concrete at different times,
(a) 0.03 s; (b) 100 s; (c) 200 s and (d) 360 s

The temperature field in the foamed concrete wall at 0.03 s, 99 s, 200 s and 360 s are calculated and showed in Figure 7.6. The colours in each Figure 7.6 are indicating different temperature values. At 0.03 s, in Figure 7.6a, only the end touching fire rises temperature from initial 20 ℃ to 22 ℃. When it is 100 s, in Figure 7.6b, the temperature of the outside wall surface rises rapidly to 1045 ℃, and

temperature elevated zone extends to the 11th meshed grid. And there are still 19 mm of the wall keeping its temperature at 20 ℃. After 200 s, the fire stops as shown in Figure 7.6c), and the maximum temperature is 1058 ℃. In Figure 7.6 d, the highest temperature drops to 1039 ℃ at 360 s and 7 mm of wall still remains at temperature of 20 ℃.
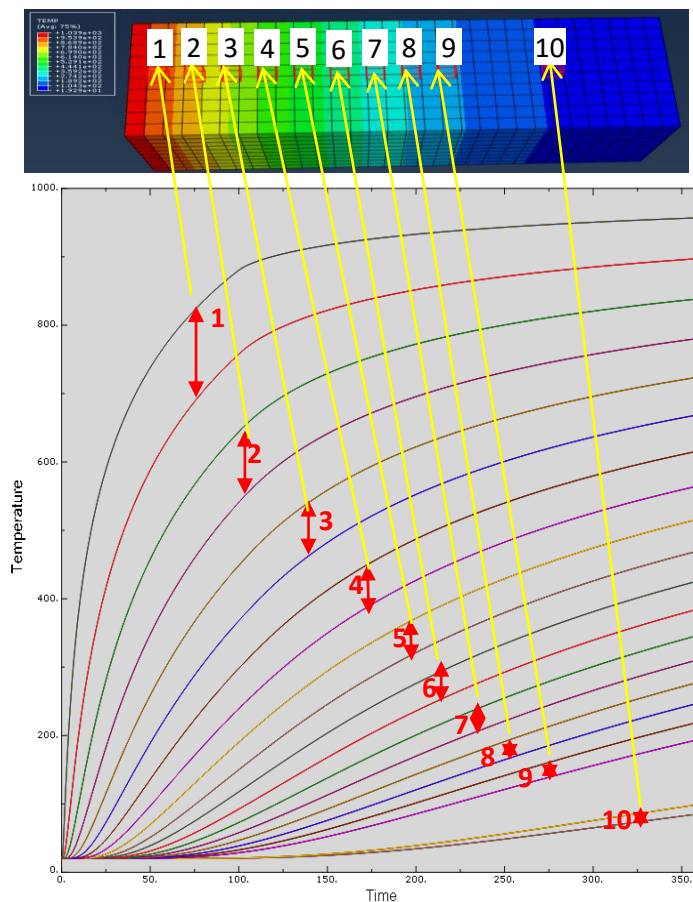
Figure 7. 7 Simulated temperature evolution curves for selected units during a fire incident

The simulated temperature rising curve for the 10 selected units of foamed concrete are shown in Figure 7.7. From the left side of wall, the temperature evolution curve of the first unit is drawn in the top two curves, one is adjacent to fire face, the other is far from the fire face. The temperature rises quickly from 0 to 50 s, and then rises slowly. The final temperature difference between the two curves is less than 50 ℃. As the unit is 1 mm in size, therefore the temperature gradient is 50 ℃/mm at 360 s for the first unit. For other units further away from the external fire, their

temperature difference decreases gradually. For the last selected unit, the temperature difference between the two sides of the unit is 20 ℃ at 360 s.
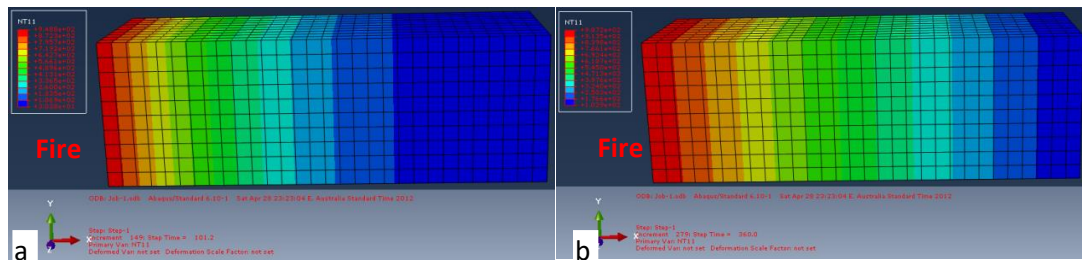
Figure 7. 8 Calculated temperature field for a solid concrete wall at varying time periods; a) t=100s;b) t=360s

The temperature field of traditional dense concrete wall at 100 s and 360 s are calculated in Figure 7.8. At 100 s (Figure 7.8 a), the highest temperature and the lowest temperature are 948 ℃ and 30 ℃, respectively, located adjacent to the wall surface of the fire side wall and the other end. At 360 s (Figure 7.8b), the highest and lowest temperature are 987 ℃ and 102 ℃, respectively, which means that the entire wall temperature exceeds 100 ℃. Comparing with foamed concrete (in Figure 7.8d), the temperature field of the conventional concrete wall rises more rapidly.

The temperature evolution curves for different positions within a normal dense concrete structure are shown in Figure 7.9, in which six nodes along the wall thickness are chosen to viewing their temperature evolution during a fire accident. From the left face, the temperature of node 1 rises quickly up to 700℃ in less than 50s, follows by a gradually rise to 800℃ at 100s; beyond 100s the temperature increases more slowly than before, and at 360s the first node temperature reaches 900℃. The temperature of the second node rises quickly before 100s and up to 700℃ at 360s. The last node is only 3mm from the right side face of wall and its temperature rises gradually and reaches 180℃ at 360s.
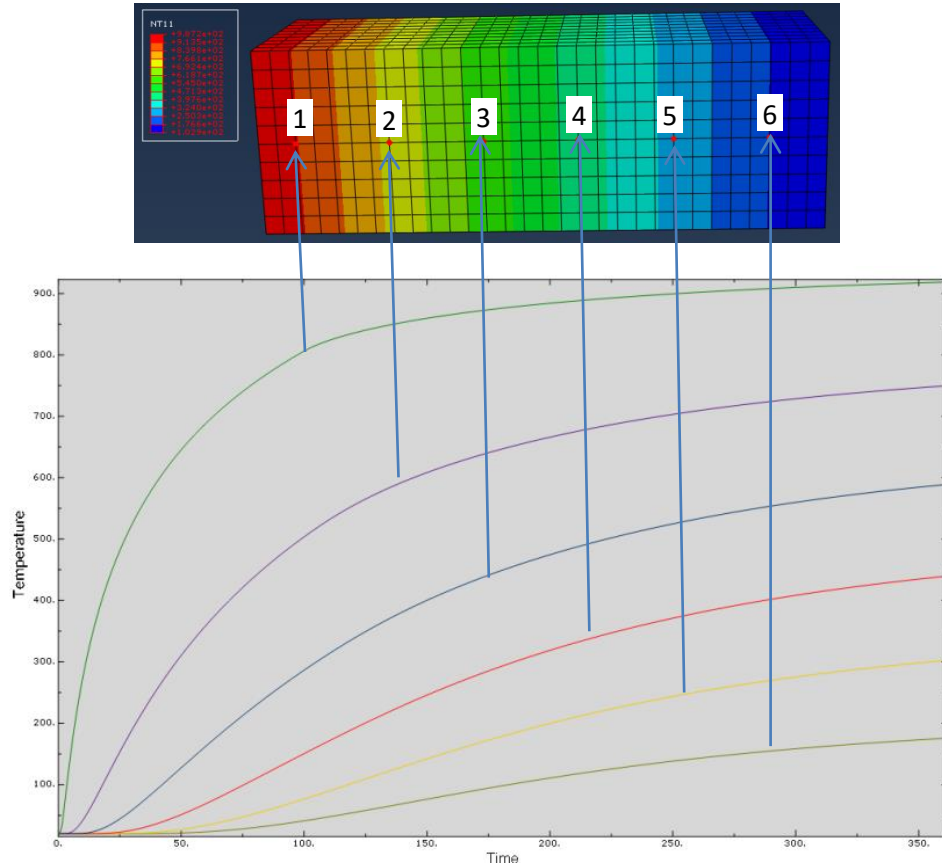
Figure 7. 9 Temperature evolution curve of the marked point

7.3 Summary

By establishing the relationships between volume fraction, heat conductivity and the specific heat model, temperatures field of foam concrete during a simulated fire accident can be simulated, the following conclusions are achieved:

1. The effective heat conductivity of foam concrete is: $k_e = k_s \dfrac{k_g\sqrt[3]{V_g^2}+k_s\left(1-\sqrt[3]{V_g^2}\right)}{k_g\left(\sqrt[3]{V_g^2}-\varepsilon\right)+k_s\left(1-\sqrt[3]{V_g^2}+V_g\right)}$; with a relative error of less than 6%.

2. The effective specific heat of foam concrete is $C_p^e = C_p^a m_a + C_p^c (1 - m_a)$; the specific heat for $\rho = 580\text{kg/m}^3$ is $C_p^e = 967.05$ J/kg•K while experimental value is 920 J/kg•K, and the relative error is less than 5.1%.

3. For a 30mm thickness foam concrete wall, temperature is maintained at 20℃ on the opposite side for 360s of firing on one side. The wall thickness of 7 mm maintains at this temperature. In contrast, temperature for a simulated dense concrete wall rises to more than 150℃ after the same period of firing. Therefore, foam concrete can allow people to have more time to escape from a fire incident than a traditional dense concrete wall.

CHAPTER 8 CONCLUSIONS

In this thesis, the main two physical properties—compressive strength and heat conductivity of foam concrete are studied by experimental, theoretical and numerical simulation methods, which provides a tool to design foam concrete and predict the final product properties. Firstly, the aims of this research are presented in introduction chapter. Then, research progress of foam concrete is reviewed in chapter 2. In chapter 3, experimental method is employed to build the relationship between pore features and compressive strength. In chapter 4, theoretical method is employed to deduce compressive strength with single size and two sizes of EPS concretes. In chapter 5, EPS beads distribution in 2D and 3D is simulated by using Matlab and Python program. Following, finite element method is employed to simulate the compressive strength. Finally, the heat conductivity of foam concrete is deduced by theoretical method, and the fire resistance of foam concrete wall is simulated by using this theoretically calculated heat conductivity.

By completing the research work designed in this thesis, the following important conclusions are drawn:

1) The compressive strength of EPS concrete containing 2.68 mm diameter EPS is $f_{2.68} = 5.57756 \times 10^{-8} \times \rho^{2.71984}$ (MPa). The compressive strength of EPS concrete with 7.04mm diameter EPS is $f_7 = 3.19781 \times 10^{-9} \times \rho^{3.07017}$ (MPa);

2) The smaller the size of EPS beads in EPS concrete is, the smaller difference between the experimental measurement and theoretical calculation. Low the volume fraction of EPS beads in EPS concrete leads to consistence between the experimental measurement and theoretical calculation\;

3) Through numerically fitting, the relationship between compressive strength and pore volume fraction of foam concrete can be expressed as: $f = 49.00164 - 54.10444 * (1 - e^{(-V_f/0.31316)})$;

4) Pores size distribution in foam concrete is described as: $y(V_f, x) = \exp(A + B \cdot x) = \exp\left(0.69 - 0.65 \exp\left(-\exp\left(-\frac{V_f - 0.41}{0.14}\right) - \frac{V_f - 0.41}{0.14} + 1\right) + \left(-0.0081 - \right.\right.$

$0.01646V_f + 0.11353V_f{}^2 - 0.13863V_f{}^3)x\Big)$; pore averaged sizes are

$\overline{l(V_f)} = 115.81 + 26.97V_f + 16.49V_f{}^2 + 3010.26V_f{}^3 - 4565.42V_f{}^4$; the pores

area fraction is expressed as: $\overline{s(V_f)} = 0.065 + 1.27V_f - 7.40V_f{}^2 + 26.97V_f{}^3 - 25.98V_f{}^4$; the compressive strength of foam concrete is deduced to be:

$\sigma = 3.5 + 11.25 * \left(1 + erf\left(\frac{\overline{l} - 158.46}{39.05\sqrt{2}}\right)\right) * \left(1 + erf\left(\frac{\overline{s} - 0.38}{0.30\sqrt{2}}\right)\right)$;

5) Theoretically, for the EPS concrete containing only single sized EPS beads, the compressive strength can be expressed as: $f_c = f_0(1 - \dfrac{fix\left(\frac{3V_f a^3}{4\pi r^3}\right)\pi r^2}{a^2})$; if two sizes of EPS beads are mixed in the concrete matrix, the maximum compressive strength can be achieved when the volume fraction of two sizes EPS beads is 50:50. The maximum compressive strength of two sized EPS beads mixed in EPS concrete is $f = f_0(1 - S) = f_0\left(1 - 2\pi\left(\frac{3V_f}{8\pi}\right)^{\frac{2}{3}}\right)$. Comparing with only single size EPS beads embedded in concrete, the maximum compressive strength with the two sizes of EPS beads is lower;

6) A Matlab program is compiled to describe the EPS distribution in a concrete matrix, and the EPS beads distribution is compared with experimental samples, the results confirms that the program can be adopted for description the EPS beads distribution;

7) Through the numerical simulation, it is established that the distance between the neighbouring pores plays an important role in determining the local maximum stress. In addition, the smaller the diameter of pores reduces the stress concentration;

8) The heat conductivity of foam concrete is expressed as:

$k_e = k_s \dfrac{k_g\sqrt[3]{V_g{}^2} + k_s\left(1 - \sqrt[3]{V_g{}^2}\right)}{k_g\left(\sqrt[3]{V_g{}^2} - V_g\right) + k_s\left(1 - \sqrt[3]{V_g{}^2} + V_g\right)}$. A comparison of the calculated results with

experimental measured results, the relative error is less than 6%. By using this model, the temperature field during a fire incident is further compared with

traditional dense concrete, and the simulation results confirm the superior thermal insulation property.

Future Research Plan

After completing the work in this thesis, the author finds that there are still lots of work remains to be done in the future.

First of all, optimizing the foam concrete pore features so as to get the premium thermal insulation and compressive strength is the most important thing for the future study, which includes balance between the heat conductivity and compressive strength to match the engineering requirement.

Secondly, in this thesis only the influences of volume fraction and pore size on compressive strength are studied. In the future, the pore shape factor and pores' average distance can be studied, which is helpful to deeply understand its effect on the compressive strength of foam concrete.

Finally, by controlling pore features during the foam concrete making process, the idealized pore features can be obtained, which will be directly beneficial to the industries.

References

1.   Ramamurthy, K., E.K. Kunhanandan Nambiar, and G. Indu Siva Ranjani, *A classification of studies on properties of foam concrete.* Cement and Concrete Composites, 2009. **31**(6): p. 388-396.

2.   Qu, X. and X. Zhao, *Previous and present investigations on the components, microstructure and main properties of autoclaved aerated concrete – A review.* Construction and Building Materials, 2017. **135**: p. 505-516.

3.   Hlaváček, P., et al., *Inorganic foams made from alkali-activated fly ash: Mechanical, chemical and physical properties.* Journal of the European Ceramic Society, 2015. **35**(2): p. 703-709.

4.   Amran, Y.H.M., N. Farzadnia, and A.A. Abang Ali, *Properties and applications of foamed concrete; a review.* Construction and Building Materials, 2015. **101**: p. 990-1005.

5.   Zhang, Z., et al., *Mechanical, thermal insulation, thermal resistance and acoustic absorption properties of geopolymer foam concrete.* Cement and Concrete Composites, 2015. **62**: p. 97-105.

6.   Huang, Z., T. Zhang, and Z. Wen, *Proportioning and characterization of Portland cement-based ultra-lightweight foam concretes.* Construction and Building Materials, 2015. **79**: p. 390-396.

7.   Nambiar, E.K.K. and K. Ramamurthy, *Models for strength prediction of foam concrete.* Materials and Structures, 2007. **41**(2): p. 247-254.

8.   Batool, F. and V. Bindiganavile, *Air-void size distribution of cement based foam and its effect on thermal conductivity.* Construction and Building Materials, 2017. **149**: p. 17-28.

9.   Kumar, R. and B. Bhattacharjee, *Porosity, pore size distribution and in situ strength of concrete.* Cement and Concrete Research, 2003. **33**(1): p. 155-164.

10.   Kearsley, E.P. and P.J. Wainwright, *The effect of porosity on the strength of foamed concrete.* Cement and Concrete Research, 2002. **32**(2): p. 233-239.

11.   Narayanan, N. and K. Ramamurthy, *Structure and properties of aerated concrete: a review.* Cement and Concrete Composites, 2000. **22**(5): p. 321-329.

12.   Miled, K. and O. Limam, *Effective thermal conductivity of foam concretes: Homogenization schemes vs experimental data and FEM simulations.* Mechanics Research Communications, 2016. **76**: p. 96-100.

13.   Lian, C., Y. Zhuge, and S. Beecham, *The relationship between porosity and strength for porous concrete.* Construction and Building Materials, 2011. **25**(11): p. 4294-4298.

14.   Sumanasooriya, M.S. and N. Neithalath, *Pore structure features of pervious concretes proportioned for desired porosities and their performance prediction.* Cement and Concrete Composites, 2011. **33**(8): p. 778-787.

15.   Nambiar, E.K.K. and K. Ramamurthy, *Air‐void characterisation of foam concrete.* Cement and Concrete Research, 2007. **37**(2): p. 221-230.

16.   Deo, O. and N. Neithalath, *Compressive behavior of pervious concretes and a quantification of the influence of random pore structure features.* Materials Science and Engineering: A, 2010. **528**(1): p. 402-412.

17.   Wikipedia. *Concrete*. 2012; Available from: http://en.wikipedia.org/wiki/Concrete.

18.   Arellano Aguilar, R., O. Burciaga Díaz, and J.I. Escalante García, *Lightweight concretes of activated metakaolin-fly ash binders, with blast furnace slag aggregates.* Construction and Building Materials, 2010. **24**(7): p. 1166-1175.

19. *Concrete Properties--Properties of normal strength Portland cement concrete*. 2012; Available from: http://www.engineeringtoolbox.com/concrete-properties-d_1223.html.

20. Roberts, B. *Global cement consumption up to 9.9% last year*. 2011; Available from: http://www.constructionweekonline.com/article-11772-global-cement-consumption-up-99-last-year/.

21. Vanderley M.John, E.P., *On the sustainability of concrete.* UNEP Industry and Environment, 2003: p. 1-7.

22. Pade, C. and M. Guimaraes, *The CO2 uptake of concrete in a 100 year perspective.* Cement and Concrete Research, 2007. **37**(9): p. 1348-1356.

23. Ramli, A.O.R.M.B., *A Qualitative Study of Green Building Indexes Rating of Lightweight Foam Concrete.* Journal of Sustainable Development, 2011. **4**(5): p. 188-195.

24. Saber, H.H., et al., *3D heat and air transport model for predicting the thermal resistances of insulated wall assemblies.* Journal of Building Performance Simulation, 2011. **5**(2): p. 75-91.

25. Wei, S., et al., *Characterization and simulation of microstructure and thermal properties of foamed concrete.* Construction and Building Materials, 2013. **47**(0): p. 1278-1291.

26. Hung, T.-C., et al., *Inorganic polymeric foam as a sound absorbing and insulating material.* Construction and Building Materials, 2014. **50**(0): p. 328-334.

27. Wikipedia. *Autoclaved aerated concrete*. 2012; Available from: http://en.wikipedia.org/wiki/Autoclaved_aerated_concrete.

28. Just, A. and B. Middendorf, *Microstructure of high-strength foam concrete.* Materials Characterization, 2009. **60**(7): p. 741-748.

29. Zhang, Z., et al., *Geopolymer foam concrete: An emerging material for sustainable construction.* Construction and Building Materials, 2014. **56**(0): p. 113-127.

30. Petersen, A.K. and B. Solberg, *Environmental and economic impacts of substitution between wood products and alternative materials: a review of micro-level analyses from Norway and Sweden.* Forest Policy and Economics, 2005. **7**(3): p. 249-259.

31. Nooraini Mohd Zahari, I.A.R.a.A.M.A.Z., *foam concrete potential application in thermal insulation*, in *Proceedings of MUCEET2009*. 2009: MS Garden, Kuantan, Pahang, Malaysia. p. 47-52.

32. Al-Jabri, K.S., et al., *Concrete blocks for thermal insulation in hot climate.* Cement and Concrete Research, 2005. **35**(8): p. 1472-1479.

33. Liu, M.Y.J., et al., *Evaluation of thermal conductivity, mechanical and transport properties of lightweight aggregate foamed geopolymer concrete.* Energy and Buildings, 2014. **72**(0): p. 238-245.

34. Ortiz, O., F. Castells, and G. Sonnemann, *Sustainability in the construction industry: A review of recent developments based on LCA.* Construction and Building Materials, 2009. **23**(1): p. 28-39.

35. Pisello, A.L., et al., *Effect of dynamic characteristics of building envelope on thermal-energy performance in winter conditions: In field experiment.* Energy and Buildings, 2014. **80**(0): p. 218-230.

36. Huber, P., et al., *Conditions for cost-efficient reuse of biological sludge for paper and board manufacturing.* Journal of Cleaner Production, 2014. **66**(0): p. 65-74.

37. Demirboğa, R. and R. Gül, *The effects of expanded perlite aggregate, silica fume and fly ash on the thermal conductivity of lightweight concrete.* Cement and Concrete Research, 2003. **33**(5): p. 723-727.

38. Ahmaruzzaman, M., *A review on the utilization of fly ash.* Progress in Energy and Combustion Science, 2010. **36**(3): p. 327-363.

39. Nambiar, E.K.K. and K. Ramamurthy, *Models relating mixture composition to the density and strength of foam concrete using response surface methodology.* Cement and Concrete Composites, 2006. **28**(9): p. 752-760.

40. Limbachiya, M., M.S. Meddah, and Y. Ouchagour, *Use of recycled concrete aggregate in fly-ash concrete.* Construction and Building Materials, 2012. **27**(1): p. 439-449.

41. Duxson, P., et al., *The role of inorganic polymer technology in the development of 'green concrete'.* Cement and Concrete Research, 2007. **37**(12): p. 1590-1597.

42. Bernal, S.A., et al., *Evolution of binder structure in sodium silicate-activated slag-metakaolin blends.* Cement and Concrete Composites, 2011. **33**(1): p. 46-54.

43. Henon, J., et al., *Porosity control of cold consolidated geomaterial foam: Temperature effect.* Ceramics International, 2012. **38**(1): p. 77-84.

44. Al-Sibahy, A. and R. Edwards, *Thermal behaviour of novel lightweight concrete at ambient and elevated temperatures: Experimental, modelling and parametric studies.* Construction and Building Materials, 2012. **31**: p. 174-187.

45. Al-Sibahy, A. and R. Edwards, *Mechanical and thermal properties of novel lightweight concrete mixtures containing recycled glass and metakaolin.* Construction and Building Materials, 2012. **31**: p. 157-167.

46. Wongkeo, W., et al., *Compressive strength, flexural strength and thermal conductivity of autoclaved concrete block made using bottom ash as cement replacement materials.* Materials and Design, 2012. **35**(0): p. 434-439.

47. Ünal, O., T. Uygunoğlu, and A. Yildiz, *Investigation of properties of low-strength lightweight concrete for thermal insulation.* Building and Environment, 2007. **42**(2): p. 584-590.

48. Mo, L.T., et al., *2D and 3D meso-scale finite element models for ravelling analysis of porous asphalt concrete.* Finite Elements in Analysis and Design, 2008. **44**(4): p. 186-196.

49. Brocca, M., Z.P. Bažant, and I.M. Daniel, *Microplane model for stiff foams and finite element analysis of sandwich failure by core indentation.* International Journal of Solids and Structures, 2001. **38**(44–45): p. 8111-8132.

50. Ehlers, W. and W. Volk, *On theoretical and numerical methods in the theory of porous media based on polar and non-polar elasto-plastic solid materials.* International Journal of Solids and Structures, 1998. **35**(34–35): p. 4597-4617.

51. Benboudjema, F., F. Meftah, and J.M. Torrenti, *Interaction between drying, shrinkage, creep and cracking phenomena in concrete.* Engineering Structures, 2005. **27**(2): p. 239-250.

52. Ranaivomanana, N., S. Multon, and A. Turatsinze, *Basic creep of concrete under compression, tension and bending.* Construction and Building Materials, 2013. **38**(0): p. 173-180.

53. Chindaprasirt, P. and U. Rattanasak, *Shrinkage behavior of structural foam lightweight concrete containing glycol compounds and fly ash.* Materials & Design, 2011. **32**(2): p. 723-727.

54. Duxson, P., G.C. Lukey, and J.S.J. van Deventer, *Thermal evolution of metakaolin geopolymers: Part 1 – Physical evolution.* Journal of Non-Crystalline Solids, 2006. **352**(52-54): p. 5541-5555.

55. S.M.Abd, M.F.M.Z., R.Abdul Hamid, *Modeling the prediction of compressive strength for cements and foam concrete*. 2008. p. 343-354.

56.   Nambiar, E.K.K. and K. Ramamurthy, *Models for strength prediction of foam concrete.* Materials and Structures, 2008. **41**(2): p. 247-254.

57.   Narayanan, K.R.a.N., *Factors influencing the density and compressive strength of aerated concrete.* Magazine of Concrete Research, 2000. **52**(3): p. 6.

58.   Hoff, G.C., *Porosity-strength considerations for cellular concrete.* Cement and Concrete Research, 1972. **2**(1): p. 91-100.

59.   Ashby, L.J.G.a.M.F., *The Mechanics of Three-Dimensional Cellular Materials.* Proc. R. Soc. Lond, 1982. **382**: p. 43-59.

60.   Kadashevich, I. and D. Stoyan, *A beam-network model for autoclaved aerated concrete and its use for the investigation of relationships between Young's modulus and microstructure.* Computational Materials Science, 2008. **43**(2): p. 293-300.

61.   Roberts, A.P. and E.J. Garboczi, *Elastic properties of model random three-dimensional open-cell solids.* Journal of the Mechanics and Physics of Solids, 2002. **50**(1): p. 33-55.

62.   Roberts, A.P. and E.J. Garboczi, *Elastic moduli of model random three-dimensional closed-cell cellular solids.* Acta Materialia, 2001. **49**(2): p. 189-197.

63.   Carson, J.K., et al., *Thermal conductivity bounds for isotropic, porous materials.* International Journal of Heat and Mass Transfer, 2005. **48**(11): p. 2150-2158.

64.   Holman, J.P., *Heat transfer.* 1989: McGraw-Hill.

65.   Wang, J., et al., *A new structural model of effective thermal conductivity for heterogeneous materials with co-continuous phases.* International Journal of Heat and Mass Transfer, 2008. **51**(9-10): p. 2389-2397.

66.   Qiang Li , H.W., Zuhua Zhang and Andrew Reid, *Numerical simulation of porosity on thermal properties and fire resistance of foamed concrete.* Journal of Sustainable Cement-Based Materials, 2013. **2**(1): p. 1-7.

67.   Maxwell, J.C., *A treatise on electricity and magnetism*, ed. t. ed. 1954, New York Dover Publications Inc.

68.   Kim, H.K., J.H. Jeon, and H.K. Lee, *Workability, and mechanical, acoustic and thermal properties of lightweight aggregate concrete with a high volume of entrained air.* Construction and Building Materials, 2012. **29**(0): p. 193-200.

69.   Bentz, D.P., et al., *Thermal properties of high-volume fly ash mortars and concretes.* Journal of Building Physics, 2011. **34**(3): p. 263-275.

70.   Zhou, Z., S.W. Rees, and H.R. Thomas, *A numerical and experimental investigation of ground heat transfer including edge insulation effects.* Building and Environment, 2002. **37**(1): p. 67-78.

71.   Ke, Y., et al., *Identification of microstructural characteristics in lightweight aggregate concretes by micromechanical modelling including the interfacial transition zone (ITZ).* Cement and Concrete Research, 2010. **40**(11): p. 1590-1600.

72.   Nguyen, V.P., M. Stroeven, and L.J. Sluys, *Multiscale failure modeling of concrete: Micromechanical modeling, discontinuous homogenization and parallel computations.* Computer Methods in Applied Mechanics and Engineering, 2012. **201-204**: p. 139-156.

73.   Chindaprasirt, P., C. Jaturapitakkul, and T. Sinsiri, *Effect of fly ash fineness on compressive strength and pore size of blended cement paste.* Cement and Concrete Composites, 2005. **27**(4): p. 425-428.

74.   Zhang, Z., et al., *Geopolymer foam concrete: An emerging material for sustainable construction.* Construction and Building Materials, 2014. **56**: p. 113-127.

75.   Babu, D.S., K. Ganesh Babu, and W. Tiong-Huan, *Effect of polystyrene aggregate size on strength and moisture migration characteristics of lightweight concrete.* Cement and Concrete Composites, 2006. **28**(6): p. 520-527.

76.   Babu, K.G. and D.S. Babu, *Behaviour of lightweight expanded polystyrene concrete containing silica fume.* Cement and Concrete Research, 2003. **33**(5): p. 755-762.

77.   Duškov, M. and A. Scarpas, *Three-dimensional finite element analysis of flexible pavements with an (open joint in the) EPS sub-base.* Geotextiles and Geomembranes, 1997. **15**(1–3): p. 29-38.

78.   Miled, K., et al., *Compressive behavior of an idealized EPS lightweight concrete: size effects and failure mode.* Mechanics of Materials, 2004. **36**(11): p. 1031-1046.

79.   Miled, K., K. Sab, and R. Le Roy, *Particle size effect on EPS lightweight concrete compressive strength: Experimental investigation and modelling.* Mechanics of Materials, 2007. **39**(3): p. 222-240.

80.   Liu, N. and B. Chen, *Experimental study of the influence of EPS particle size on the mechanical properties of EPS lightweight concrete.* Construction and Building Materials, 2014. **68**: p. 227-232.

81.   Chen, B. and N. Liu, *A novel lightweight concrete-fabrication and its thermal and mechanical properties.* Construction and Building Materials, 2013. **44**: p. 691-698.

82.   Ling, I.H. and D.C.L. Teo, *Properties of EPS RHA lightweight concrete bricks under different curing conditions.* Construction and Building Materials, 2011. **25**(8): p. 3648-3655.

83.   Bouvard, D., et al., *Characterization and simulation of microstructure and properties of EPS lightweight concrete.* Cement and Concrete Research, 2007. **37**(12): p. 1666-1673.

84.   Laukaitis, A., R. Žurauskas, and J. Kerien≐, *The effect of foam polystyrene granules on cement composite properties.* Cement and Concrete Composites, 2005. **27**(1): p. 41-47.

85.   Fu, G. and W. Dekelbab, *3-D random packing of polydisperse particles and concrete aggregate grading.* Powder Technology, 2003. **133**(1–3): p. 147-155.

86.   Liu, Y., Z. You, and Y. Zhao, *Three-dimensional discrete element modeling of asphalt concrete: Size effects of elements.* Construction and Building Materials, 2012. **37**(0): p. 775-782.

87.   Farghal Maree, A. and K. Hilal Riad, *Analytical and experimental investigation for bond behaviour of newly developed polystyrene foam particles' lightweight concrete.* Engineering Structures, 2014. **58**(0): p. 1-11.

88.   Wang, Y., J.Y.R. Liew, and S.C. Lee, *Theoretical models for axially restrained steel-concrete-steel sandwich panels under blast loading.* International Journal of Impact Engineering, 2015. **76**(0): p. 221-231.

89.   Bardella, L., et al., *A micromechanical model for quasi-brittle compressive failure of glass-microballoons/thermoset-matrix syntactic foams.* Journal of the European Ceramic Society, 2014. **34**(11): p. 2605-2616.

90.   Scerrato, D., et al., *A simple non-linear model for internal friction in modified concrete.* International Journal of Engineering Science, 2014. **80**(0): p. 136-152.

91.   Shigang, A., et al., *Effect of aggregate distribution and shape on failure behavior of polyurethane polymer concrete under tension.* Computational Materials Science, 2013. **67**(0): p. 133-139.

92.   She, W., Y. Zhang, and M.R. Jones, *Three-dimensional numerical modeling and simulation of the thermal properties of foamed concrete.* Construction and Building Materials, 2014. **50**(0): p. 421-431.

93.   Bardella, L., et al., *A critical evaluation of micromechanical models for syntactic foams.* Mechanics of Materials, 2012. **50**: p. 53-69.

94.   Yeh, I.C., *Computer-aided design for optimum concrete mixtures.* Cement and Concrete Composites, 2007. **29**(3): p. 193-202.

95.   Sobhani, J. and M. Najimi, *Numerical study on the feasibility of dynamic evolving neural-fuzzy inference system for approximation of compressive strength of dry-cast concrete.* Applied Soft Computing, 2014. **24**(0): p. 572-584.

96.   Alshihri, M.M., A.M. Azmy, and M.S. El-Bisy, *Neural networks for predicting compressive strength of structural light weight concrete.* Construction and Building Materials, 2009. **23**(6): p. 2214-2219.

97.   Bal, L. and F. Buyle-Bodin, *Artificial neural network for predicting drying shrinkage of concrete.* Construction and Building Materials, 2013. **38**(0): p. 248-254.

98.   Chandwani, V., V. Agrawal, and R. Nagar, *Modeling slump of ready mix concrete using genetic algorithms assisted training of Artificial Neural Networks.* Expert Systems with Applications, 2015. **42**(2): p. 885-893.

99.   Ghafoori, N., et al., *Predicting rapid chloride permeability of self-consolidating concrete: A comparative study on statistical and neural network models.* Construction and Building Materials, 2013. **44**(0): p. 381-390.

100. Cihan, M.T., A. Güner, and N. Yüzer, *Response surfaces for compressive strength of concrete.* Construction and Building Materials, 2013. **40**(0): p. 763-774.

101. del Coz Díaz, J.J., et al., *Hygrothermal properties of lightweight concrete: Experiments and numerical fitting study.* Construction and Building Materials, 2013. **40**(0): p. 543-555.

102. Chaoming Song, P.W.H.A.M., *A phase diagram for jammed matter.* Nature, 2008. **453**: p. 629-632.

103. Miyauchi, S.Y.J.K.M., *Multi-Sized Sphere Packing.* 2009: p. 1-45.

104. Huang, Q., et al., *Numerical analysis of the effect of coarse aggregate distribution on concrete carbonation.* Construction and Building Materials, 2012. **37**(0): p. 27-35.

105. Ozen, M. and M. Guler, *Assessment of optimum threshold and particle shape parameter for the image analysis of aggregate size distribution of concrete sections.* Optics and Lasers in Engineering, 2014. **53**(0): p. 122-132.

106. Xu, W.X., Z. Lv, and H.S. Chen, *Effects of particle size distribution, shape and volume fraction of aggregates on the wall effect of concrete via random sequential packing of polydispersed ellipsoidal particles.* Physica A: Statistical Mechanics and its Applications, 2013. **392**(3): p. 416-426.

107. Shuguang, L. and L. Qingbin, *Method of meshing ITZ structure in 3D meso-level finite element analysis for concrete.* Finite Elements in Analysis and Design, 2015. **93**(0): p. 96-106.

108. Ganesh Babu, K. and D. Saradhi Babu, *Performance of fly ash concretes containing lightweight EPS aggregates.* Cement and Concrete Composites, 2004. **26**(6): p. 605-611.

109. Anastaselos, D., S. Oxizidis, and A.M. Papadopoulos, *Energy, environmental and economic optimization of thermal insulation solutions by means of an integrated decision support system.* Energy and Buildings, 2011. **43**(2–3): p. 686-694.

110. Kolaitis, D.I., et al., *Comparative assessment of internal and external thermal insulation systems for energy efficient retrofitting of residential buildings.* Energy and Buildings, 2013. **64**(0): p. 123-131.

111.   Yew, M.C., et al., *Integration of thermal insulation coating and moving-air-cavity in a cool roof system for attic temperature reduction.* Energy Conversion and Management, 2013. **75**(0): p. 241-248.

112.   Yu, M., et al., *A unified method for calculating fire resistance of solid and hollow concrete-filled steel tube columns based on average temperature.* Engineering Structures, 2014. **71**(0): p. 12-22.

113.   Marquis, D.M., G. Auguin, and P. Barabinot, *Poster abstracts-Fire Resistance of Sandwich Composite Materials.* Procedia Engineering, 2013. **62**(0): p. 1121-1127.

114.   Porcari, G.-L.F., E. Zalok, and W. Mekky, *Fire induced progressive collapse of steel building structures: A review of the mechanisms.* Engineering Structures, 2015. **82**(0): p. 261-267.

115.   Chow, W.K. and Y.Y. Chan, *Computer simulation of the thermal fire resistance of building materials and structural elements.* Construction and Building Materials, 1996. **10**(2): p. 131-140.

116.   DP Bentz, M.P., A Dura´n-Herrera, P Valdez and CA Jua´rez, *Thermal properties of high-volume fly ash mortars and concretes.* Journal of Building Physics, 2011. **34**: p. 263-275.

117.   J.P.Holman, *Heat Transfer*. the 9th Edition ed. 2005, Beijing: China Machine Press.

118.   Wang Yushu, F.C., *Abaqus structural engineering analysis and examples to explain*. 2011, Beijing: Chinese constructional industrial Press.

Appendix

Appendix 1 Program for 2D pore structure model

```
1.  clear all
2.  depth=100;
3.
4.  n=0;
5.  N=0;
6.  V=0;
7.  V1=0.5; % V1?????V??????????
8.
9.  while V<=V1
10. n=n+1
11. r(n)=rand*20+5;
12. xc(n)=rand*(depth-2*r(n))+r(n);yc(n)=rand*(depth-2*r(n))+r(n);
13.
14. if n==1 % First circle center
15. N=N+1;
16. r(N)=r(n);
17. xc(N)=xc(n);yc(N)=yc(n);
18. V=V+pi*r(N)^2/depth^2;
19. end
20.
21. if n>=2
22. for i=1:N
23. d(i)=sqrt((xc(n)-xc(i))^2+(yc(n)-yc(i))^2);
24. rr(i)=r(i)+r(n);
25. d_rr(i)=d(i)-rr(i);
26. end
27. if min(d_rr)>0
28. N=N+1;
29. r(N)=r(n);
30. xc(N)=xc(n);
31. yc(N)=yc(n);
32. V=V+pi*r(N)^2/depth^2;
33. end
34. clear d rr d_rr
35. end
36.
37. end
38.
39. % Plot
40.
41. d=pi/20;
42. t=0:d:2*pi;
43. xx=cos(t);yy=sin(t);
44.
```

```
45. for i =1 : N
46. x=xx*r(i)+xc(i);
47. y=yy*r(i)+yc(i);
48. plot(x,y)
49. axis([0 100 0 100]);
50. hold on
51. end
52. hold off
```

Appendix 2 python program for generating 3D pore structure

```python
from part import *
from material import *
from section import *
from assembly import *
from step import *
from interaction import *
from load import *
from mesh import *
from job import *
from sketch import *
from visualization import *
from connectorBehavior import *
import random
import math

#Euclidean Distance Measure
def euclidean_py(x, y):
    # lightly modified from implementation by Thomas Sicheritz-Ponten.
    # This works faster than the Numeric implementation on shorter
    # vectors.
    if len(x) != len(y):
        raise ValueError, "vectors must be same length"
    sum = 0
    for i in range(len(x)):
        sum += (x[i]-y[i])**2
    return math.sqrt(sum)

#Create Cube
mdb.models['Model-1'].ConstrainedSketch(name='__profile__', sheetSize=200.0)
mdb.models['Model-1'].sketches['__profile__'].rectangle(point1=(0.0,        0.0),
point2=(1.0, 1.0))
mdb.models['Model-1'].Part(dimensionality=THREE_D,             name='Part-1',
type=DEFORMABLE_BODY)
mdb.models['Model-1'].parts['Part-1'].BaseSolidExtrude(depth=1.0,
sketch=mdb.models['Model-1'].sketches['__profile__'])
del mdb.models['Model-1'].sketches['__profile__']
```

```
#Instantiate cube
mdb.models['Model-1'].rootAssembly.Instance(dependent=ON,    name='tmpCube',
part=mdb.models['Model-1'].parts['Part-1'])

#File Output
text_file = open("c:\Sphere_Positions.txt", "w")

#Radius of one sphere
#r = (3*0.30)/(4*math.pi*n)
#r = r**(1.0/3.0)
#print "Sphere Radius is " + str(r)
#text_file.write("Sphere Radius is " + str(r) + "\n")
#Number of Spheres
#define the radius of EPS beads
r=3.5
print "Sphere Radius is " + str(r)
text_file.write("Sphere Radius is " + str(r) + "\n")

#define the total number of EPS beads
n=round(3*40*40*40*0.2/(4*math.pi*r*r*r))
print "Total sphere number is " + str(n)
#n=108
text_file.write("Number of Spheres: " + str(n) + "\n")


#Create Sphere
mdb.models['Model-1'].ConstrainedSketch(name='__profile__', sheetSize=200.0)
mdb.models['Model-1'].sketches['__profile__'].ConstructionLine(point1=(0.0,
-100.0), point2=(0.0, 100.0))
mdb.models['Model-1'].sketches['__profile__'].FixedConstraint(entity=mdb.models[
'Model-1'].sketches['__profile__'].geometry[2])
mdb.models['Model-1'].sketches['__profile__'].ArcByCenterEnds(center=(0.0,  0.0),
direction=CLOCKWISE, point1=(0.0, -r), point2=(0.0, r))
mdb.models['Model-1'].sketches['__profile__'].Line(point1=(0.0,   -r),   point2=(0.0,
r))
mdb.models['Model-1'].sketches['__profile__'].VerticalConstraint(entity=mdb.mode
ls['Model-1'].sketches['__profile__'].geometry[4])
mdb.models['Model-1'].Part(dimensionality=THREE_D,            name='Part-2',
type=DEFORMABLE_BODY)
mdb.models['Model-1'].parts['Part-2'].BaseSolidRevolve(angle=360.0,
flipRevolveDirection=OFF, sketch=mdb.models['Model-1'].sketches['__profile__'])
del mdb.models['Model-1'].sketches['__profile__']

#List of Spheres
sphereList = []
sphereInstancesList = []

#Create n instances of the sphere
```

```
for i in range(1, n+1):
    InstanceName = 'Sphere_' + str(i)
    print InstanceName
    text_file.write(InstanceName)

    #Maximum tries to distribute sphere
    maxTries = 1000

    while len(sphereList) < i:
        maxTries -= 1
        if maxTries < 1:
            print "Maximum Distribution tries exceeded. Error! Restart the
Script!"
            break;

        #Make sure Spheres dont cut cube sides
        vecPosition                                                     =
[r+(random.random()*(1.0-r-r)),r+(random.random()*(1.0-r-r)),r+(random.random()
*(1.0-r-r))]
        for pos in sphereList:
            if euclidean_py(pos, vecPosition) < 2*r:
                break
        else:
            sphereList.append(vecPosition)
            print vecPosition
            text_file.write("\t" + str(vecPosition) + "\n")
            #Instantiate Sphere
            mdb.models['Model-1'].rootAssembly.Instance(dependent=ON,
name=InstanceName, part=mdb.models['Model-1'].parts['Part-2'])
            #Translate Instance of Sphere

mdb.models['Model-1'].rootAssembly.translate(instanceList=(InstanceName,        ),
vector=vecPosition)

sphereInstancesList.append(mdb.models['Model-1'].rootAssembly.instances[Instanc
eName])

print "Sphere Radius is " + str(r)

#Cut all spheres with cube
mdb.models['Model-1'].rootAssembly.PartFromBooleanCut(cuttingInstances=(
sphereInstancesList ),
instanceToBeCut=mdb.models['Model-1'].rootAssembly.instances['tmpCube'],
name='Part-3')

#Intantiate Cut Object
mdb.models['Model-1'].rootAssembly.Instance(dependent=ON, name='Cube',
part=mdb.models['Model-1'].parts['Part-3'])
```

```
#Delete temporary cube
del mdb.models['Model-1'].rootAssembly.instances['tmpCube']

text_file.close()
```